MASTERARBEIT

Titel der Masterarbeit

„Photogrammetry in a quarry

-

3D modeling and joint evaluation“

verfasst von

David Grebenstein B.Sc.

angestrebter akademischer Grad

Master of Science (M.Sc.)

Wien, 2014

Studienkennzahl lt. Studienblatt:	A 066 815
Studienrichtung lt. Studienblatt:	Erdwissenschaften UG 2002
Betreuer:	PD Mag. Dr. Erich Draganits

Erklärung zum eigenständigen Verfassen der Arbeit

Ich versichere, dass ich die vorliegende Arbeit selbständig verfasst und keine anderen als die angegebenen Quellen und Hilfsmittel verwendet habe. Die Arbeit wurde in gleicher oder ähnlicher Form noch nicht in einem anderen Studiengang als Prüfungsleistung verwendet.

Wien, am

Unterschrift

(David Grebenstein)

1 Outline

Table of content

1 Introduction

Up-to-date aerial photos and their derivatives represent important remote sensing data with abundant applications. Their applications stretch from land surveying, vegetation evaluation and real estate photography, to base maps for emergency planning. Recently, technological advances have increased the possibility to produce high-quality aerial photos with minimal investment by the use of civil drones, called unmanned aerial vehicles (UAVs). First experiments were conducted by Rzybilla and Wester-Ebbinghaus (1979) with a model airplane. Later Wester-Ebbinghaus (1980) used a model helicopter as transport vessel. For the first time this approach was scientifically successfully used in 2006 by a research group from the ETH Zürich for an archeology project (Eisenbeiss and Zhang, 2006). In the following, more projects and further development can be found in Eisenbeiss and Zhang (2006), (Eisenbeiß, 2009a), Gruen et al. (2009), Zhou (2009), Sauerbier and Eisenbeiss (2010), Barazzetti et al. (2010). Further reading and inspiration is found in, Remondino et al. (2011), Nex and Remondino (2014), and especially in the internet forums of the webpages DIY drones (2014), rcgroups.com (2014) and a distinguished source is Duffy (2014).

Recently, many of the applications are based on the new multicopter models but less on the classical fixed-wing type. Nevertheless, a group of motivated individuals have created a project for low-cost land survey (Wich et al., 2014). There are several geological applications of UAV photography.

1.1 Geological hazards

The hazard of rock fall or other mass movements is omnipresent in alpine environments. In addition to the danger posed by the usual triggering mechanisms like rain, snow, changing groundwater-table, and pore water pressure, recently also the challenge of changing permafrost levels has been recognized as an important aspect (Arenson, 2002). Here the melting conditions can lead to instabilities in very short time intervals, necessitating careful research. This research requires the utmost care as the unstable environment is hard to assess for a geologist (Phillips et al., 2003-2004). In such a situation the use of UAVs is a very valuable asset, providing an alternative to risking the researchers' life. While of course direct observation by an experienced geologist is invaluable, the value of the geologist's lives is infinitely higher. Also, even inaccessible rock formations can be monitored (Kääb et al., 1997). The change of bonding between rocks by melting of ice can be documented as well as the crack-widening process caused by the periodic freezing and melting of the interstice water.

This becomes increasingly necessary because retreat of the permafrost continuously results in threatening instability in new locations (Phillips et al., 2003-2004).

As these mechanisms pose a permanent danger to the general public, they have to be monitored regularly. For this, UAV based monitoring has to be considered, as it is an effective, low-cost approach. Time dissolved DSMs have already been proven to be a good tool to monitor mass movements (Mikoś and Hübel, 2008). Now, with the enhanced capabilities of the UAVs, small areas can be scanned several times a week, comparable to terrestrial laserscanning (TLS) for avalanche monitoring during winter season (Prokop, 2008). This enables scientists and engineers to take responsive actions as needed, based on up-to-date data. Because of the low cost of an UAV their use could be considered even in emerging countries, often probably constituting the only means to observe hazardous areas that would otherwise go unmonitored due to insufficient funds (Wich et al., 2014). The operators not only gain a new monitoring tool but also the option to only have rather short intervals between flights, the higher resolution in terms of time being the key advantage.

All in all this shows that time dissolved monitoring for potential mountain hazards is one of the most important capabilities of UAVs.

Many other applications are feasible, like monitoring volcanos (Pyle et al., 2013), e.g. photogrammetric evaluation and documentation of progressing lava flows (O'Callaghan, 2014). The photo camera could be exchanged for a thermal camera, visualizing the temperatures of such an environment. Observing gas vents with changing locations and size, or small erupting craters is also important, as they show fluctuations before, while and after heavy eruptions. Additionally, gas monitoring is possible (McGonigle, et al., 2008) and together with a ash concentration assessment by small handheld spectrometers would complete the remote-sensed picture of a volcano, enabling the authorities and scientist to base their decisions on facts and, if necessary, to warn the public and to evacuate high-risk areas.

1.2 Fast and low-cost documentation of geological events

Another possible application would be the response in case of catastrophic events. In such cases a quick assessment of the damage, an assessment of the remaining danger, and prevention of potential further loss is of high importance. Such events, in the media mostly dubbed ‘natural catastrophes’ (Lenzer, 2013) include fresh rock fall, landslides, earthquakes or volcanic eruptions, which have a high impact on the human population in the vicinity. The creation of base-maps assessing zones of different risk levels is vital in such a situation in order to coordinate rescue missions without endangering more lives.. In such a situation full-size helicopters will be needed for transport of resources, equipment and the wounded. Gaining an aerial overview can very well be taken over by an UAV, freeing resources for further rescue efforts. Additionally, if further life-threatening situations, like an aftershock are to be expected, the potential loss of an UAV is a low price to pay for the safety of rescuers and geologists.

Furthermore, anthropogenic damages can be dealt with, e.g. cave-ins or collapses in old mining regions (SpiegelOnline, 2009). There, photo-documentation, photogrammetry based-basemaps, and surface models or videos can play an important part in handling collapsing surfaces. Cave-ins are not only the result of collapsing old and abandoned (especially artisanal) mines but can also occur naturally due to calcite dissolving processes (karst). These structures (dolina) can vary in scale between small (sub-meter) to very large (20 m and bigger) (theguardian, 2013). If such structures develop, immediate action is required to assess the potential risk (Robertson and Orndorff, 2013). Roping down a geologist is not always possible without risk for the same reasons as stated above. Again small multicopters and a workflow for photogrammetric surface-modeling can help to understand the trigger and mechanism. The necessary calculation of the required minimum amount of concrete for filling the holes can be calculated with this data, too, mitigating any potential hazard for the community. The same workflow for documentation can be applied if infrastructure and lives are endangered by the collapse of escarpments of old open pit mining or high cliffs in touristic recreation areas (Pachmann, 2012).

1.3 Exploration

For exploration of hydrocarbons, the photogrammetric UAV approach can enable scientists to model potential reservoirs. Outcropping members of potential source and/or reservoir rocks can be mapped in 3D, allowing the geologist to build a 3D model of the reservoir and estimate potential yield of the oil or gas field. The cubatures can be gauged in higher detail, as changes in height as well as other heterogeneities of the reservoir rocks can be documented fairly easily (S. J. Buckley et al., 2008, CIPR Virtual Outcrop Geology Group, 2014a, 2014c).

In the mining industry, potential environmental polluters could be detected with the help of UAVs, e.g. tracing illegal dumping of waste water. But not only intended but also accidental spillage can be documented for example by insurances. Tailings and treatment plants for acid mine drainage could be monitored more easily and optimized for maximum efficiency. Here again exchanging the normal camera with a thermal camera would be suggested. The chemical reaction of the acidic water should give a thermal signature; the same applies for the breakdown of acids or other potential noxious agents by biota in the waste water of a mine. An optimized workflow would have to be developed in regards to these special tasks.

Another application would be the monitoring of heap bioleaching (Riekkola-Vanhanen, 2010), i.e. spraying acidic solutions and special bacteria on deposited excavation material (heap). The bacteria are chosen for their selective degradation ability, resulting in leaching of the metal ores without dissolving the sulfides. This is a strong exothermal process, again potentially resulting in a thermal signature. As heap bioleaching is a coarse method close monitoring is necessary, especially to avoid environmental damage. The process can subsequently be monitored for breakdown of the heaps (photogrammetric modeling), thermal signature (thermal camera) and potential leakage (oblique or nadir facing images) of the acidic waters.

1.4 Documentation of sedimentary and erosive processes

Evaluation of recent developments of clastic embankments is possible. Again, a time dissolved approach would help to document the cubatures deposited and eroded on the sides of a river bank (e.g. braided river system) (Abel et al., 2014) (CIPR Virtual Outcrop Geology Group, 2014b). This would help with assessing the lifetime and planning the maintenance of retardation buildings or hydro-electrical plants. At the same time the catchment-area can be surveyed, processed and modeled for potential discharge during a flooding event. The area surrounding a dam can be modeled for catastrophic events e.g. collapse of a dam or overflow of flood control basin. A 3D model would help to develop emergency plans for such situations and allow modelling of soil erosion, destabilization of rocks as well as the behavior of potential debris flows in a valley (in-Terra, 2011).

In more arid areas the movement of dunes can be monitored and their size can be easily calculated. Similarly deposits of sandstorms and other possible features of desertification can be observed. Further, in arid regions precipitation can cause massive erosion gullies (Christian, 2014) that pose a thread for the safety of streets or paths and potentially also remove the soil in agricultural areas resulting is poor yield of the fields.

For a geologist working in civil engineering, UAV based photogrammetry can help calculating the necessary amount of explosives for blasting huge road cuts and controlling the blasting success.

The retreat of glaciers is an important subject of current research (Paul et al., 2007). One of the aspects, the lateral retreat, is measurable quite easily by just subtracting the extent of one stage from the next with the use of satellite imagery. Volumina, however, require 3D measurements. Again TLS could be employed, but full coverage, including the crevasses and other shadowing elements can only be detected with expensive airborne laserscanning or via UAV (Vieira, 2014).

Besides the already stated advantages of the UAV approach, another equally important aspect has to be taken into account: the education of an larger audience and heightening awareness for climate change and possible threats posed to human life (see below for details on teaching).

1.5 Advantages compared to laserscanning

The most obvious and important advantage of UAV photogrammetry is the 3D coverage of objects, thus reducing the amount of shadowing compared to laserscanning. The handling of this problem with means of terrestrial laserscanning is very tendious as it is hindered by the weight of the heavy machinery to be transported. This is especially true if the study area is in an alpine environment (personal communication with G. Hatzenbichler). The advantage over airborne laserscanning is the achievable resolution and the already stated more complete coverage of e.g. overhanging rocks.

This is a critical factor, as on-demand airborne laserscanning is very expensive and not always available in remote areas or due to schedule conflicts. Also, airborne laserscanning is not comparable in terms of resolution, especially in the case of overhanging rock or small outcrops. The investment that has to be made for a single terrestrial laserscanner equals up the cost of several UAVs.

Another advantage is the resulting texture of the model, as it is photorealistic in terms of resolution. This allows revisiting outcrops for further reference. Teaching can be improved here as well, as human perception is based on three-dimensional impressions; this enables the lecturer to show outcrops or and give real-life examples in the lecture hall that could otherwise only be demonstrated in the field (cf. Kikinis et al., 1996). This not only results in eye-opening moments but enhances the perception by magnitudes, resulting in better understanding of described topic.

1.6 Mapping

Geological surveys are often based on orthophotos enabling the geologist not only to navigate in unknown terrain but also to have a second perspective from above. Some structures only reveal their characteristics by having an overview from above. Some areas are not accessible on foot for various reasons, e.g. great danger for life and material or unreachable because of exposition, *et cetera*. In these cases, both orthophotos as well as oblique aerial shots are useful, if they do not even make the important difference. Here the UAV based approach helps as it allows the production of literally up-to-date aerial orthophotos on demand. These enable the geologist to create a map based on the most recent available data of the area worked on. The use of a GNSS- System, capable of handling and showing this data, allows a more accurate placement of observed features because of the correctness and currentness of the mapping base that matches the field perception.

The best possible scenario for inaccessible outcrops would be complete 3D coverage with decent resolution and the ability to evaluate it from a safe workstation.

All abbreviations are listed in the appendix (12- Abbreviations).

1.7 Aim of work

The aim of this work is a proof of concept towards a geological use and handling of an UAV while keeping the costs to a minimum. Primarily, the achievable and the effective usable resolution and, in the following, possible applications are evaluated. As for applications, a mappable orthophoto and digital surface model (DSM) are aimed for. Additionally, an assessment of the possible remote sensing of faults and joints is interesting. Having an overview over the faults and joints can help with the interpretation of structure geological features and e.g. quarry design. The used software will be evaluated as well.

As this work is a methodical approach, the description of the geological stetting and the distinct features within the quarry have not been considered in detail.

After testing a hobby-level fixed-wing plane for aerial photography, the evaluation of a 3D ground survey was conducted. The tested area in this work is a quarry which qualifies by having a considerable relief to test the 3D capabilities, small-scale structures at the quarry benches for resolution assessment, and low / no-vulnerability in case of UAV crashes.

The project is the first study of this kind in the institute with these spatial dimensions thus representing an evaluation of the workflow for future applications in areas were high-resolution remote sensing data is not available.

2 Background

2.1 Choice of UAV

All UAVs in this work can be classified according to the different classes described by (Eisenbeiß, 2009b). The limit for this group is a maximum flight time of one hour, a maximum flight altitude of 250 m, a horizontal range lower than 10 km, and a weight lower than 5 kg. Specific values may differ, especially regarding the flight time, as this is the most critical one. Some data of the UAV used in this study can be found below.

Many surveys use data gathered with relatively newly developed multicopters rather than the classical fixed-wing type. This seems to be based in the easy vertical take-off and landing (VTOL) capabilities of multicopters and the beginner-friendly shallow learning curve, if used with altitude hold (ALThold) possibility and loiter function – global navigation satellite system (GNSS)-fix. The fixed-wing UAV has advantages over multicopters by having a much bigger aerial coverage. Most geological problems can only be solved by looking at larger scales, thus greater coverage is most useful. The achieved resolution should not suffer though. In case of a required small-scale operation or refining of a model, a small multicopter can always be employed.

2.2 Return on invest

After establishing the workflow, the user profits for various reasons, especially if the desired resolution has to be equal or better than commercially available survey data. These advantages include:

- higher availability through low cost options and easy transport of equipment
- due to being a low-cost approach, easier and more frequent repetitions of the surveys are possible
- reduced risk for employees in hazardous environments e.g. rock fall (see Figure 1)

And finally, a reason never to be underestimated:

- in-house production

Figure 1: Working safety; potential rock fall (black), operator (red), car (orange), safe distance (green); note: picture taken from UAV

Producing data without having data handed out to subcontractors, thus reducing the risk of accidental data loss or undocumented data copying, can be crucial for an operation, both business or research. This enables the user to handle confidential data with ease.

3 Methods and setup

3.1 Setup (technical)

For the UAV flights the following setups were used. A list of abbreviations is found in the appendix (see chapter 12 Abbreviations).

1. Bixler 2; flight time 15 minutes (see Figure 2)
    a. 2200 kv (revolutions per apl. Volt) brushless motor
    b. 30 A electronic speed controller (ESC)
    c. 11 g metal gear (MG) servos (HK MG90s)
    d. 4 Ah 3s lithium polymer (LiPo) battery (Turnigy)
    e. 600 TV lines (TVL) Super HAD security camera
    f. Video transmitter (VTx) (5.8 GHz)
    g. G-OSD (on-screen-display)
    h. Canon Ixus 75 w/ Canon hack development kit (CHDK)
2. Finwing Penguin; flight time 20 minutes (see Figure 2)
    a. 1200 kv brushless motor
    b. 70 A ESC
    c. 17 g servos (Hitec 82MG and HK 939)
    d. 4 Ah / 5 Ah / 2x4 Ah 3s LiPo
    e. 600 TVL Super HAD security camera
    f. VTx (5.8 GHz)
    g. ArduPilotMega 2.5 w/ minimOSD, serial telemetry
    h. Canon Powershot s110 w/ CHDK
    i. shuttercontrol (arduino nano w/ firmware: theotherhand.com)
3. Tricopter 2.5; flight time 7 minutes (see Figure 2)
    a. 900 kv brushless motor (NTM 28-30s 900kv)
    b. 20 A ESC (HK F-20A)
    c. 11 g servo (Hitec 82MG)
    d. 3.3 Ah 3s LiPo (Turnigy nano-tech)
    e. 600 TVL Super HAD security camera
    f. E-OSD w / CL-OSD
    g. VTx (5.8 GHz)
    h. Canon Ixus 75 w/ CHDK

4. Hexacopter (Gaui 540H frame); flight time 10 minutes (see Figure 2)
    a. 6x 780 kv (Robbe roxxy 2827-34 760 kv)
    b. 20 A ESC (HK F-20A)
    c. 4.8 Ah 4s LiPo (zippy Compact / Turnigy nano-tech)
    d. Sony EffioE security camera
    e. VTx (5.8 GHz)
    f. APM w/ minimOSD, serial telemetry
    g. Canon Ixus 75 w/ CHDK
    h. Simple DIY wooden gimbal

Figure 2: Finwing Penguin, ready for takeoff; Tricopter 2.5 with Ixus 75 and IR Mod; Hexacopter at maiden flight

3.2 Setup of fixed-wing UAVs / building an UAV

The Bixler 2 was the first UAV used and suffered from various high-speed landings as well as building errors. Finally, it was discarded as it was lacking the necessary space to place the flight control (FC), the battery and the camera itself in the fuselage. Nevertheless, the first orthophoto and DSM were accomplished with this UAV. The successor is a Finwing Penguin, inspiration and the overall build-ideas were taken from Duffy (2014). Having a generous opening, placing and mounting the payload as well as the equipment was easy and quick. As for interference issues, the gained room helped a lot to reduce the induced magnetic field on the magnetometer on the ArduPilotMega (APM) (DIY Drones community, 2007) as seen before on the Bixler 2. Further improvements would be possible, for example, upgrading to a 4s setup to reduce current-flow thus enhancing efficiency on the power rails. The UAV can be transported in its original packaging and can be loaded into a small car (Figure 3)

Figure 3: Finwing Penguin in transportation box (length 170 cm)

The UAV (Finwing Penguin) is modified compared to the original plans. The elevator servo is mounted in the horizontal stabilizer. The main advantage is the shorter control rod and thus less mechanical play in it. The removable rudder and horizontal stabilizer were fixed in place with hot glue; the reasons are a) the massive play even with a Velcro inlay b) fatal disintegration caused by small weeds. This is not acceptable, especially with the higher payloads used on the UAV and its critical function. The control surface in the horizontal stabilizer was exchanged to a wedge of balsa wood for more rigidity, the old one stayed warped after a small amount of use, resulting in an ineffective and unreliable control surface. The motor mount was exchanged with an aftermarket motor mount (CXN mount) resulting in a better airflow, better cooling for a now exposed electronic speed controller (ESC), and most important of all, the possibility of using a bigger 10” (25.4 cm) propeller. The hatch was used to fit the first person view (FPV) equipment and the serial modem. The FPV camera was mounted on a servo for pan enabling the pilot to have a better view and enhanced situational awareness. The acrylic dome included in the kit was discarded because it caused severe heat buildup, being aerodynamically destructive, and being very heavy. For easy and faster assembly of the wing, the screw and nut assembly at the carbon rod/aluminum tube connection was exchanged for two simple splints from remote controlled (RC)-car accessories as suggested by Duffy (2014).

3.3 Setup of multirotor UAVs

Multirotors are most sensitive to vibration induced by unbalanced propellers and motors. It is crucial to balance the blades of the propellers as well as the bells of the motors. The vibration can ‘blind’ the sensors of the FC resulting in a high-speed landing; for details see DIY Drones community, (2014b). For that reason some depending/softening foam out of latex was used, not only to protect the flight control but also the camera to preserve a crisp, sharp image. The built tricopter (Windestål, 2011) was primarily used as a learning platform but as the second build, after rebalancing all the moving parts, it turned out to be a decent lightweight support vehicle. It can be used to take useful images as well and is capable of short flights in hazardous areas for the geologist (e.g. rock fall, fresh mass movements). The hexacopter was used for test flights only. It was not used productively because the flexible frame lacked the required rigidity.

3.4 Interferences

The UAVs were built with caution in regard to interference caused by transmitter (Tx) modules on the receiver (Rx) modules, as well as high frequency noise, generated at the ESC and voltage regulators (UBECs). All important sensor cables were switched to shielded USB 2.0 grade ones. Signal and power lines to the servos and ESCs were divided into their single strands and in the following twisted with a standard cordless drill (personal communication F. Grebenstein). No twitching or other jitter-like movements were observed in the following test flights. A small keycam (#808-16 wide) was used for confirmation.

3.5 Camera setup

Best results are usually achieved with a complete manual setup of the camera. Trying to use the shutter-priority (S-mode) resulted in problems with erratic fluctuations of the aperture, in turn resulting in different sharpness in consecutive pictures. The aperture itself should be fixed as well in order to suppress that behavior. Sometimes the images were blurry although vibration had been countered. This problematic general fuzziness not caused by vibration of the pictures (like rapid movements caused by turbulent air) could be countered with closing the aperture at least two steps to overcome the lens's imperfection towards a crisp picture (see next chapter). If encountered in the following, underexposed images can be enhanced with standard software such as Irfan view (Skiljan, 2014) or similar fuzziness caused by camera movement (e.g. rolling of the plane, wind gusts, vibrations of the motor) while having the shutter open, can be compensated with shorter exposures; 1/1000 – 1/1250 seconds have proven to be very effective. High ISO must not be used to reduce and avoid color noise and washed-out gradients in the pictures. As explained above, a dark image can always be enhanced and stretched, whereas a blurred image is completely useless.

3.6 Used Cameras

In the project three (four) cameras were used (see Figure 4):

1. Ixus 75, Canon
2. Ixus 75, modified with an infrablue mod, Canon
3. Powershot SX260, Canon, discarded (see below)
4. Powershot S110, Canon

Figure 4: Used cameras Ixus 75 w/ ROSCO2007, S110 stock, Ixus 75stock

The Ixus 75 was bought on a second-hand platform. About 40 € were paid, thus a high-speed landing is not too expensive on the payload side. The camera has several advantages a) low cost b) last camera made by Canon without an image stabilization system c) compact size d) widely used e) decent image quality f) light g) easy to modify h) canon hack development kit capable (CHDK, 2006) i) robust in case of rough landings. While the camera usually is not sensitive to near-infrared (IR), the backup camera was modified by removing the IR filter. This enables the camera to also document the near-IR part of the spectra (see Verhoeven et al., 2009). Although only few experiments were done with this approach, many of them were quite promising. An infrablue system (using a ROCSO 2007 filter, see Public Lab (2013)) was employed to check on the growth of grass with the use of the normalized differenced vegetation index (NDVI). The infrablue system is an approach of removing the IR-blocking filter of a standard digital camera and subsequently putting a blue filter in front of the lens. This setup blocks out the “red” part of the visible spectra allowing the near-IR part to be sensed by the complementary metal-oxide-semiconductor (CMOS) chip on the “red”-channel. For further reading see the public lab homepage Public Lab (2014).

The second camera used in this study was a SX260 from Canon. It has several advantages compared to the Ixus75; most relevant being a higher resolution (7 Megapixel (MPx) compared to 12 MPx) and an integrated GNSS-logger. However, it was discarded because the image quality was not as good as expected (see below). Although the image quality was insufficient, the GNSS tag in the exchangeable image file format (EXIF) header of the pictures helped considerably in the process of aligning the pictures (see below).

The third camera is a Canon S110. The larger sensor promised better yield in regard to light efficiency. Also the lens was supposed to be a ”fast lens” by the manufacturer’s specifications, see Canon Inc. (2014). A disadvantage however is the lack of an integrated GNSS. The first photographs were successful, but several adjustments had to be made to the UAV. The shutter-priority had erratic fluctuation in the exposure; the integrated image stabilizer turned out to be detrimental in regard to image quality. Finally, the image quality with completely opened aperture was not good; the picture was blurry and soft. After fixing all settings manually, e.g. the shutter, the aperture, and the ISO, the pictures were better than had been expected. The movement of the image stabilizer (IS) lens thus causing blurring of the image was countered with turning up the shutter time to 1/1000 and then finally to 1/1250. The aperture was fixed three steps above the lowest possible value, resulting in a crisp image. Pinning the ISO to 100-200 gave enough exposure to acquire light and properly exposed pictures. The option to increase the ISO to 200 gives the possibility to take photos even on a cloudy day without too much compromise at the color noise level.

3.7 Camera calibration

The cameras were calibrated using a bookshelf and the software “Lens” from Agisoft (Agisoft Lens, 2011).

The bookshelf approach is a rather simple one: a photo is taken and afterwards the picture is assessed at 100 %. Any fuzziness can now be detected quite easily, as the books’ spines usually have a high amount of detail. Some prerequisites have to be kept in mind: a) the camera should be placed on a tripod b) the camera should be placed parallel to the bookshelf c) the distance should be in the infinity position of the lens d) the books should all be placed in line e) any other planar object with sufficient detail can be used as well. This fairly easy approach showed that one of the bought cameras (SX260, Canon) was insufficient in terms of picture quality. The picture was sharp in the middle but towards the corners the picture got increasingly out of focus and blurrier. That camera was then discarded.

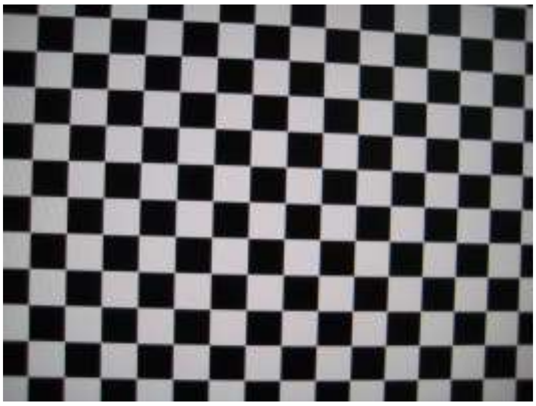

Figure 5: Chessboard-calibration-pattern, Agisoft Lens

The company Agisoft provides the software “Lens” (Agisoft Lens, 2011) free of charge. It rounds off the package required to produce decent 3D content. The software calculates the correction parameters for any kind of camera. The workflow consists of two parts; first the user takes photos of a chess pattern on the display of the workstation (Figure 5). The photos are taken with slight changes in the inclining angels. The images are processed as they are loaded into the software. Afterwards, the software computes the misfit of the lens resulting in a calibration file. This file can consecutively be used in the Photoscan software (Agisoft Photoscan, 2013).

3.8 Flight planning

As the primary goal was to evaluate the possibility of low-cost UAVs as geological tool, not too much effort was put into flight planning at the beginning. A simple look at a map and a recognizing flight for distinct landmarks was used for the first flights. Those references, as well as the low accuracy of the GNSS height, were used for the first flights, nevertheless producing acceptable results.

Figure 6: MissionPlanner software; screenshot with flight plan marked

In the following, technical enhancements were conducted at the introduction of the APM, ArduPilotMega, (DIY Drones community, 2007). Now, the need for good ground control arose. Wind directions were studied and the mission pattern was preplanned, adapted to the sensed wind direction, and uploaded via “MissionPlanner”(Michael Oborne, 2014) (Figure 6). This is important because the resulting overlap in the pictures differs due to the camera being released at a defined interval. If the wind accelerated the plane in flight direction, the resulting spacing on the ground rose dramatically. Later, the resulting line pattern was upgraded to a chessboard-like pattern to increase resolution and overlap, as well as redundancy in case of blurry images. The next step would be a chessboard-pattern at different heights. This will help to gain higher accuracy of the model.

3.9 APM

The APM, ArduPilotMega, (for details see DIY Drones community, 2007) is an open source flight control (Figure 7). It is capable of controlling a vehicle e.g. plane, copter, boat, rover and moving it fully automated over a set course. For that purpose, a set of sensors have been flowed on the circuit board (PCB): an accelerometer (ACC), a gyroscope (GYRO), a barometer (BARO), a magnetometer (MAG) and a global navigation satellite system (GNSS). These sensors provide an accurate position of the vehicle, as well as its current moving and heading in the three-dimensional space.

The used parts on the APM 2.5 are

- Honeywell digital compass HMC5883L
- Invensense 6 degree of freedom Accelerometer / GYRO combo MPU-6000
- Measurement Specialties barometric pressure sensor MS5611-01BA03
- Atmel main processor ATMEGA2560-16AU
- Atmel co-processor and USB functionality ATMEGA32U-2
- u-blox GPS Sensor NEO-6M or equivalent

For details see http://ardupilot.com/, all improtant features and data are listed thereand it was used as the main source for the information summarized in this chapter.

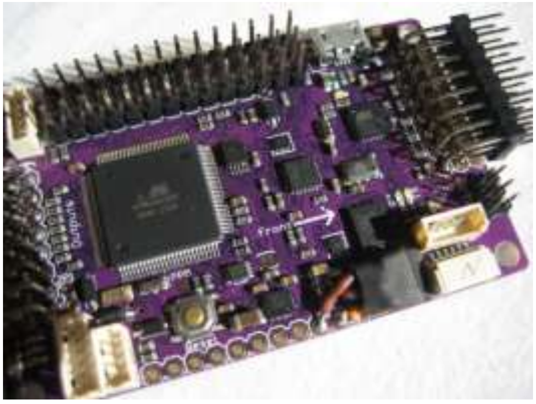

Figure 7: ArduPilotMega, with soldered 3.3V regulator in heatshrink

The sensors, especially their surface mount device (SMD)-size (small form factor chips), are a very recent development. They have risen with the rapid development of smartphones as those incorporate these sensors.

The sensors themselves have quite large errors, and especially high drift, but with the used firmware, the UAVs can hold the positions very well by compensation through combining the sensors raw data streams.

The ArduPilotMega can compensate external influences on the course such as wind and turbulences. For those routines in the code, a PID tuning dedicated to the airframe is necessary. "*P*" can be described as the amount of reaction, "*I*" as the intensity and "*D*" as the dampening of the counter force as the reaction to an applied external force (The detailed listing can be found at http://copter.ardupilot.com/wiki/arducopter-parameters/). These variables are deeply ingrained into the source code of the APM´s firmware. As the nature of this tuning is very delicate but essential to a proper flight experience, most of the build time is spend on this part of the work.

The flight course is preplanned on a computer or an android device and then uploaded via a serial connection. For this purpose a Bluetooth module, an ultra-high frequency (UHF) serial modem (433 MHz/933 MHz), or a standard serial-over-USB connection is used. The APM executes the mission at the click of a button.

For security purposes, two additional features are used. First, a "return to home function" is employed, which automatically starts if reception is lost during flight and returns the vehicle to the home position. The return to home function is useful if the RC-transmitter fails and/or interference blocks out the RC-signal. The second feature is the video transmission which gives the pilot a first-person-view (FPV), comparable to the view of an airplane pilot from the cockpit. A video overlay with important figures is projected in the video image by an external module (OSD) to help the pilot to check the status of mission, battery state, distance to home, and direction of the next rally point. A custom firmware is used, minimOSD-extra by Zoltán (2014). The displayed data is taken directly from the telemetry data stream (MAVlink protocol) sent by the APM. This enables the pilot to anticipate, and ideally avoid, high-speed landings as well as reducing the amount of "dumb-thumb"-actions (commonly known issue of misinterpreting the attitude and/or altitude of the vehicle resulting in false movement, usually resulting in a fatal high-speed landing).

3.9.1 Design flaw at the 3.3 V rail

The APM, including its clones, have a design flaw. The schematic can be found here DIY Drones community (2014a). The I^2C 3.3 V rail is dangerously underpowered and a potential loss of the UAV is possible if the 5 V input rail is exceeding 5.5 V or an additional spike is induced in the moment the USB cable is connected. If this happens the linear regulator providing the necessary 3.3 V blows, resulting in 5 V on the 3.3 V rail. The ACC and the MAG are then fed with 5 V resulting in an overload on the chip's circuit. In consequence, their outputs are no longer useful and their lifetime is relatively short at this supply. Sudden failure is possible and imminent for further details see Plischka (2014). This major problem can be fixed in a comparatively simple manner. The linear voltage regulator has to be unsoldered using a hot air flow gun, followed by the assembly of a new, bigger linear regulator. In this case a LMS117 was used. For further details please see the tutorial by Fabian Briese (2013).

3.10 Batteries

For powering the UAV, Lithium polymer batteries are used (see Figure 8). The cell voltage varies between 3.7 V and 4.2 V depending on the charging state. As ~4 V are usually not enough to power an UAV, cells are put in series to create higher voltages. This is indicated by the abbreviation Xs, X standing for the number of cells used in the pack (e.g. a pack of three cells would be marked as '3s' → ~12 V). In order to have a greater capacity, packs can also be used parallel thus gaining more mAh. The tricky part of the assembly and planning is not to overload the plane, resulting in lower flight times as the motor has to run permanently in a high, inefficient state (about 75-95 %). All information taken from Heinrich (2014).

Figure 8: Standard Lithium polymer battery; 5 Ah 3s (cell) 25 c discharge capabilities

3.11 Motors

For the UAVs brushless motors were used. They have advantages over the old brushed self-commutating motors, as they are much more efficient. The brushless motors have a 3 phase interface connected to multiple poles which are energized by the speed controller in a defined way. The resulting jumping magnetic field switches over the coiled shoes, see Vorkoetter (2014) for details. As this commutation of the phase is done at very high speeds this is synchronized by a microchip. For small multicopter UAVs the electronic speed controller (ESC) has to be flashed with a non-dampening firmware, e.g. RapidESC (SimonK), BlHeli, to keep up with the minimal throttle changes of the rotors (Snow, 2014).

3.12 GCPs and their requirements

The ground control points (GCPs) themselves were marked with standard construction-work spray-paint (see Figure 9, Figure 11, Figure 12). One can of product lasts for about 50 markings with decent covering and visibility. The markings have a radius of ~20 cm, resulting in a good visibility even with higher overview flights.

Figure 9: Used spray-paint; for best results use old discarded tiles for best reflectance and visibility

The testing of 2D-codes from Photoscan (Figure 10) was not successful as problems with the picture quality made it impossible for the Agisoft software to detect the markers. The exposure of the white paper in combination with the intense sunlight resulted in partial overexposure and blurring halos. In other pictures the resolution of the camera was insufficient, resulting in a failed detection of the markers (Figure 13). As a result, the 2D-code idea was discarded for this project. Nevertheless, the workflow can be enhanced quite significantly if the markers are detected, as the manual assignment of the markers is very time consuming.

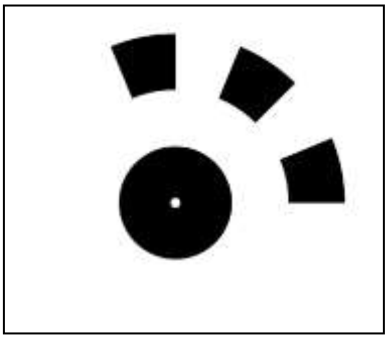

Figure 10: 2D code from Photoscan

Figure 11: Printed 2D code and spray-paint on rock

Figure 12: Spray-paint on rock, crop from aerial image as seen from 110m above ground level (AGL)

Figure 13: 2D code, crop from image as seen from ~100m AGL; note the overexposure

The positions of the ground control points were acquired with a differential GNSS (Trimble GEOHX 2008). For higher accuracy and overall better results the portable device (rover) was equipped with a carbon pole with the capability of mounting a Hurricane external antenna (Figure 14). The external antenna was mounted at 2 m height; a spirit level is attached to the pole to ensure perfectly vertical handling. At least 40 measurements (1/sec) were taken to improve accuracy. Additionally, for differential correction a secondary device was used as a base station (Figure 15). The GCPs were then corrected with the "GPS Pathfinder Office" (Trimble Navigation Ltd., 2009). Accuracy estimations can be found in the Appendix (Table 5).

Figure 14: Referencing of GCP with a Trimble DGNSS

Figure 15: Base station for differential correction; note that for increased accuracy the dome of the GNSS antenna was placed level with an additional cardboard box (not visible in photo), crate was used to increase reception

3.13 Basic introduction to photogrammetry in context of this work

The basemap for many mapping applications in the field are orthophotos. They are usually compiled from various sources but mostly lack decent quality or resolution, especially if they are free (cf. Robert, 2011). Usually, the effort of getting high quality up-to-date aerial photos is time-consuming and a significant expense factor in a project. Hence, the main goal of this work is an at least decent to even high quality orthophoto derived from the aerial shots made by a low-cost UAV. As most panoramic stitching software, like Microsoft ICE (Microsoft Corporation, 2011), produces unusable, distorted output, the way to go is clearly a more sophisticated processing. The only option to get a serviceable product is to project the pictures on a DSM, and thus calculating an undistorted mosaic of the scene.

The difference between the products is as follows (taken form Kraus (2007)): the aerial photo represents a standard photography just as produced by any consumer camera. The optical path is always inclined and connects the focal point by fanning out towards a distant representing point, a normal, human-like perspective view. Contrary, the orthophoto is a map-like image; every point is represented in a geometrically correct manner; the information is reproduced without distortion in scale and optical pathways. Figure 16 shows a 2D cut through a hypothetical hillside. The dotted line represents the orthogonal projection, the orange points being a projection of every point as seen from above. Below, the continuous line is equivalent to a photograph taken by a camera. Note the spatial difference of the orange points relative to their location on the orthophoto, shown in red.

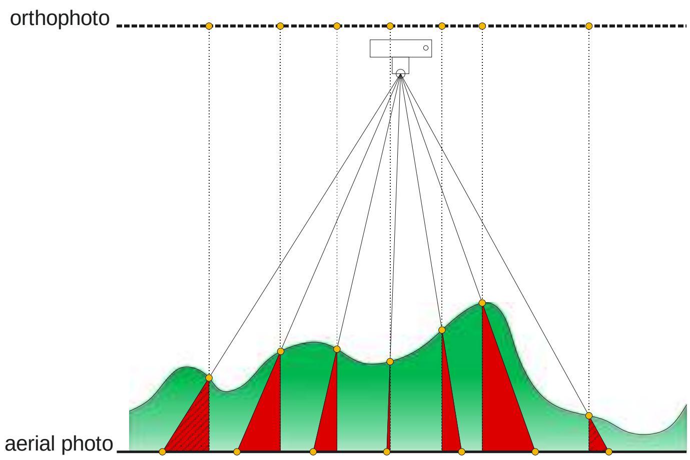

Figure 16: Schematic sketch of the difference between an aerial photo (nadir facing) and an orthophoto (modified from Kraus, 2007)

Kraus (2007) defines photogrammetry as a technique were photographic images are used to reconstruct the location and the shape of objects. The calculations and visual impressions are processed similar to how the human eye works. The eyes compare two images taken at a defined distance: the stereobase. The human brain calculates the location and the shape of the objects seen, based on the two images received from the eyes (Figure 17). The photogrammetry techniques do the same. The stereoscopic impression is created with two images, taken separately at different locations at a known distance to each other. Therefore, the images need to be shifted and rotated until they match within their overlap, thus creating the stereoscopic (3D) impression.

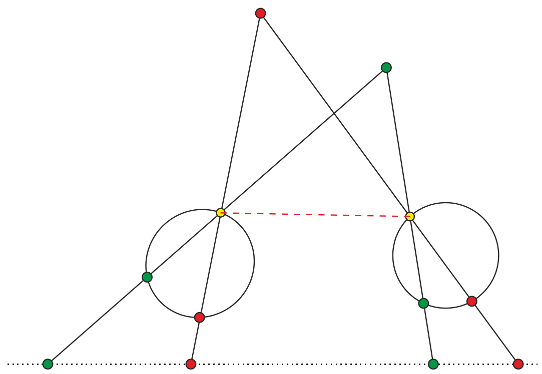

Figure 17: Model of the human eye and a projected image on a theoretical photo plane (dotted line) modified from Kraus (2007)

In the beginning, the overlay was done by massive technical-optical instruments. Some of them bigger than a fully-grown adult they were usually used for drawing plans, maps etc. The other end of the size-spectrum was small hand held devices which could even be used in the field. They all had their 3D-impression-creating capabilities in common. These workflows are called hardcopy photogrammetry.

The digital photogrammetry or softcopy photogrammetry works similar to the analogue or hardcopy photogrammetry. The main difference is the correlating power and respective accuracy. With the analogue approach, the human eye, the quality of the lens-system plus their respective arrangement, and the user's capability to arrange pictures are the limiting factors; now the ability of the computer-vision code and the available computing power define the quality of the output. For further basic reading and deeper insights it is suggested to read Drury (1998), Kasser and Egels (2002), Kraus (2007) and Linder (2009), as the information form above is extracted from these sources.

With the rise of the personal computer and the exponential growth of the respective calculation power, the possibility arose to not only use mechanical means and optics work with 3D but also the possibility to work in 3D on a digital level. With the enormous power of modern graphic cards and their parallel computation capability, the generation of 3D-content is not only limited to high-end supercomputers and/or clusters any more. Modern graphic cards have a high number of cores which allow them to process data in a parallel way, enabling them to handle quite large data quantities. The established frameworks like Compute Unified Device Architecture (CUDA) and Open Computing Language (OpenCL) enable the programmer to use these capabilities to write GPU-enabled software.

3.13.1 Theoretical background

In the following, important features and concepts of photogrammetry are described, taken from Kasser and Egels (2002), Kraus (2007), Linder (2009).

3.13.1.1 Inner orientation

The inner orientation describes the optical distortion of the camera. In a real camera the lens system is always radial displaced and decentered with respect to the sensor. Therefore, the radial lens distortion parameters (k_1, k_2, k_3, and k_4) and the decentering lens distortion parameters (p_1 and p_2) have to be considered. This correction can be described by a polynomial, the Brown's distortion model see Brown (1966):

$$x' = x(1 + K_1r^2 +K_2r^4 + K_3r^6+K_4r^8) + P_2 (r^2 + 2x^2) + 2P_{1xy}$$

$$y' = y(1 + K_1r^2 +K_2r^4 + K_3r^6+K_4r^8) + P_1 (r^2 + 2x^2) + 2P_{2xy}$$

whilst

$$r = \mathrm{sqrt}\,(x^2 + y^2)$$

x, y being the coordinates of the pixel of a picture taken by the camera.

With these parameters the deflection of photons after leaving the lens system can be described, i.e. the aberration of the system from a perfect camera or “camera obscura”. This part of the correction can be handled with a lab calibration (see camera calibration and Figure 5) and a correction within the project as part of the optimization of the alignment.

3.13.1.2 External orientation

The external orientation is the description of orientation of the camera in space during the opened shutter. The orientation is given by the parameters Ω_O, Φ_O and $K_{O,}$ commonly known as nick, roll, and yaw, respectively. These correspond to “nose down”, tilt left and right and rotating around the Z-axis, i.e. changing the azimuth. The other part of the external orientation is the location of the camera at the timestamp the image is taken given as X, Y, Z, which in this project correspond to the latitude, longitude, and height. This data can be supplied from the FC, but it is not necessarily needed as they can also be calculated in the alignment process.

3.13.1.3 Bundle adjustment

With the use of bundle adjustment the pictures are connected to each other, making it possible to reduce the unknown parameters, overdetermine them, and providing the possibility of a simultaneous calibration as described above. The errors of the fitting are minimized with an iterative process for minimal errors. The bundle adjustment requires an overlap in direction of flight, as well as an overlap parallel to the flight direction. The basic principle of bundle adjustment is based on several pictures showing the same features, so-called tie points, which can then be tied together, a process called aerotriangulation. The GCPs (red points) ensure a correct placement of the model, while the tie points (gray points) connect the pictures as just described (see Figure 18). The tie points also reduce the amount of GCPs needed, a huge advantage as the GCP placement in the mapped area as well as in the calculated model takes a lot of time and effort, and sometimes locations are too dangerous or impossible to reach.

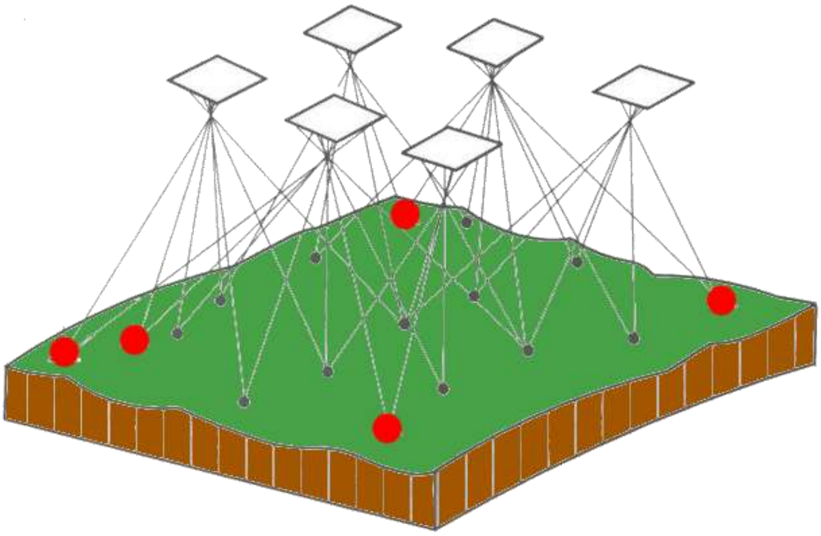

Figure 18: Model of aligned photos; tie points (gray) and GCPs (red dots), modified after Kraus (2004)

4 Testing

4.1 The quarry

4.1.1 Geology

The excavated material of the quarry is a granite. It is overlain by sandstones. The cementing is quite weak. In the older part of the quarry, where excavation was stopped, some crosscutting mafic dykes are exposed. Erosion removed parts of the sandstone overlay which is an important aspect for the operation of the quarry, as removing the overburdening sandstone overlay would be cost intensive.

Figure 19: Typical outcrop situation in the quarry; granitic intrusive countryrock (red) is overlain by sandstone (yellow) and cross-cut by a dyke (black), an anthropogenic wall serves as a security measure (brown); note: secondary wall at foot of the bench to restrict rock fall

4.1.2 Operation of quarry

For excavation, the overlying sandstone has to be removed, thus the parts of the quarry with little to no overlay are favored. The quarry has a workshop and a processing facility for crushing and sorting at its entrance. The office buildings are found there as well. In the old part of the quarry the removal of the sandstone became too expensive, so excavation was stopped. Following, that section of the quarry was partly used as a dump for construction waste while the other part is used as storage for pre-sieved, ready-to-use material such as gravel, sand etc.

The third part is the active quarry. There, the benches are about 20 m high and active excavation takes place.

4.2 Flight mission planning

For planning the missions the weather forecast was monitored carefully; days with calm to low wind were chosen and used for the flights. Being on a slight slope with a canyon type surface the local wind was observed with test flights, and in the following flight planning the detected wind directions were used to minimize the drift of the UAV. At the same time the signal range had to be taken into account as the quarry is oblong and the base station is best placed at a cliff for a safe and easy takeoff. So a two stop approach was used to have a decent security buffer.

Figure 20: Typical ground station, a standard laptop with UHF serial modem; note the long cable to avoid interference from the USB bus to the modem

The mission planning itself was done by 'MissionPlanner' (Michael Oborne, 2014), a software allowing to plan a flight with only a few mouse clicks. The user simply defines waypoints witch are coupled with an order. Usually, a waypoint is approached at a certain height and the UAV passes it in a defined radius before it jumps to the next. The waypoints can also trigger a number of routines, e.g. fire a camera, deploy a landing gear, etc. The dataset with the waypoints and orders is then uploaded either via serial-over-USB connection, an ultra high frequency (UHF) modem or a Bluetooth connection. A remote upload with the UHF modems and the UAV being in the air was tested but not successfully accomplished. The distance in which a successful transmission can be achieved was very low (< 30 m). A higher wattage or better antennae should compensate these problems.

4.3 The flight

The UAV is hand-launched and then flown to a certain height. There, some basic movements are tested. If the operator is satisfied with the performance, the mode switch is put into auto mode and the APM executes the uploaded mission automatically. The operator can now follow the plane on the display and on the ground station. In case of unforeseen complications the operator can abort the mission and fly fully manually to the landing strip. If everything works as planned, the UAV circles over the last waypoint (WP) and awaits further orders. The operator lands the UAV and can then extract the camera with the pictures.

Figure 21: Helical right hand polarized 5.8 GHz video antenna, used for better reception at ground station

Figure 22: Clover leaf right hand polarized 5.8 GHz video antenna, usually used with a (RP-)SMA connector, working as a remote antenna on the UAV

5 Processing of data

The pictures taken by the camera are extracted from the flash memory and saved. They are sorted to remove blurry and other unsuited images as well as unwanted exposures like the ones taken in a steep turn.

In the following, the used program packages are shortly introduced, first the two photogrammetric suites followed by the evaluation software.

5.1 Agisoft Photoscan

A separate copy of the images is created and loaded into the commercial software Photoscan (Agisoft Photoscan, 2013). The workflow in the software is documented very well at the homepage of Agisoft and is subject to change. Therefore, a look at that resource is always helpful. The basic principle is the same with all releases. In the following, this process is illustrated with a set of four pictures. The same process applies to bigger data sets as well.

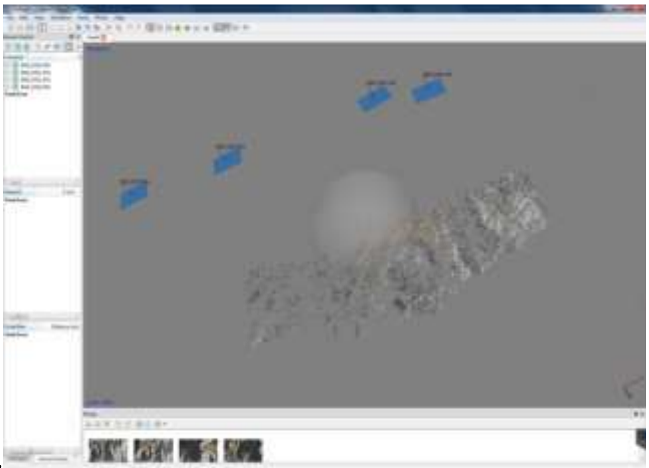

Figure 23: Aligned photos; note the sparse cloud generated and the projected photo-positions where the pictures were taken

The software first loads the pictures and creates thumbnails for easy recognition. The pictures are then aligned, which is a process of finding distinct points on every picture and consequently trying to match them with the next picture, see Figure 23 . As the software has to compare every picture with every picture the user is encouraged to use GNSS info if it is available. A basic GNSS info in the EXIF-tag helps to reduce the time of this process significantly as it enables the software to pre-select the images to compare in the process.

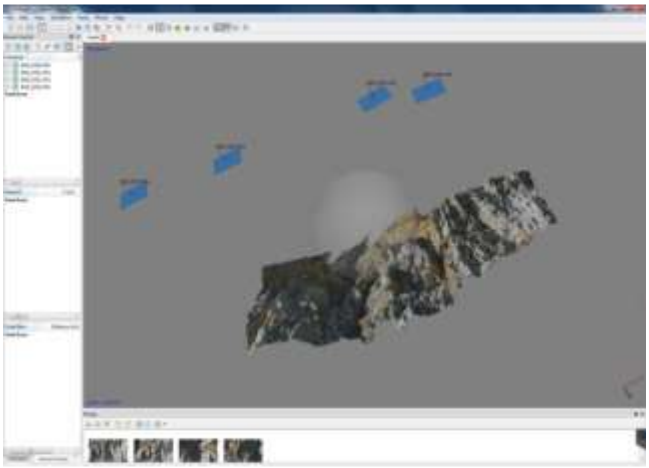

Figure 24: Calculated dense cloud; note that the single points are not distinctly visible due to the high number of points

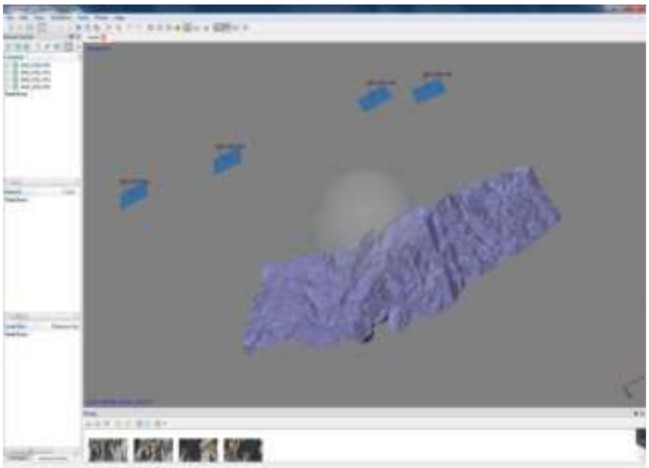

Figure 25: Surface model based on dense cloud; coloring turned off for better visibility of the 3D structure

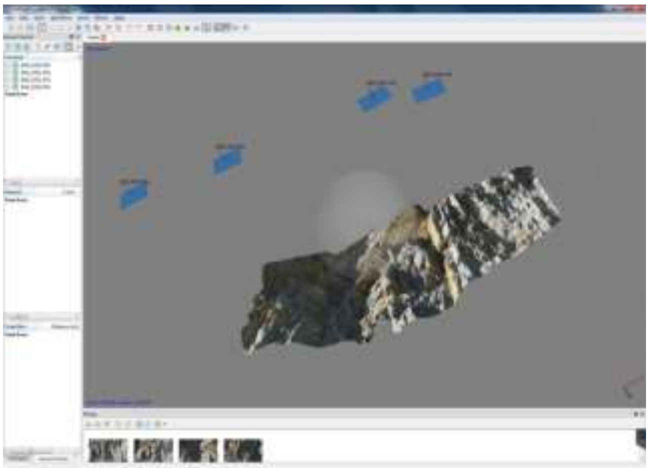

Figure 26: 3D model with texture applied

The resulting point cloud is already colored in RGB colors taken from the pictures (see Figure 24). The alignment can be checked for outliers with the help of the projected positions of the photo-shots. Now the GCPs can be marked in the pictures to increase the accuracy of the model. This step is not necessary but it helps enormously in reducing artefacts, warping effects etc.

Subsequently, the point cloud is densified through two steps, sparse and dense cloud. Finally, a triangulated network (TIN) (Figure 25) is created from the software; the TIN is also already colored based on the available color info from the alignment process. The digital surface model (DSM) can be exported now.

To get a high resolution-orthophoto, all pictures have to be projected on the surface model. In Photoscan this is just another automated process to be initiated. The model now has a decent texture (Figure 26); the corresponding orthophoto can be exported as well.

5.2 VisualSFM and CMVS

The second approach used was the freely available combination of visual structure from motion in short VSFM by Wu (2007, 2013) and Wu et al. (2011) and clustering views for multi-view stereo (CMVS) (Jancosek and Pajdla, 2011). A major difference between the Agisoft package and this one is the use of GPU framework: while Agisoft uses the GPU brand´s independent OpenCL, the VSFM software relies on compute unified device architecture (CUDA), a NVIDIA proprietary framework. The workflow was derived from Duffy (2014). An comprehensive video is available at the page tutorials.

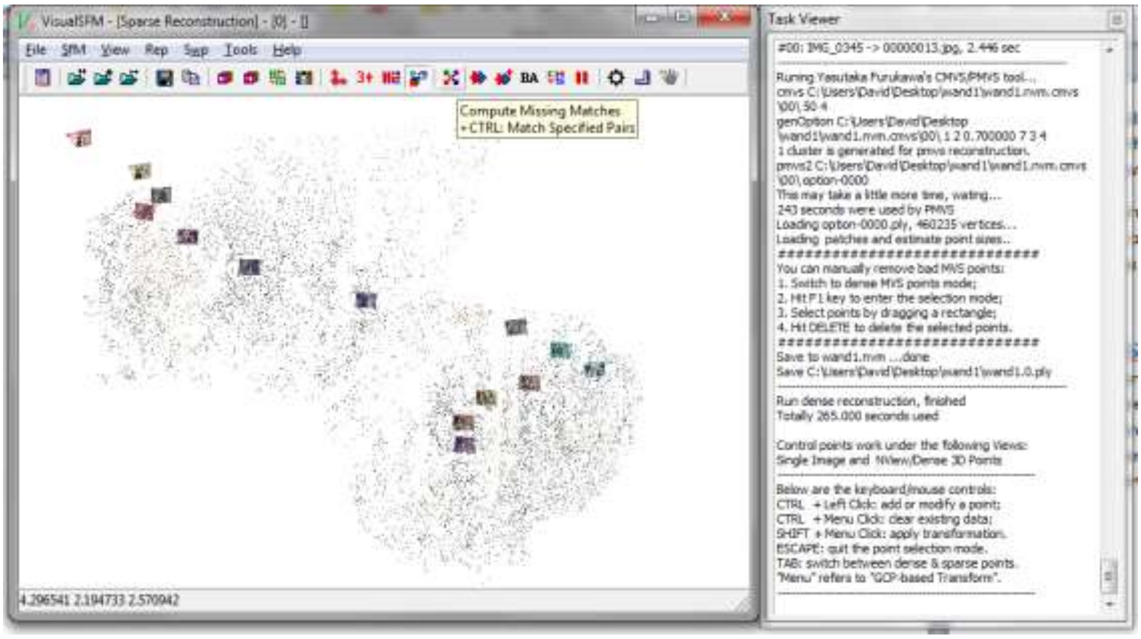

Figure 27: Sparse reconstruction with VSFM

The workflow is similar to that of Agisoft Photoscan. The photos are loaded into VFSM directly generating thumbnails; now the pictures are aligned with the scale-invariant feature transform (SIFT) routine. Following the SIFT routine the user can process a sparse cloud (Figure 27), which allows a first overview of the survey area.

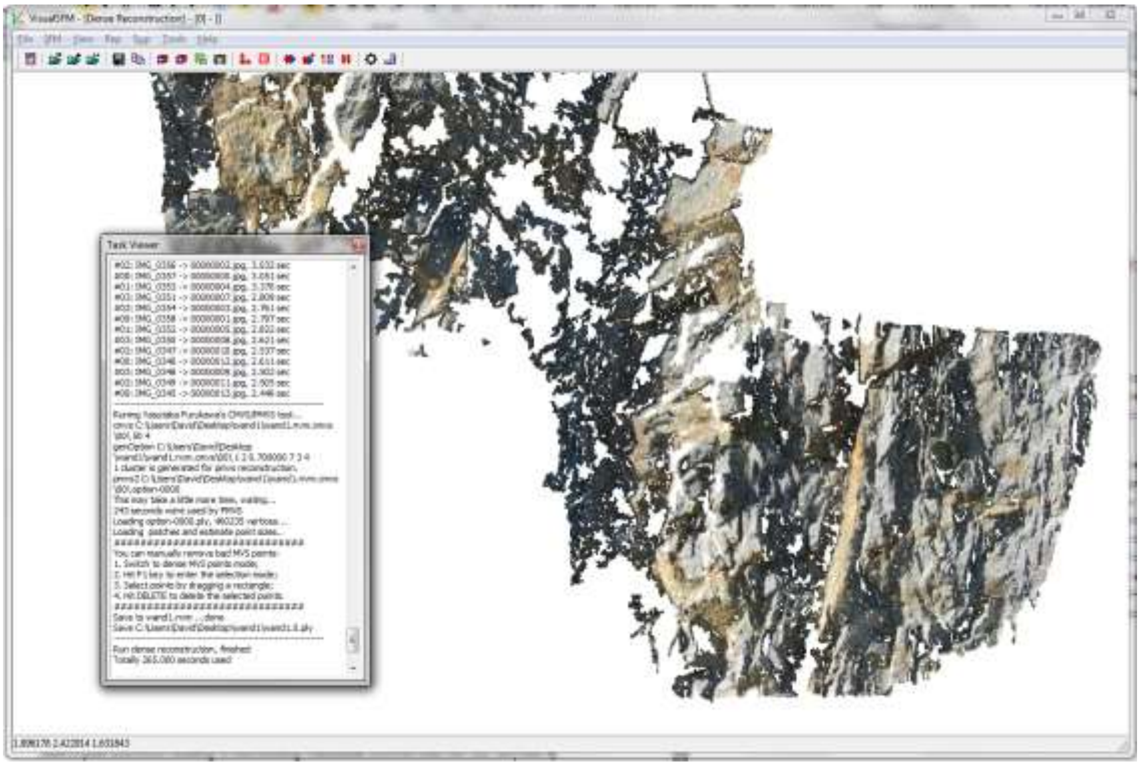

Figure 28: Dense reconstruction with CMVS initiated within VSFM

Now, similar to Photoscan, a dense reconstruction can be initiated with the CMVS routine (Figure 28). The results can be reviewed after processing. At the latest, the user will now recognize that the VSFM approach requires considerably more pictures to keep up with the amount of detail produced in Photoscan. The data can now be processed in two ways: firstly, for 3D objects, e.g. details of a quarry bench, or secondly, processed as an orthophoto. If the data falls into category one, the data is loaded into Meshlab (FGT, University of Pisa, 2005), applying a Poisson-construction of a mesh (Figure 29, Figure 30). The data is now ready for assessment. The user should take care as this dataset is still considerably low in detail. If the data is to be processed towards a decent orthophoto, the dataset is now converted to a CMP-MVS readable format. CMP-MVS (Furukawa and Ponce, 2010; Furukawa et al., 2010) is a command-line called process. It is initiated, given the project folder and the respective dataset and then calculates the digital surface model (DSM) and the orthophoto. The CMP-MVS package is also capable of exporting much more, like flyby videos of the surveyed area. Being just by-products, they still use a lot of CPU and GPU time. The user is thus encouraged to look into the to-do-list (MVS.ini) and adjust the called subroutines to the project's needs.

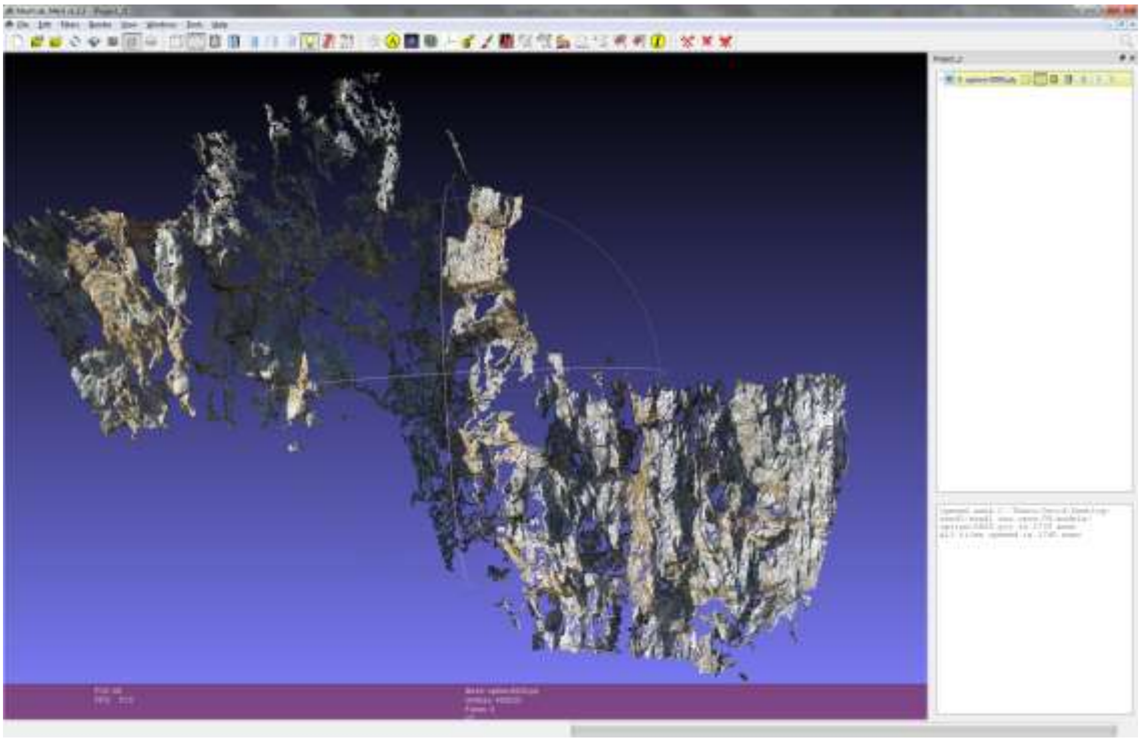

Figure 29: Point cloud loaded into Meshlab

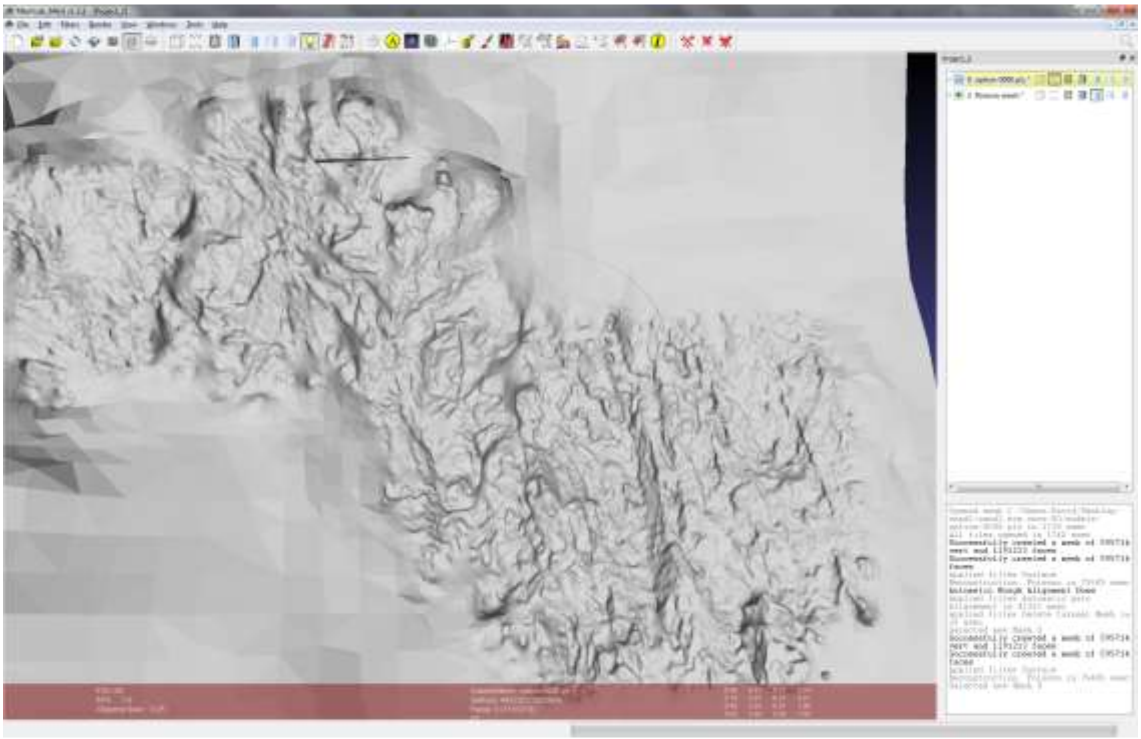

Figure 30: Surface created with Poisson-algorithm; note the surrounding wall is created automatically by the process

5.3 3Point script

For the structural evaluation of the produced 3D data, a MATLAB (MathWorks, 1984) script was used. The code was written by Grasemann (2011) and later modified to match the data format Meshlab produces.

5.4 MATLAB approach

In order to evaluate the joints and their surfaces, a part of the generated surface model was exported and loaded into MATLAB. The dataset, given in form of a *.PLY–file, was then displayed. A small code was written to extract the coordinates of three points the user specifies by clicking. The data is then processed by the function supplied by Grasemann (2011), which generates the dip and dip-direction of the surface defined by the three points.

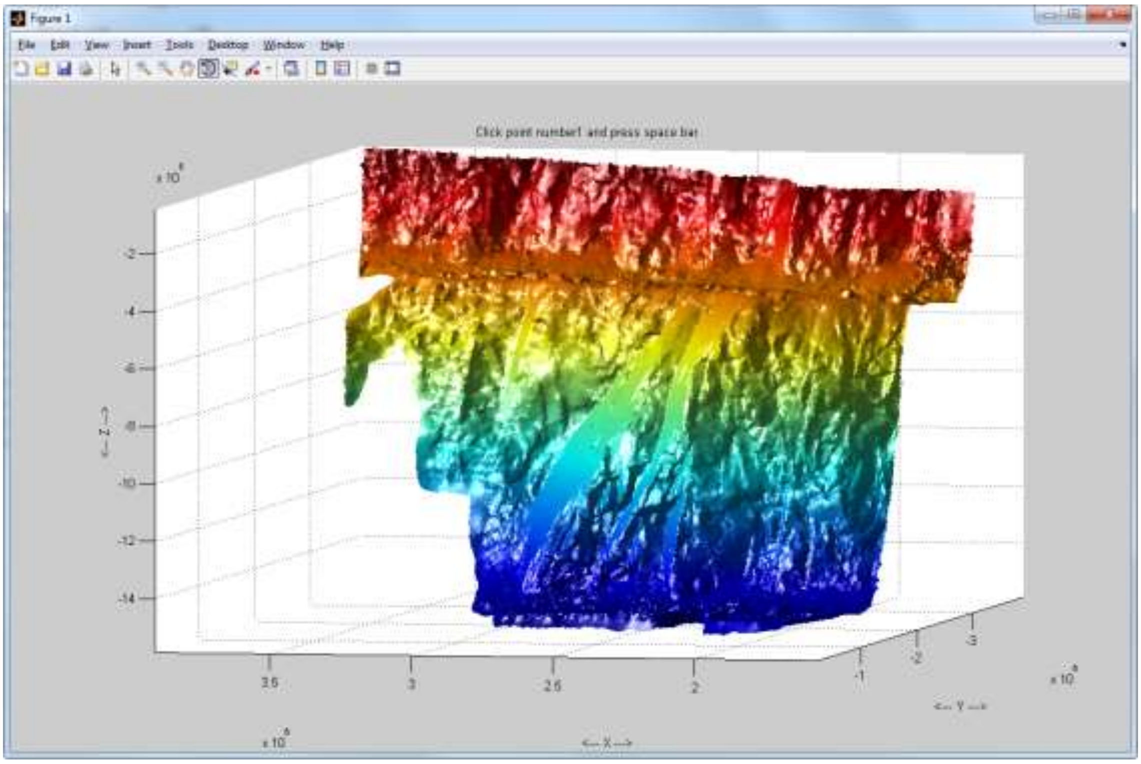

Figure 31: Part of bench loaded into MATLAB for use with 3-point method

5.5 Meshlab approach

Meshlab is a freely available open source 3D tool which allows the user to display 3D content; for further information see meshlab.sourceforge.net (FGT, University of Pisa, 2005). For this approach, the data exported from Agisoft Photoscan was transferred as a *.PLY file. The data is loaded into Meshlab and the mouse is used to gain orientation. After finding an appropriate area of interest, the point-picking (PP) tool can be used to mark points and later export them as a *.pp file (Figure 32). This file can be loaded into Excel, where the raw XYZ coordinates can be extracted with the use of the ‘ ” ‘ as delimiter, saved as an*.xls file and loaded into the MATLAB code described above. The changes necessary to allow loading datapoints from these arrays were made in the code.

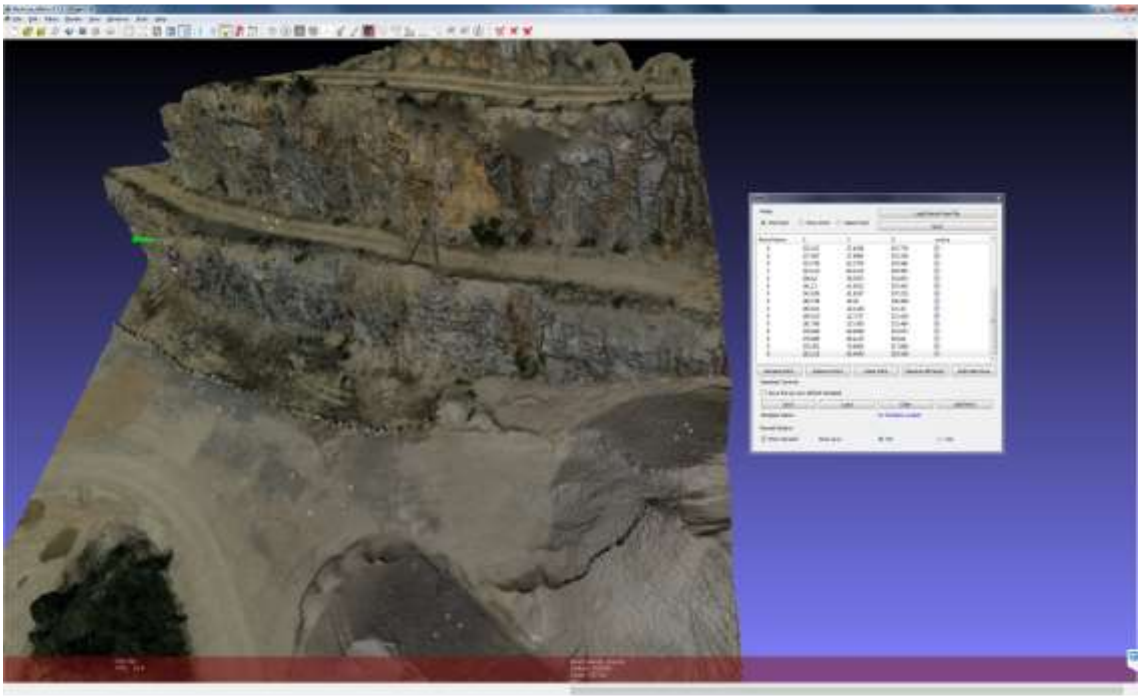

Figure 32: Data loaded into Meshlab, dialogue opened for point-picking (PP)

5.6 The ArcGIS approach

The third approach to the 3D evaluation was the use of Asmar’s port (Asmar et al., 2014) to Python for a use in ArcGIS (ESRI Inc., 1999). The script is basically the same as the MATLAB script by Grasemann (2011) described above. The main advantage is the seamless integration into ArcGIS, resulting in a better and faster workflow for the user.

The DSM and the orthophoto are loaded into the project. It is recommended to work with a geodatabase and a connected folder due to randomly appearing bugs, like software crashes, being unresponsive without obvious reasons. The script is introduced as a toolbox which asks for XYZ-data. This data is added through two other toolboxes the ‘add XY’ and ‘extract values to points’. The python code has to be edited to match the preferred data output location. The user then opens a new shape file and adds points to the shape file. For every measurement three points have to be placed on the same feature. The points need to be placed three at a time for every measurement. The resolution of the DSM should always be kept in mind to avoid too low spacing of the points relative to the DSM’s resolution which would lead to inaccurate measurements. The data is then processed through the script itself but within the shell of the model just created with the described toolboxes. The result is the same as above, a *.csv file with the respective centroids and dip/ dip-direction.

5.7 The Coltop3D approach

The fourth approach is a commercial software (Jaboyedoff et al., 2007; terranum, 2011) which is produced by a spin-off of the University of Lausanne. The software is originally planned as laserscanning-evaluation software for structural geology. However, as a point cloud is just a generic XYZ-coordinate table, it could be shown that it also works with point clouds produced by photogrammetry. The data is loaded into the software and is directly processed for the vertexes’ normal and eigenvectors. As this is not a default setting, the user has to take care to check these boxes; later processing is not possible. The calculated orientation is directly displayed with a rainbow color scale. Note, the density of the visible points can be adjusted with the pyramid button at the import stage. The increase of the point size does not really enhance the perception of the model.

5.8 Overview flowchart

The following flowchart in Figure 33 can help to keep track of the workflow used.

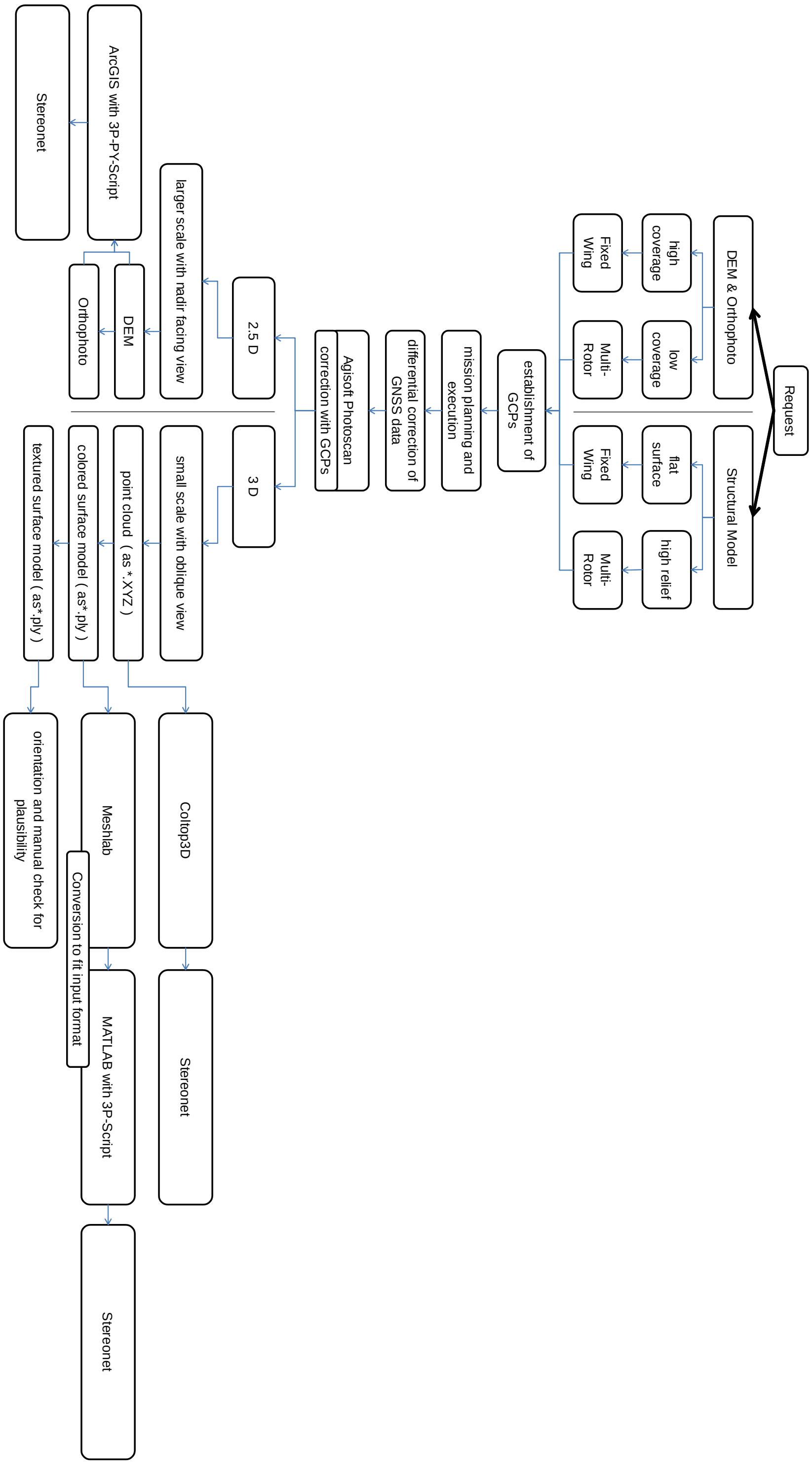

Figure 33: Flowchart of workflow

6 Results

6.1 Presentation of acquired data

The data set produced in this work is relatively big, not only in size but also in terms of resolution. Because of this the data in this chapter is displayed in several orders of magnitude. The whole extent and usability of the capabilities do not transfer to paper but by showing the different scales separately, the author hopes to accommodate the issue as good as possible.

In the first parts of this chapter, the first very inspirational steps are shown, although having been done in a totally different area: 6.1.1 Overview models and 6.1.1.1 VisualSFM and CMVS. In the following (6.1.1.2 Agisoft Photoscan) the main work, the overview model of the already described quarry is shown. Additional detailed data and processing related information from the quarry are shown in 6.1.2 Visualized metadata of the models and 6.1.3 Detailed close-ups.

In a third part, the structural application and the associated evaluation is presented: 6.2.1 Volumetric data and 6.2.2 Structural data.

Note: North is always at the top of the figure until noted otherwise.

6.1.1 Overview models

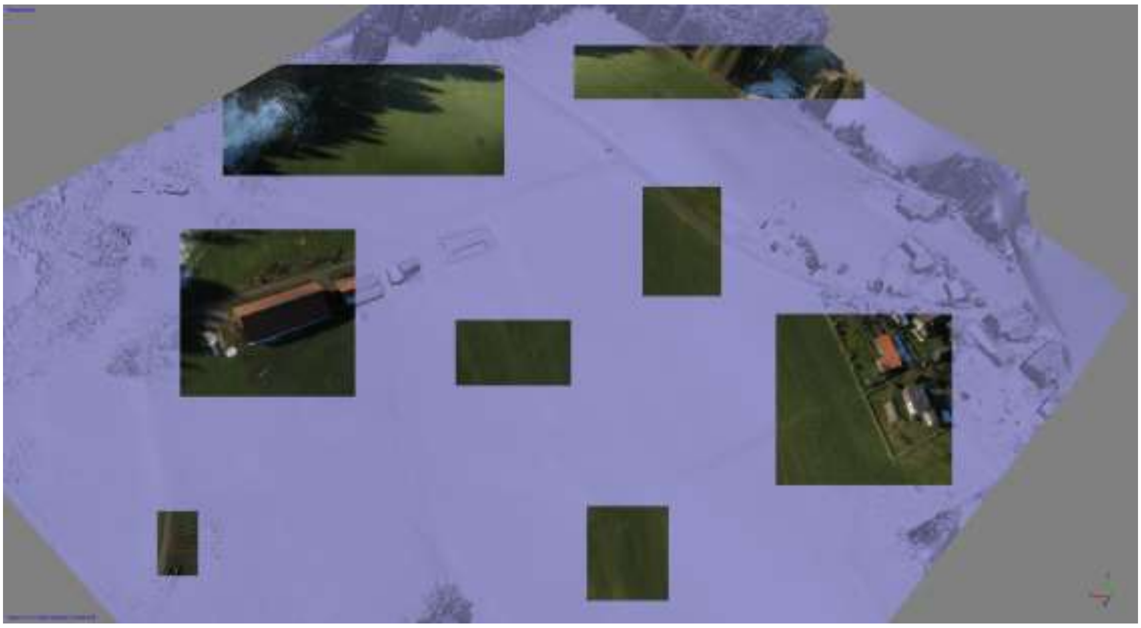

Figure 34: First aerial photos, revisited with Photocan; shaded model with partial overlays of projected photos

The model shown in Figure 34 are the reprocessed first pictures taken from the first UAV (Bixler 2) used in this project. Note without any prior knowledge the pictures still resulted in a usable model, clearly for rough reference. No flight assisting functions, like altitude-hold, were used except for displayed GNSS -speed and -height.

6.1.1.1 VisualSFM and CMVS

The first part of the results includes the first steps made with the fixed-wing Bixler2 UAV. Figure 34 shows the first mission revisited with Photoscan after switching to this software package. The following data shows the first model, which was crucial to the decision to execute this project (Figure 35). The data was processed only with the VSFM and CMVS approach. The data shows a hilly area near the border to high mountains. A small village (see Figure 37) surrounded by grassland and hayfields can be observed, which in turn are surrounded by small patches of coniferous woods. The resolution of the orthophoto is always below 20 cm, mostly even lower. The DSM shows medieval plow terraces, marked in Figure 35 (blue). The woods cause problems with height calculation resulting in a distorted heterogeneous display. The black spots on the orthophoto represent areas of insufficient overlap. In the eastern part warping is visible. Overlap and resolution can be estimated with the qualitative color-ramp in Figure 36.

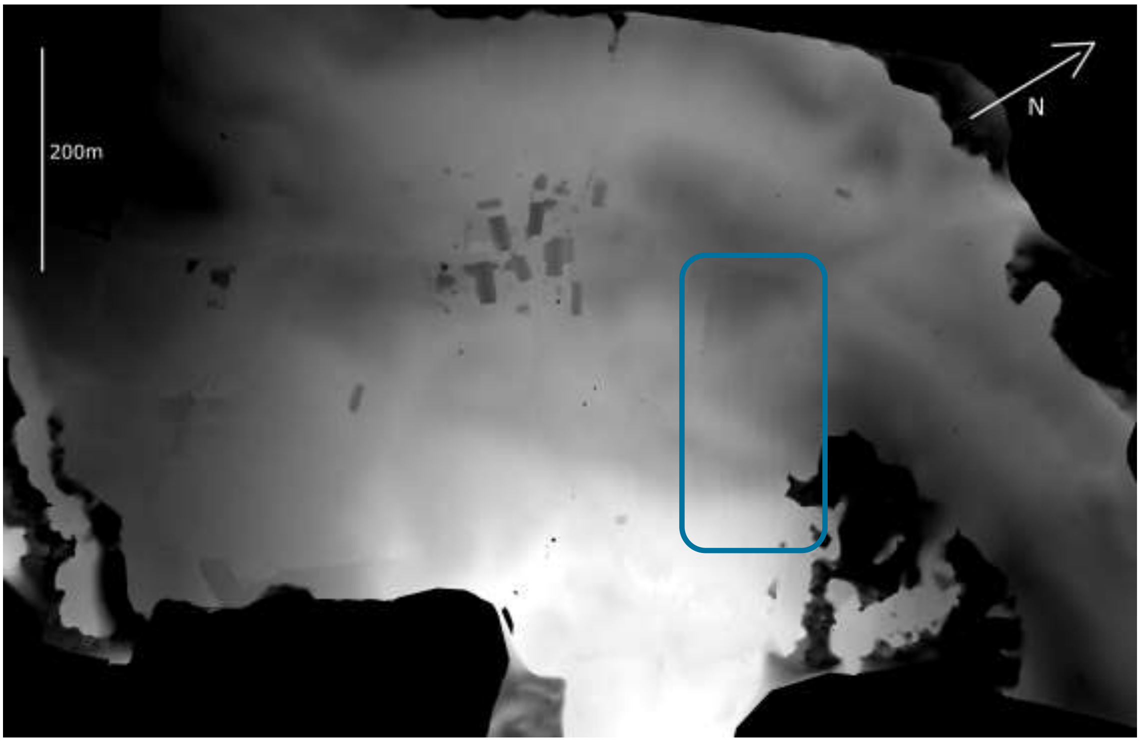

Figure 35: First self-processed model with VSFM and CMVS; DSM

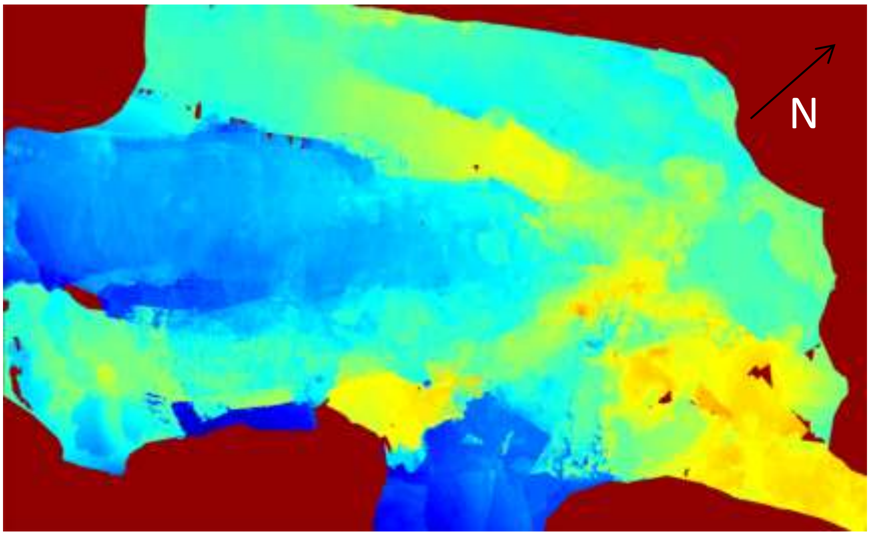

Figure 36: First self-processed model with VSFM and CMVS; qualitative estimation of overlap for DSM, blue-small overlap, orange- high overlap (red - no data)

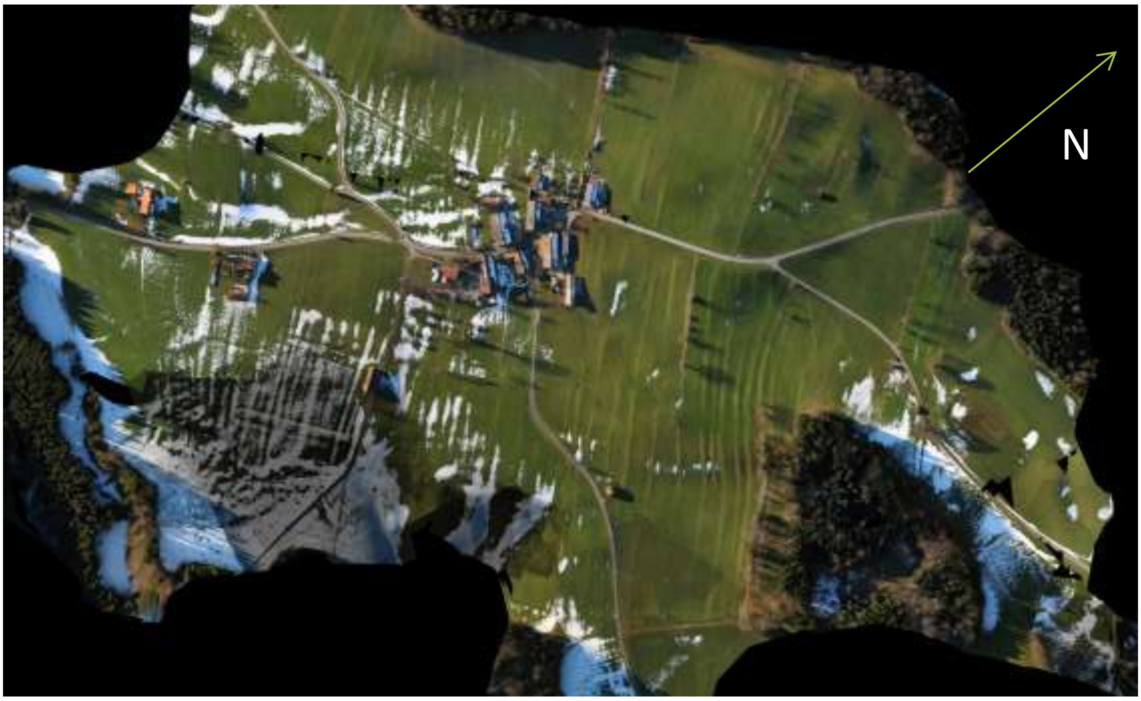

Figure 37: First self-processed model with VSFM and CMVS; orthophoto

6.1.1.2 Agisoft Photoscan

In the following the data of the quarry, the main part of this work, is presented. The 3D model of the quarry was produced based on the data collected using the fixed-wing Finwing Penguin UAV. Photoscan from Agisoft was used to process the data. The main interest was in the old and the new part of the quarry, while the entrance area with the administrative buildings was of less interest. Consequently, the coverage differs in the various parts of the overall model. The mean resolution for the orthophoto is lower than 5 cm, although some areas have a lower or higher resolution depending on the flight height. The resolution of the DSM is at least lower than 15 cm in most parts. The same fluctuation of the flight height applies to the DSM, as the resolution differs from one area of interest to another. The overlap and GCPs are shown in Figure 41. A colored model (Figure 38) and a hill-shaded model (Figure 40) are shown as displayed in Photoscan, the respective orthophoto is shown in Figure 38. Accuracy statements can be found in the Appendix, see Table 5 for the parameters of the acquisition of the GCPs and Table 6 for the GCPs errors and projection statements of Photoscan. For the placement of the GCPs a mean error of 1.6 m was calculated, for the horizontal and the vertical displacement of the model at the GCPs location 0.8 m and 1.1 m were calculated, respectively.

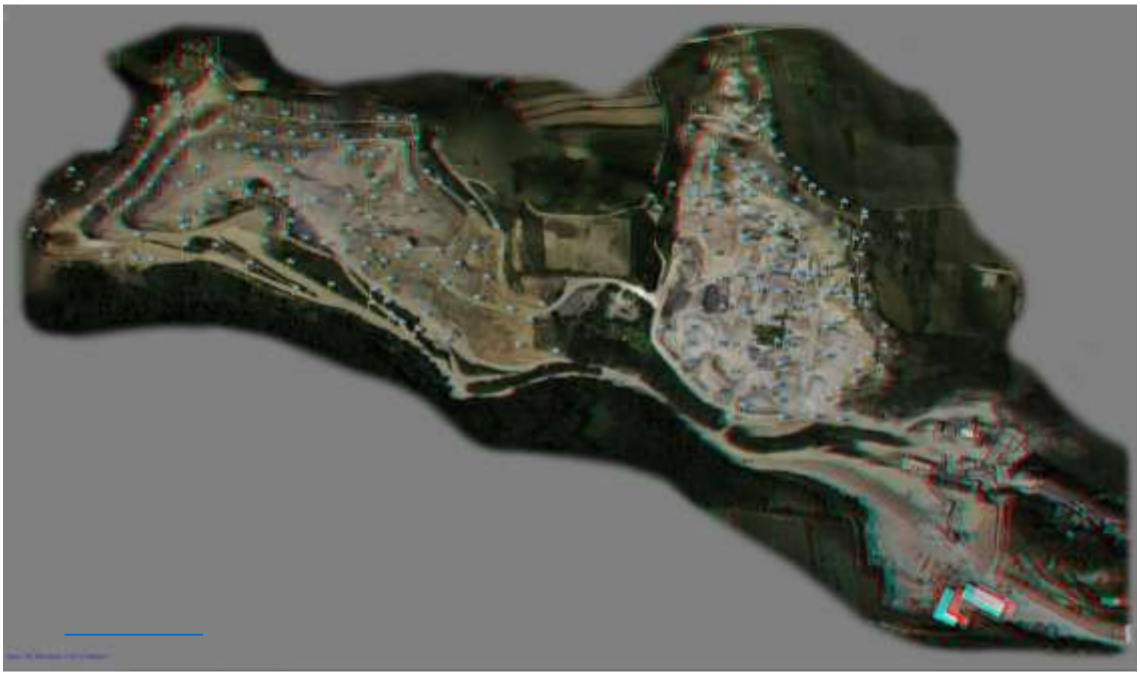

Figure 38: Colored 3D model of the quarry with marked GCPs; blue scalebar 200 m (with anaglyph vision, use red-cyan glasses)

On the orthophoto the quarry itself can be seen. It is surrounded by woods, farmland, and vineyards. The same problematic as described above is seen in the model with woods not displaying correctly; a similar effect is visible in the most western part of the active quarry. Another problem caused by insufficient overlap is visible in Figure 44. It results in the model distorting to unclear shapes, most often cones and other warping effects. In areas where these artefacts do not occur the orthophoto is very detailed and has a very high resolution, as high as 1 cm/pixel. The warping of the orthophoto is minor and, if visible, due to the projection or draping of the photos on certain areas and shapes of the model. This is particularly observed in areas with dominant relief changes over small distances where the height-field setting (calculation technique within Photoscan, for details see manual of Photoscan) causes unwanted results (as described for the trees; also applies to other singular items like the feeding conveyer belt leading to the railway in the entrance area of the quarry). These minor issues are negligible, as they show up rarely and can almost completely be avoided if overlap and flight height are set accordingly. Bigger problems are water or any metallic, highly-reflective surfaces. On those the noise on the surface is definitively visible, as it results in a wavy to spiky surface in most cases.

Figure 39: Orthophoto of the quarry; original resolution 3cm/px

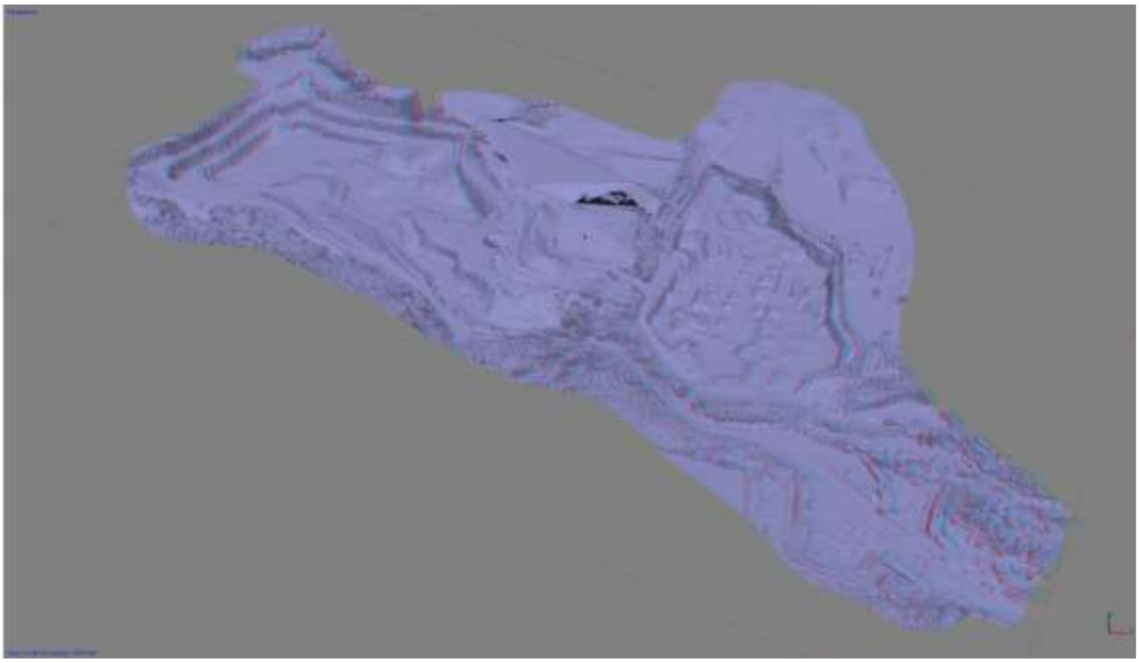

Figure 40: Model of the quarry (with anaglyph vision, use red-cyan glasses)

The model's quality and 3D capabilities cannot only be viewed at the computer with shutter glasses but also using colored paper glasses. If so inclined, the reader can gain a 3D impression of the 3D-suited images (as indicated in the image captions) by using red-cyan glasses.

6.1.2 Visualized metadata of the models

The accuracy estimations of the GCPs are listed in Table 5 in the Appendix. This data was produced by Trimble Pathfinder Office without any model. The data shown in Table 6, also found in the Appendix, represents the errors resulting from connecting the model and the GCPs. The estimations are taken from Photoscan. Figure 41 shows a visualization of the overlap, and the locations where photos were taken.

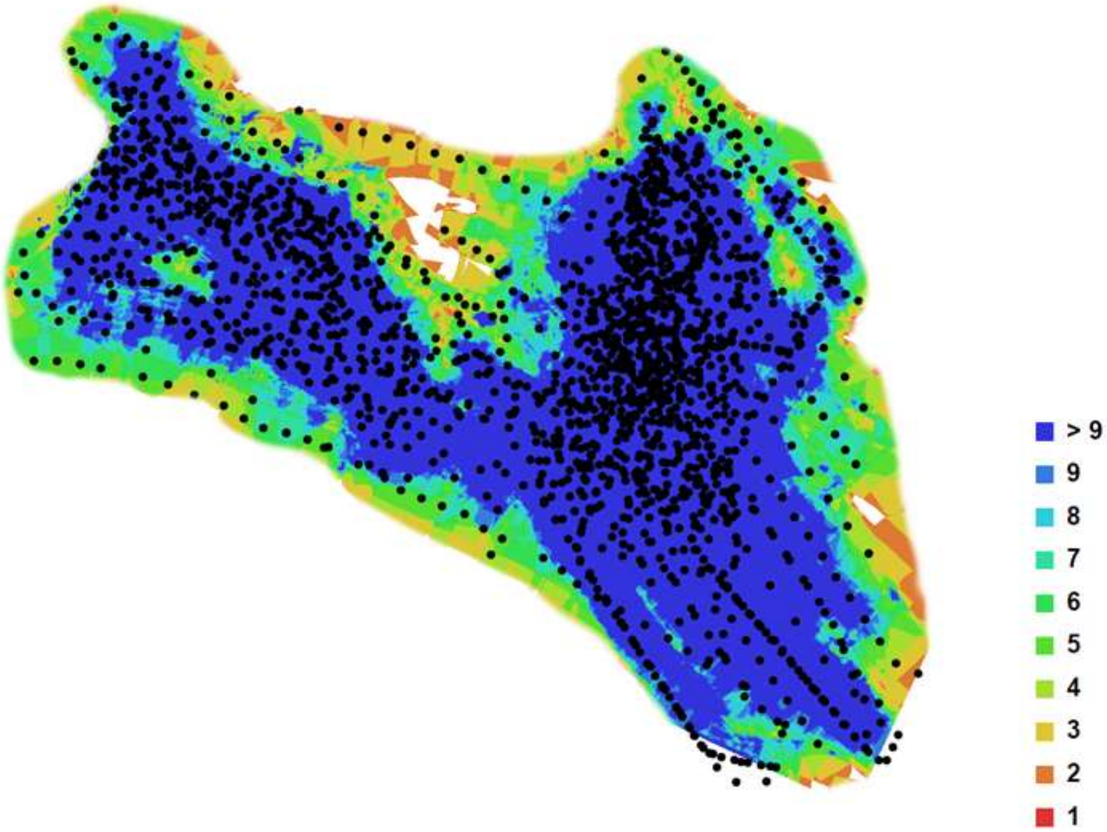

Figure 41: Sketch with overlap of aerial shots and GCPsthe legend gives the number of overlapping images

6.1.3 Detailed close-ups

In the following, some figures are shown that should allow the reader to gain an impression of the qualities - both positive and negative - of the model.

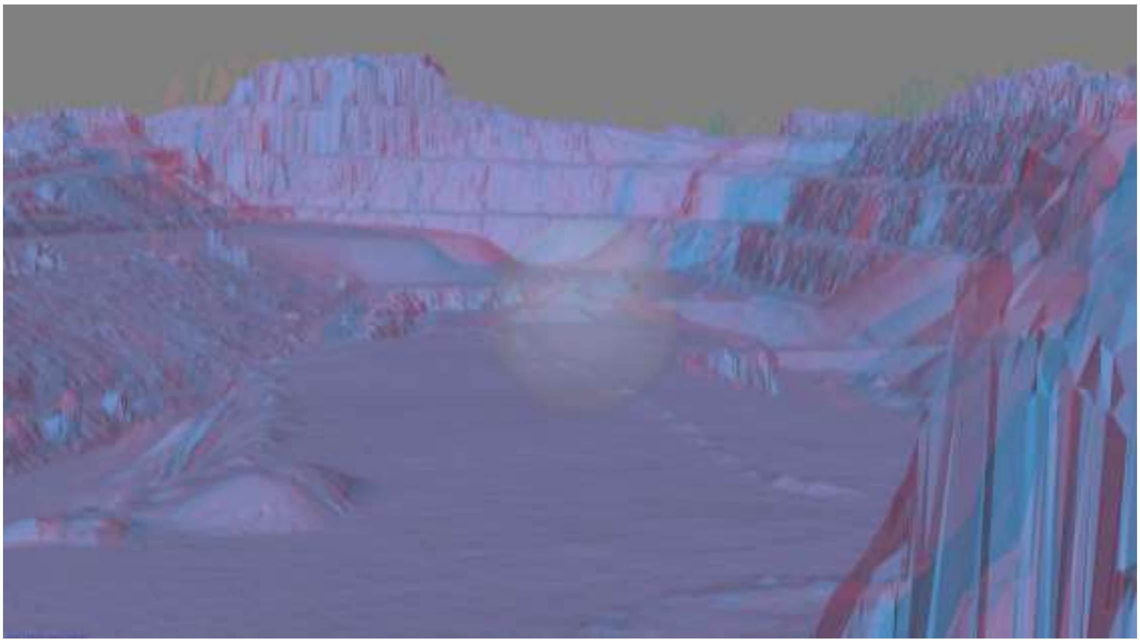

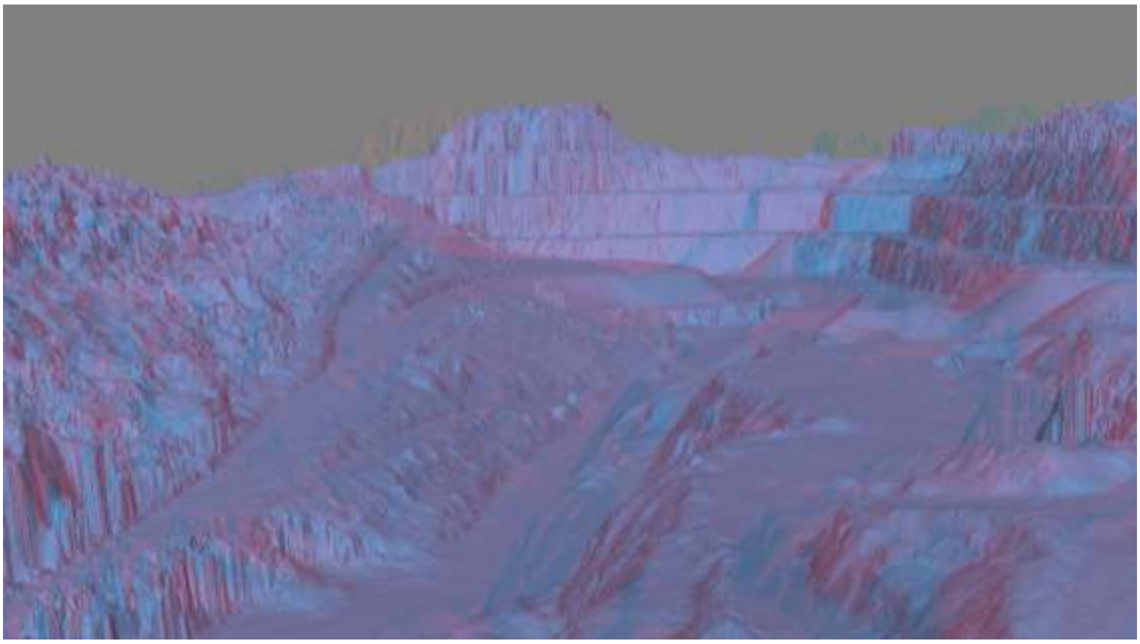

Figure 42: Artificial views into the active part of the quarry towards W (with anaglyph vision, use red-cyan glasses)

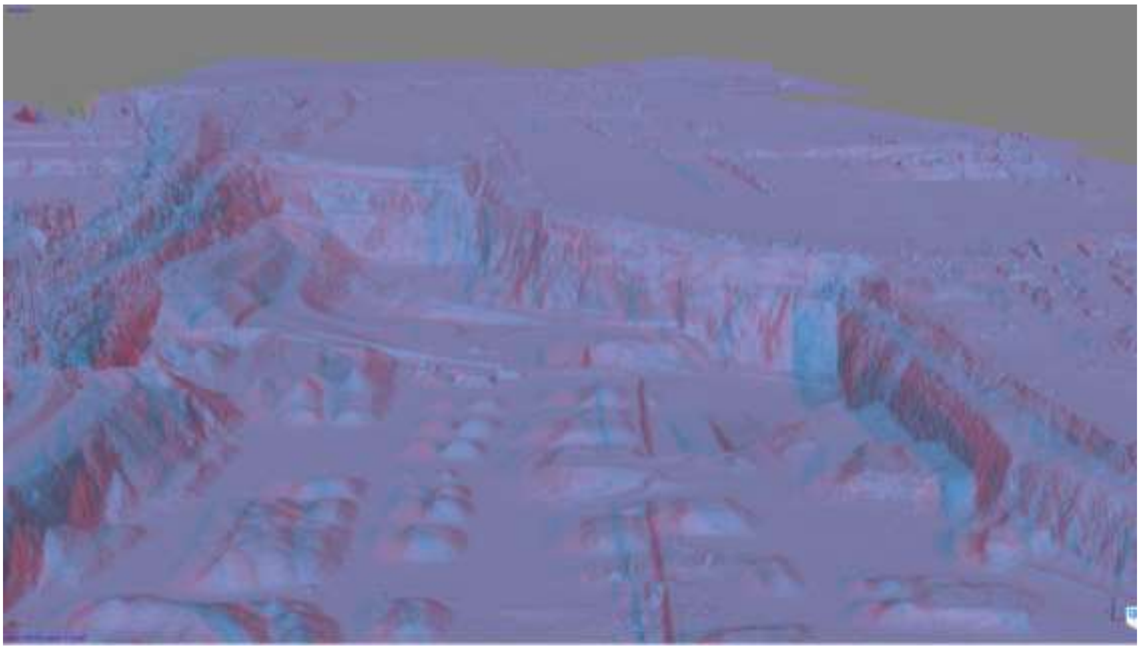

Figure 43: Artificial view into the old part of the quarry towards NNE (with anaglyph vision, use red-cyan glasses)

Detail images highlighting negative examples can be helpful showing the problematic sides of the project. The lack of overlap results in a distortion of the model as can be seen in the cone-shaped depression in Figure 44. In Figure 45 the ground appears to be very rough in some areas, which is also caused by insufficient overlap.

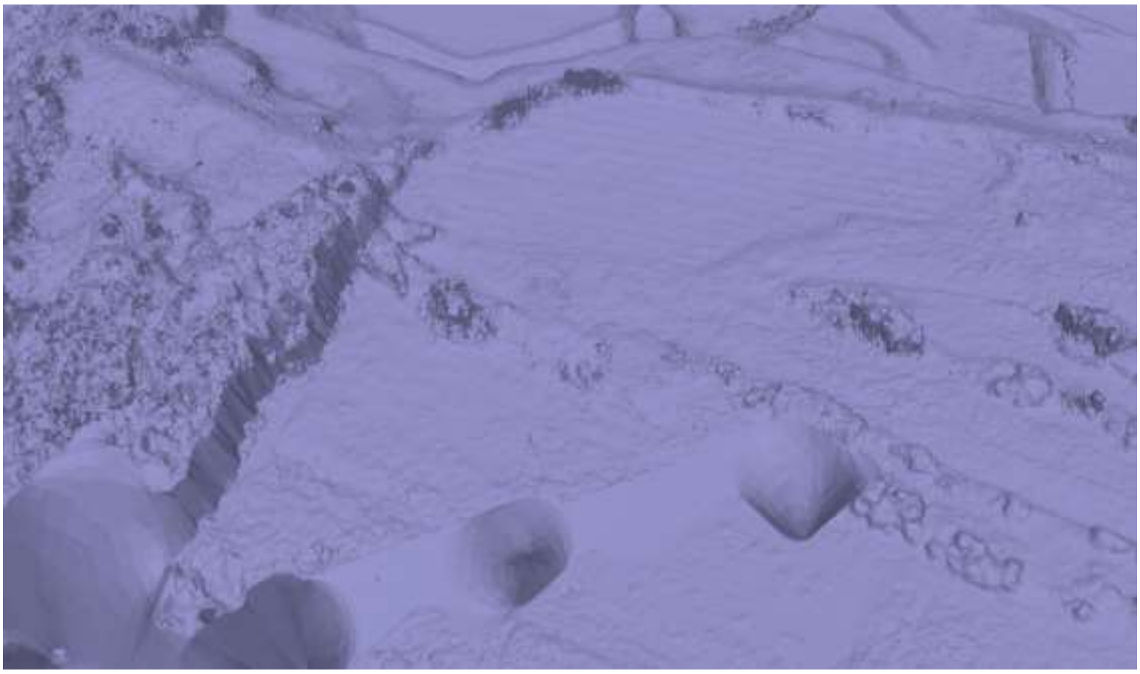

Figure 44: Issues caused by insufficient overlap; note the cone-shaped depressions and the irregular, unnatural woods on the left side

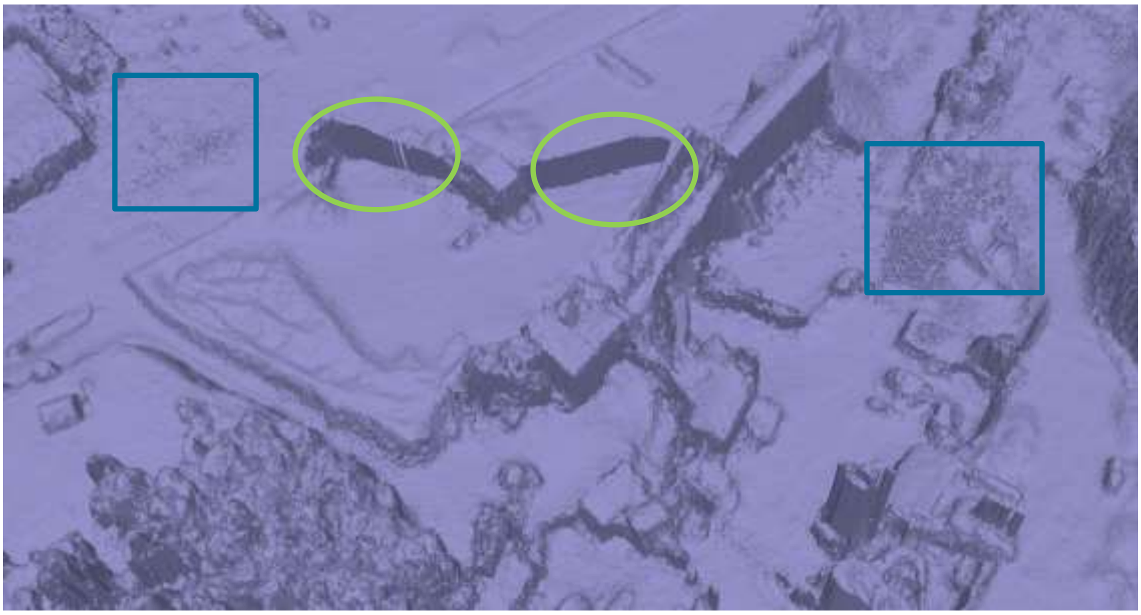

Figure 45: Issues: note rough ground (blue boxes), conveyer belt with filled headspace (green circles)

6.2 Examples of application

In this chapter possible applications of the 3D-model are presented.

6.2.1 Volumetric data

As a possible example for the use of the 3D model within the quarry, two volumetric measurements were done using a build-in function of Photoscan. For the measurement the structure has to be closed (with the fill-holes function), therefore a well-established edge around the area of interest has to be cut out. For the first measurement, a dump of construction rubble in the older part of the quarry was used. The volume was estimated as 11,500 m^3. A quick calculation (assumed 1.5 metric tons/ m^3) resulted in a weight of 17,250 metric tons for the dumped construction rubble.

As a volumetrically larger example, the volume of the whole active part of the quarry was measured. Problematic parts were left out for the estimation, avoiding overshooting of the closing function. The values may differ from the real excavated volume due to refilling with tailing-material, and due to the unknown original surface at the start of the excavation-operation. To reduce the effects of the first problem, dumps were cut and flattened. The unknown history of the quarry was handled with the assumption that the quarry is filled flat, i.e. that the top used to be a perfectly even plane. This is reasonable, as the surrounding morphology shows similar erosional physiography. The resulting volume estimation is 6.3 million m^3.

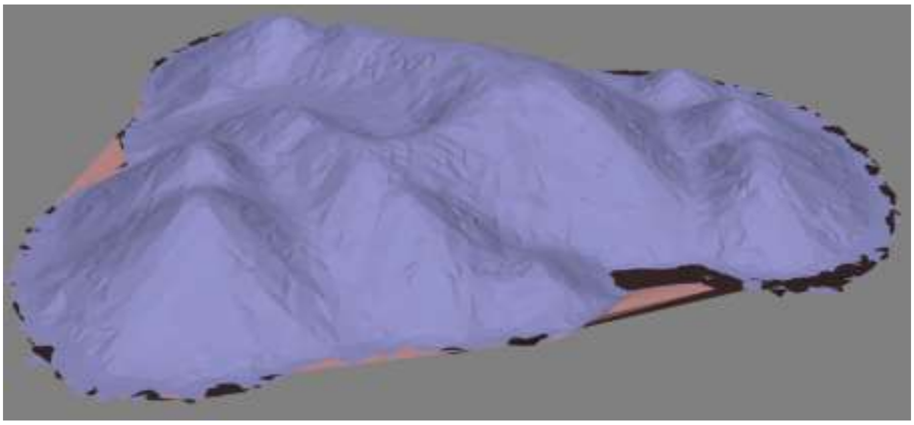

Figure 46: Closed model of the demolition-waste dump; note the skin colored 'base' put under the model

6.2.2 Structural data

The data in this chapter describes a possible structural evaluation of a 3D model. Part of it uses point clouds, the other already finished surfaces. Limitations of the software necessitated the assumption that all division surfaces can be treated equally, regardless of orientation or surface roughness. The aim was the evaluation of the workflow and the applications' usability. A verification of the softwares´ results with a control sample, measured with the mobile application Rocklogger (Turner-Jones, 2011), is presented below.

For the detailed wall evaluation a south-facing wall in the active part of the quarry was chosen. The pictures of the tricopters's flights and the matching fixed-wing UAV pictures were put together into one project to test the evaluation systems. An overview over the 3D model is given in Figure 47; the detailed textured model is shown in Figure 48. The best 3D-vision for the reader is achieved through the use of red-cyan glasses.

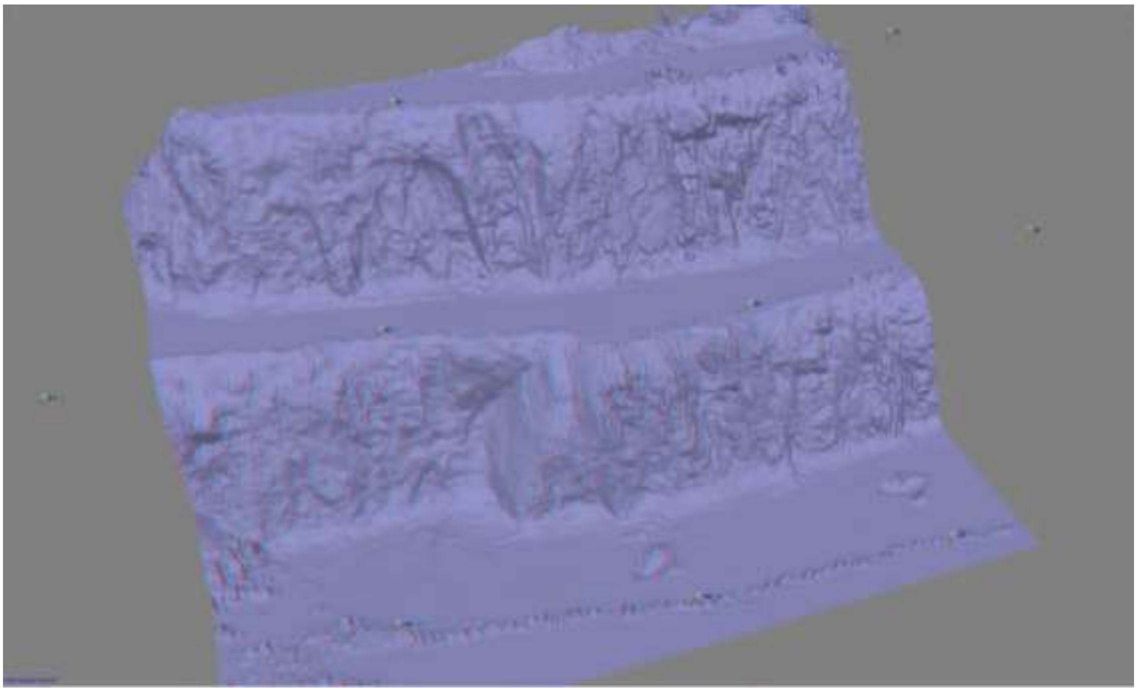

Figure 47: Detailed view of the wall with GCPs (with anaglyph vision, use red-cyan glasses)

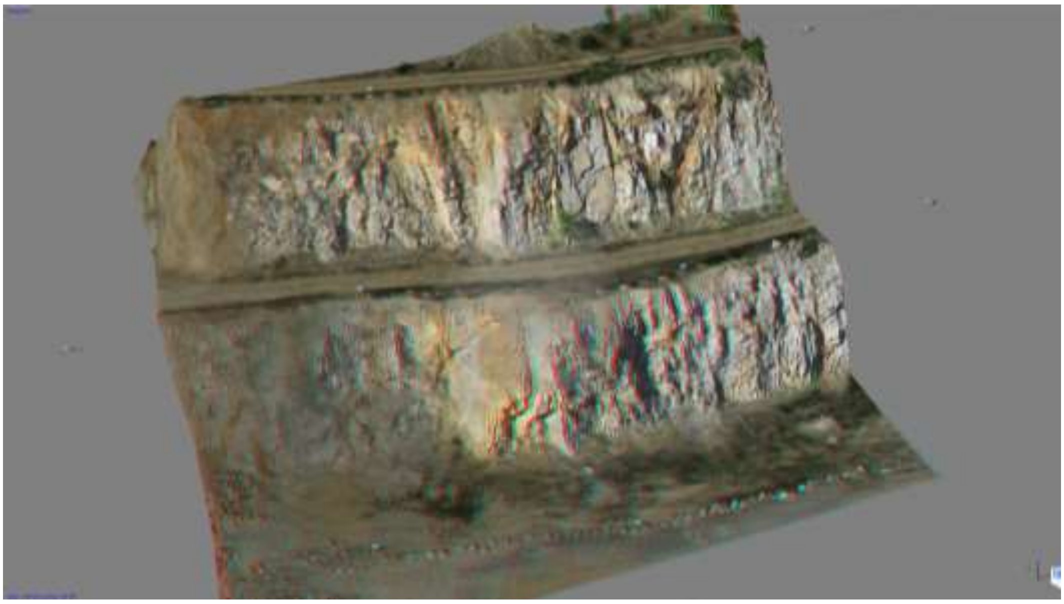

Figure 48: High-resolution view of the wall with texture (with anaglyph vision, use red-cyan glasses)

6.2.2.1 Coltop3D data

The data as seen in the software; the export of an image file failed due to randomly appearing errors, like corrupted data or crashing, thus rendering to software useless in this regard.

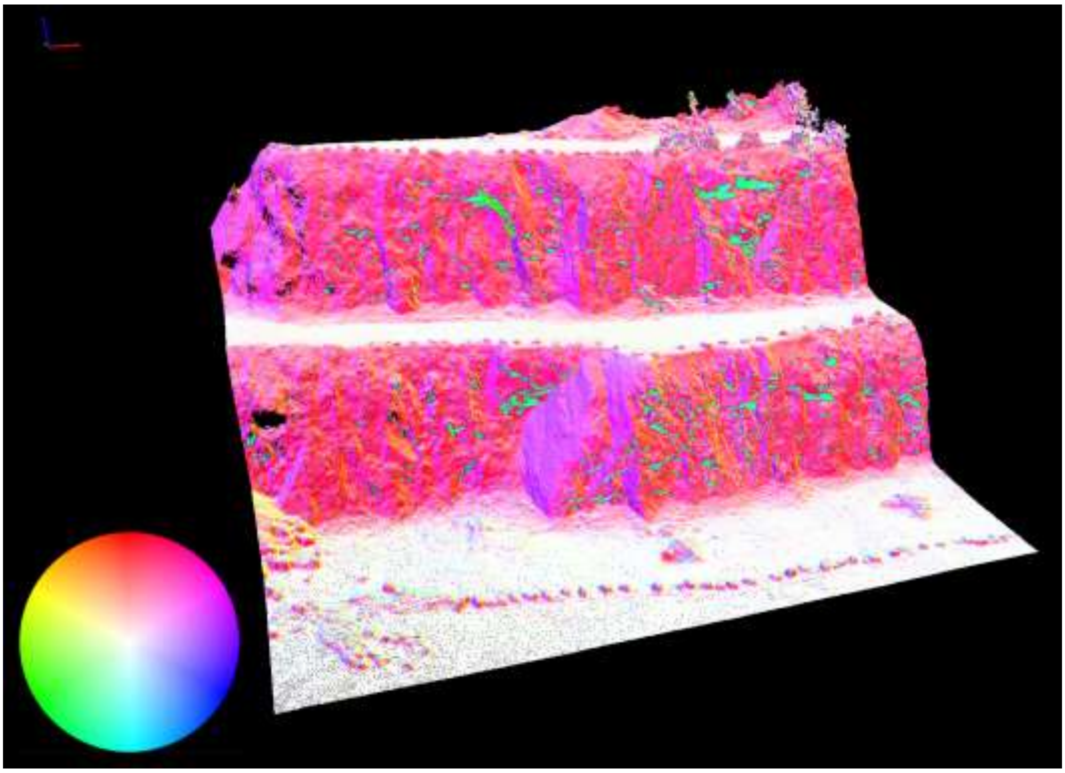

Figure 49: Coltop3D overview of section, colored pointcloud; the color key represents the lower hemisphere of a Schmidt's Net

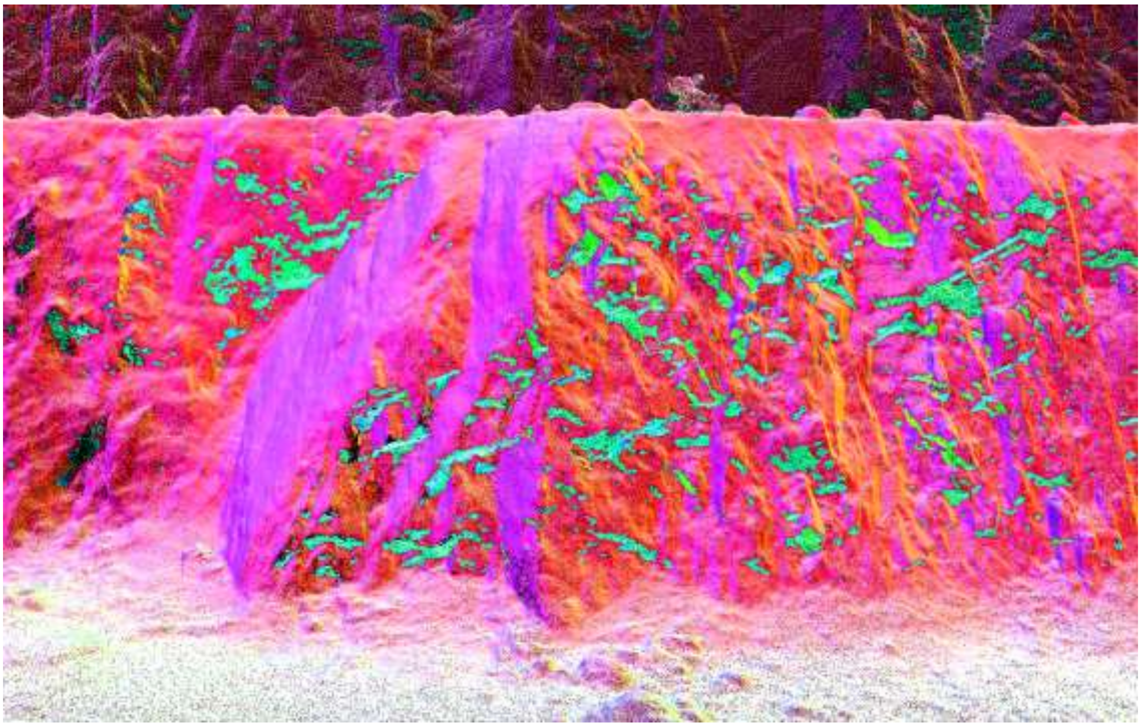

Figure 50: Detail of section with high point density

For good comparability, the individual sets of joints were separated and compared individually; note that the color-scheme was kept throughout the project (summarized by Figure 61). The dip-direction and dip-data extracted by and in Coltop3D is shown by a color-key on a lower hemisphere Schmidt's Net, see Figure 49. The data was pre-selected with the 'Direction and dip with Tolerance'-Tool and then optimized by hand for the parameters dip-direction, dip, and tolerance for good coverage of the joint.

The data manually measured with Rocklogger (Turner-Jones, 2011), a mobile application for android devices, was added to the diagram as poles and great circles; for better perception, the poles were underlain with a contour plot (1% area), e.g. Figure 52. The software used for these plotting-tasks is Stereonet, a freely available software (Allmendinger et al., 2011) (see Figure 51 - Figure 60). The amount of data produced for the modeled planes and poles is enormous (e.g. > 1.4 million orientations). It is impossible to plot these sets within reasonable time with available software. And even if it was possible the problem of the necessary high-end evaluation would still need to be solved. For a possible workflow see (Slob, 2008). For a slipstreamed approach, the data was reduced to 10,000 datasets. This still provides a comfortable safety for statistics, and in combination with the contour plot the data is easily minable. The poles for the modeled data sets were removed from the figures as they were obstructing the view onto the contour plot.

Because the datasets are, as described, very large, the data is not shown in a table for obvious reasons (> 5 million lines).

Note that the described dip direction and dip are highlighted with a surrounding tolerance. All values are given in degrees (0°-360°).

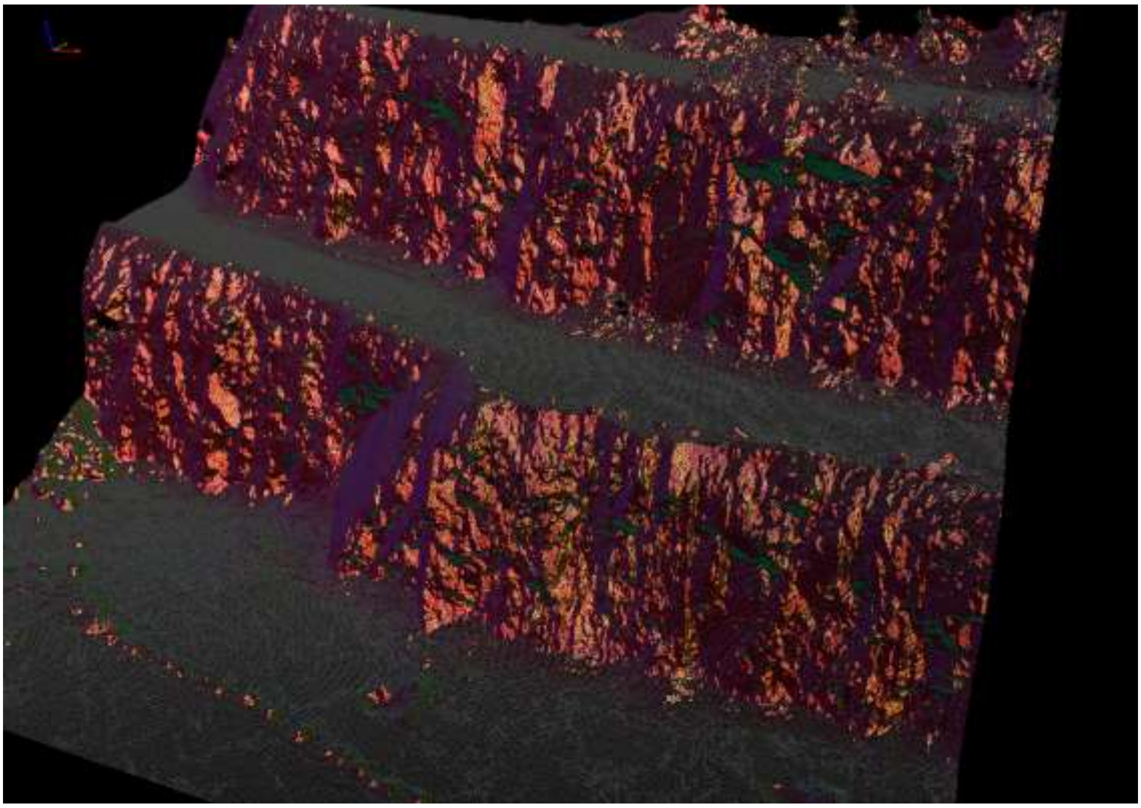

Figure 51: Highlighted dataset 'orange'; 163/55, tolerance 20°

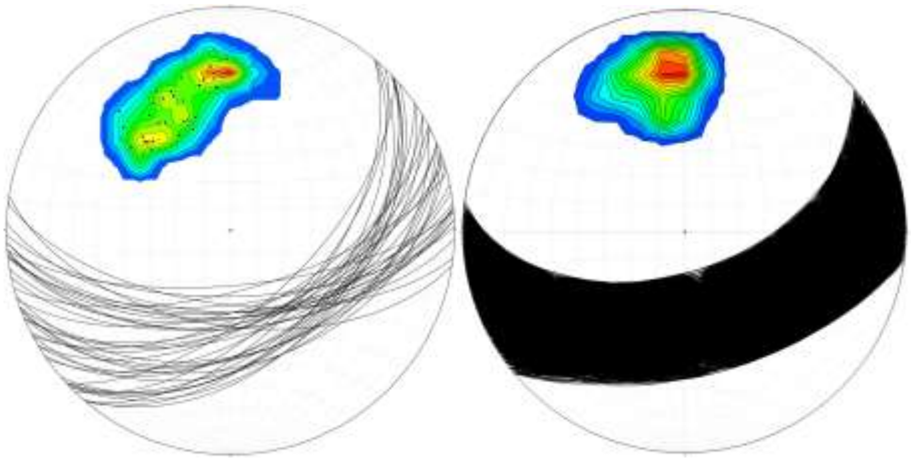

Figure 52: Stereo plots 'orange', left: field data, right: data from model

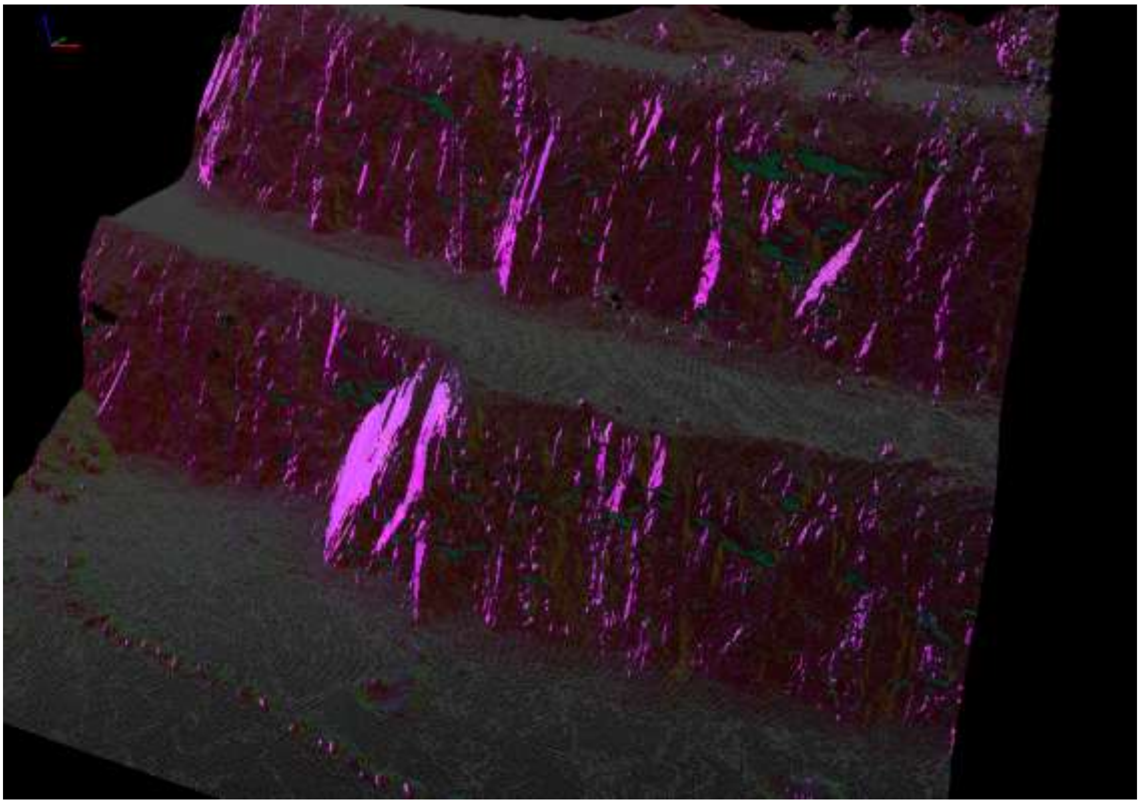

Figure 53: Highlighted dataset 'purple'; 250/65, tolerance 20°

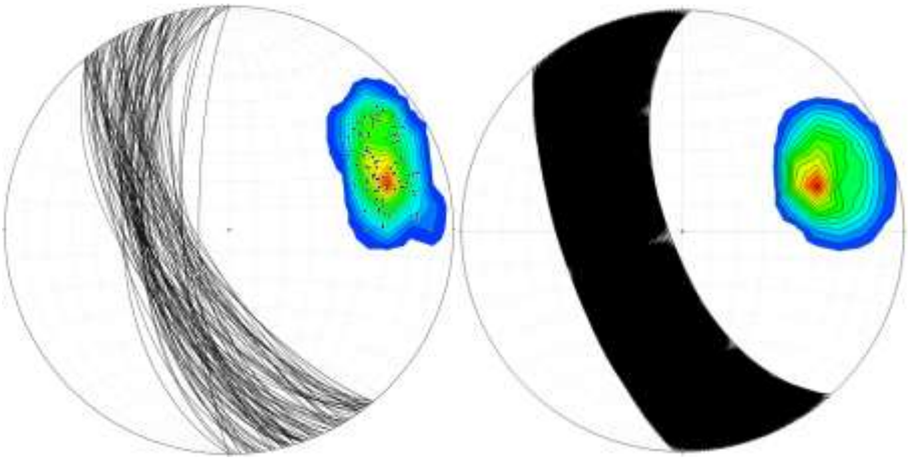

Figure 54: Stereo plots 'purple', left: field data, right: data from model

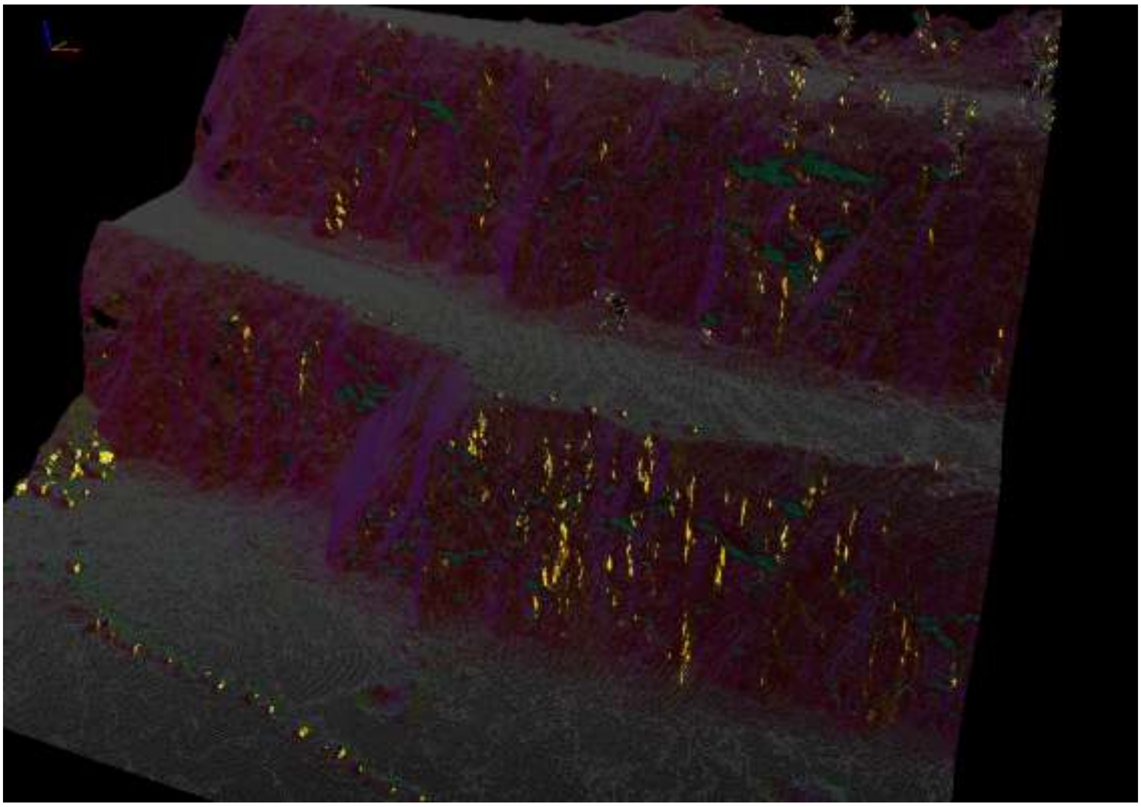

Figure 55: Highlighted dataset 'yellow'; 120/70, tolerance 20°

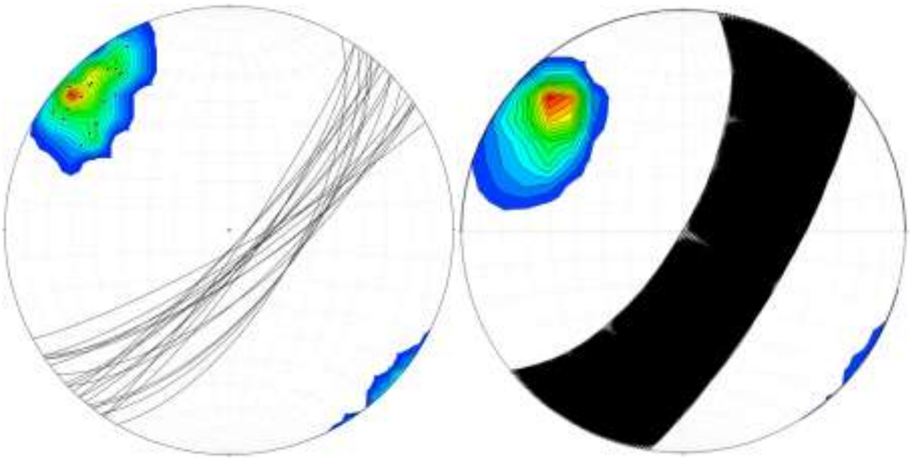

Figure 56: Stereo plots ‘yellow’, left: field data, right: data from model

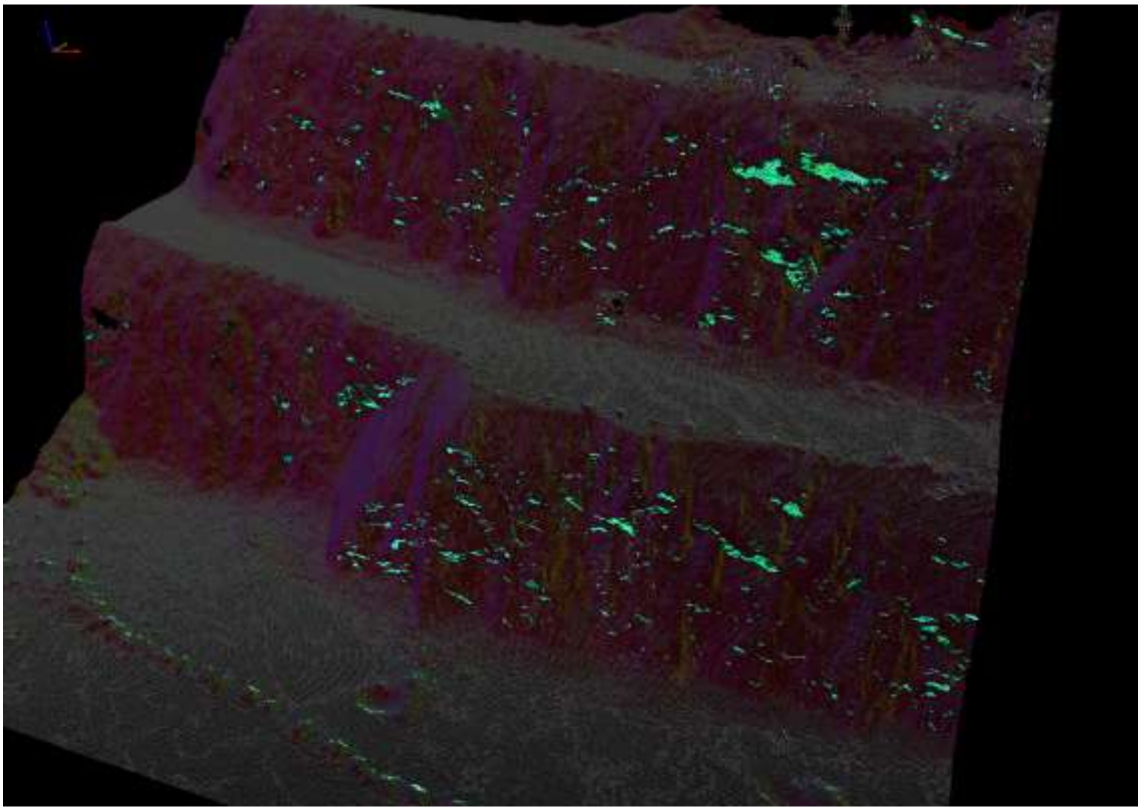

Figure 57: Highlighted dataset ‘green’; 320/60, tolerance 25°

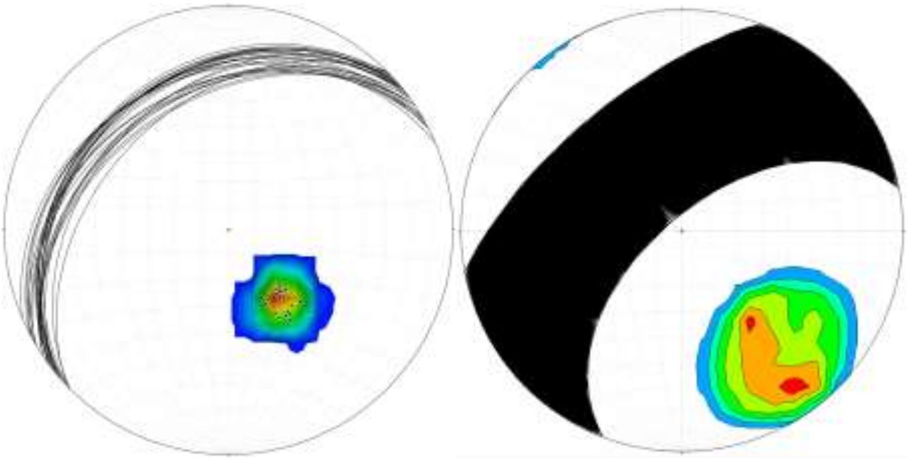

Figure 58: Stereo plots ‘green’, left: field data, right: data from model

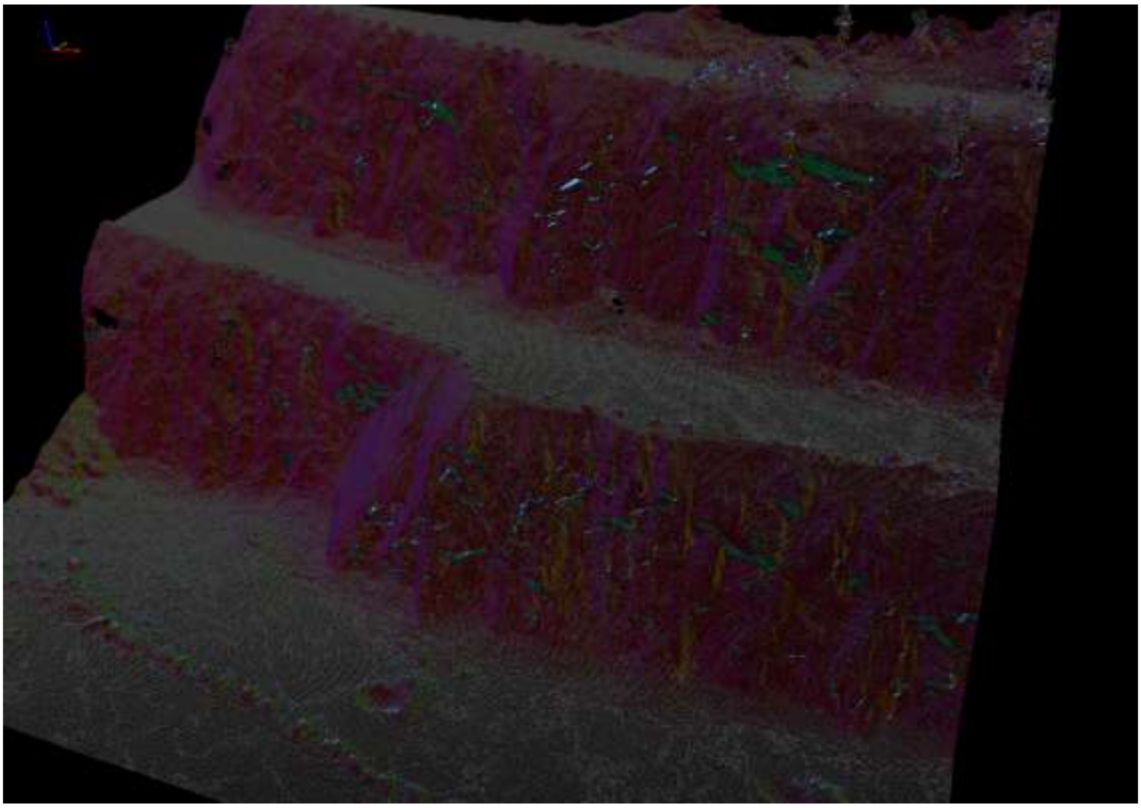

Figure 59: Highlighted dataset 'cyan'; 015/60, tolerance 25°

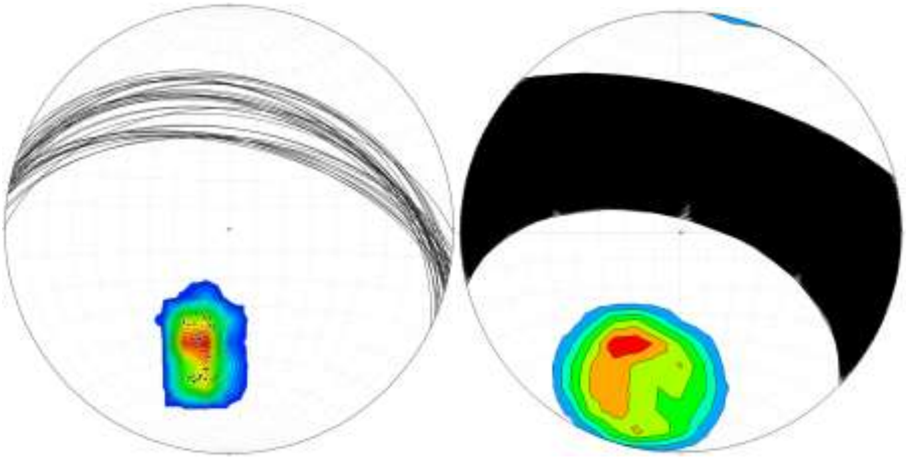

Figure 60: Stereo plots 'cyan', left: field data, right: data from model

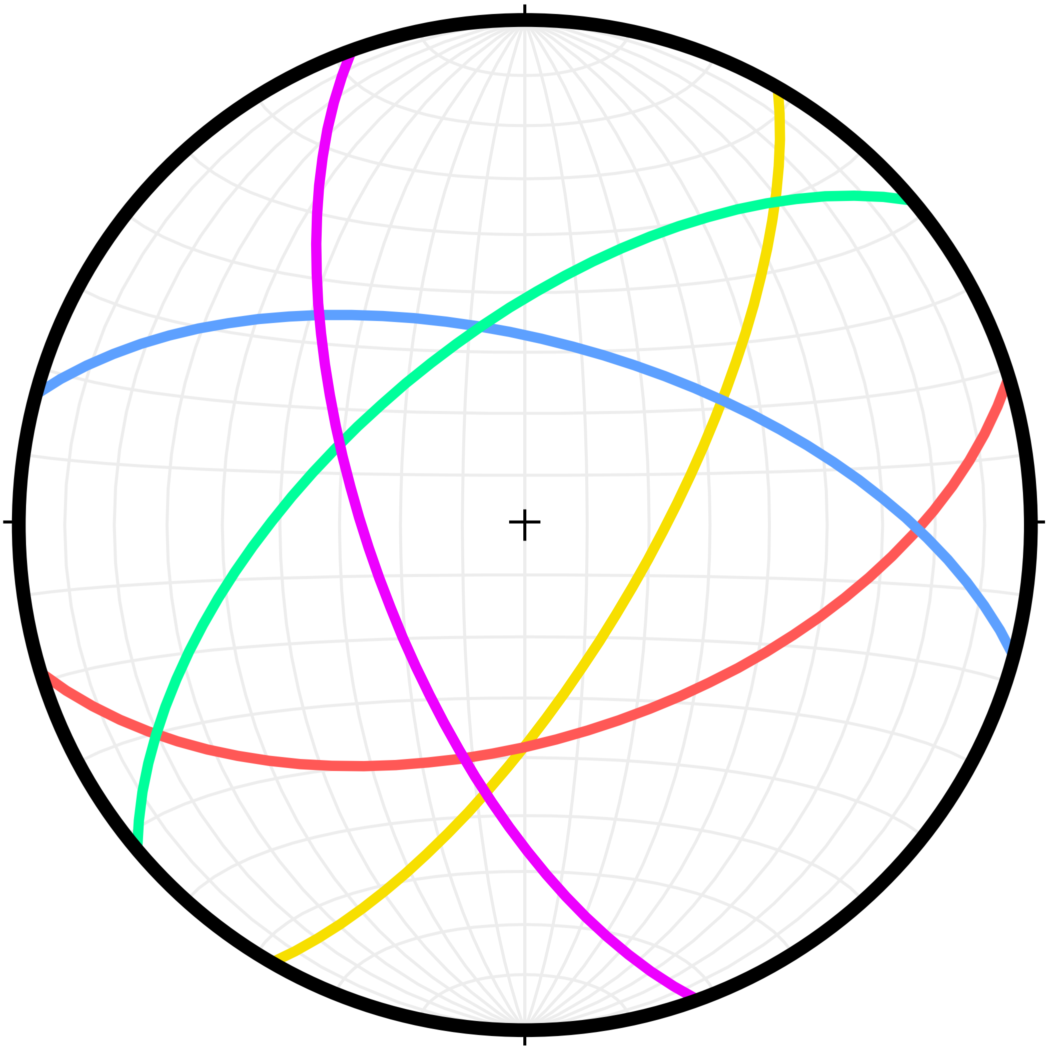

Figure 61: Stereoplot, mean values for joints colors as above
(orange 163/55, purple 250/65, yellow 120/70, green 320/60, cyan 015/60)

The hand-measured plots and the plots derived from the model show good accordance. Only minor derivations can be detected, mainly at the overhanging parts of the outcrop e.g. sets green and cyan.

The properties of the division surfaces showed different features. They range from biotite covered slickensides (with later crystal growth on them) to fresh, only though blasting opened cracks, which followed the joints. Those differences were not visible in Coltop3D.

6.2.2.2 Meshlab / Matlab approach

The results of the MATLAB/ Meshlab evaluation, found in the appendix in Table 3, can be compared to the manual measurements (Table 2). The data is plotted in Schmidt's Nets as described above (see Figure 62 - Figure 66); great circles and their respective poles with an underlying contour plot are all projected in the lower hemisphere.

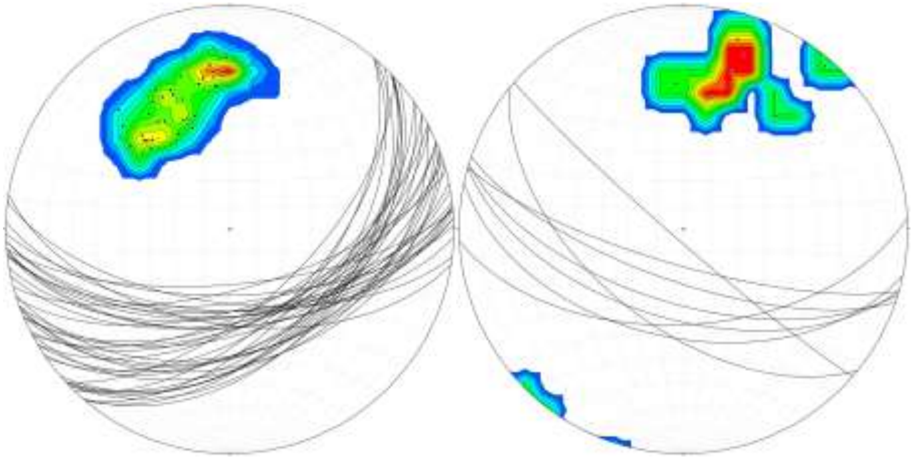

Figure 62: Stereo plots 'orange', left: field data, right: data extracted from Meshlab

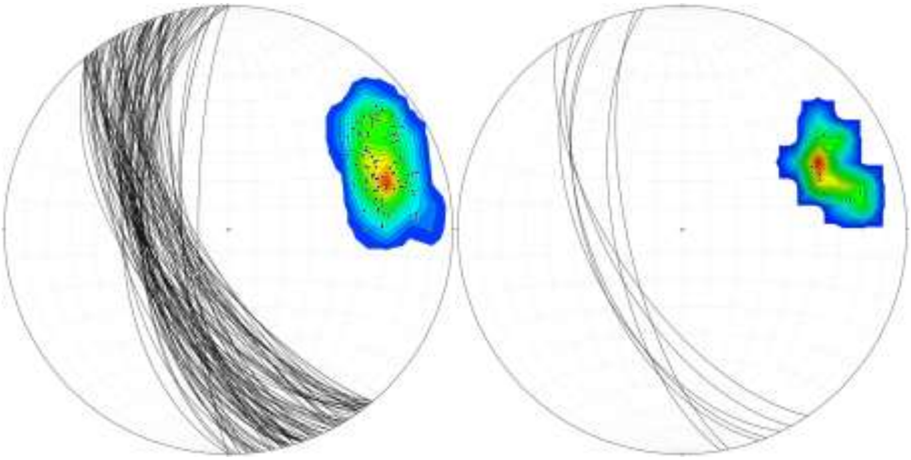

Figure 63: Stereo plots 'purple', left: field data, right: data extracted from Meshlab

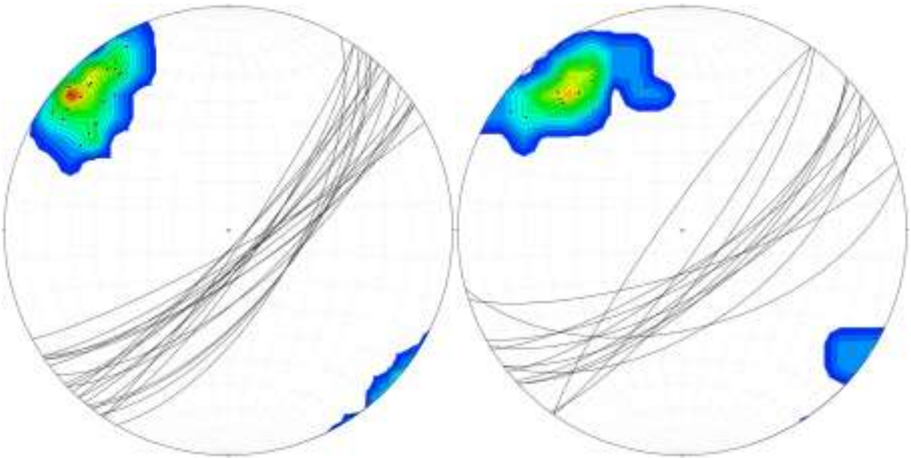

Figure 64: Stereo plots 'yellow', left: field data, right: data extracted from Meshlab

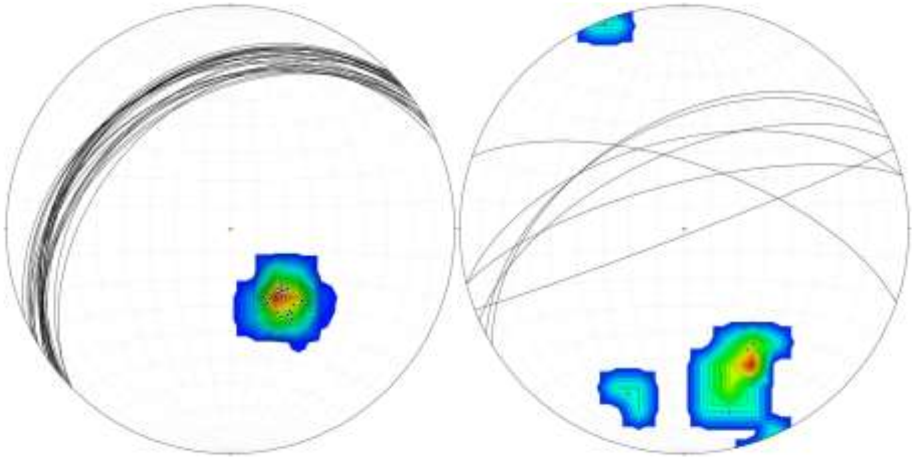

Figure 65: Stereo plots ‘green’, left: field data, right: data extracted from Meshlab

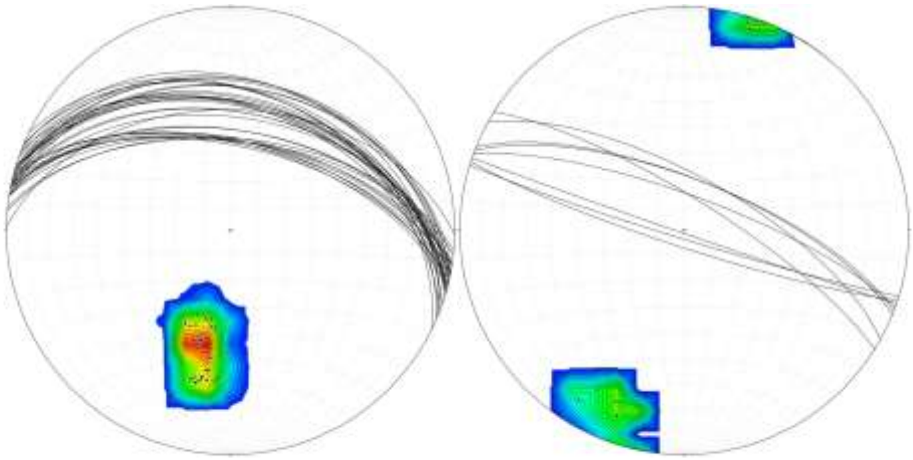

Figure 66: Stereo plots ‘cyan’, left: field data, right: data extracted from Meshlab

The hand-measured data and the data extracted from Meshlab show overlap with only minor error, the difference is mostly caused by complete outliers. For the well-developed bigger planes the data fits the manual measurements better.

7 Evaluation

7.1.1 Equipment

The first workstation (HP xw6600 Xeon E5405-2 GHz / 32 GB RAM / NVidia quadro fx4600) used to process the data unfortunately lacked the processing power to make use of the full capabilities of the software as well as handle the large data quantities produced during the project. For a project of this size a decent up-to-date system should be used; nevertheless, it was possible to handle the raw data and the marking of the GCPs with the low-end workstation. The final processing was then done at the processing workstation of the Ludwig-Boltzmann Institute (LBI ArchPro Workstation Xeon™ E5 2690 2.9GHz / 128 GB RAM / NVIDIA GeForce GTX 580).

The employed FrSky RC system matched the project requirements quite well in range and performance. The employed video-downlink system gives the operator enhanced situation awareness. This helps to accommodate gusts and other turbulent airflow. The audible feedback from the RC system helped to ensure a safe flight without requiring too much attention to the technical data, as it is read back to the operator if evasive or correcting measures are necessary.

7.1.2 Type of UAV

The fixed-wing type of UAV promised fast coverage of a large area. The results showed that it is possible to use this type of UAV and get results of sufficient quality. The mapping range matched the RF-power of the used equipment quite well. A bigger problem were the quite tight landing areas which made it impossible to use the implemented auto landing routines of the ArduPilotMega. The airframe showed good loading capabilities, only having some minor tip stall tendencies as a result of damage sustained in some high-speed landings. To facilitate handling and enhance flight performance a considerably higher speed than minimum stall speed was used. Unfortunately however, these higher speeds in turn lead to problems with the camera. The relatively slow shutter speed caused by a periodic overflow of the buffer in the camera made it difficult to adjust the number of images taken to the wider distances covered in the same time. Here, potential lies in adjusting either the camera settings, tweaking the ratio of height to focal length or choosing a different airframe like a Skywalker2014.

The additional use of the tricopter was a big enhancement for the survey of the benches on one side of the quarry. Its light weight and portability provide the possibility of approaches in short time and detailed survey of potentially dangerous areas. Unfortunately, the flight times only range between 6 and 8 minutes depending on required height, height over sea level, and wind load on the UAV.

7.1.3 GCPs

The resulting GNSS accuracies and precisions are acceptable for being in a high relief area. The best example is GCP #209 (for details see Table 6). At its position the model is sound and well-constructed. However, noticeable shadowing of the satellites caused by the steep relief leads to a considerable dilution of precision (DOP). This can be detrimental to the workflow as it dilutes the otherwise good uncorrected 3D model. The positional accuracy and precision of the GCPs can be enhanced by employing a total station, which is highly recommended. Except for some outliers the marking approach seemed to work fairly well and has the advantages of being reasonably cheap and fast. The only disadvantage of the markers also has a positive aspect: Weathering washes the markings away. This can be good or bad - depending on the aim of the project. On one hand, a self-destructing marker comes in handy as re-collecting takes up a lot of time. On the other hand, for a permanent marking (e.g. time-dissolved survey), the color does not remain visible long enough. For such an approach either a better-sticking spray or a durable object with a high visibility should be used, like a plastic dish pinned down with a nail. No objects exceeding a certain height should be used, e.g. cones, as they introduce further problems with the actual marking accuracy. The provided 2D codes from Agisoft could be handy but in this project they could not be used due to the fact that they were not recognized by the software. Reason was the too low resolution relative to the size of the printed posters. Also the partial overexposure of the white paper was hindering in the process.

Further tests with a total station and the respective working speed should be evaluated. The coded targets can be revisited, too. It should allow for faster marking of the GCPs , resulting in an overall faster availability of the processed data.

7.2 General issues

Flight height is one of the key variables while flying with small UAV. Not only the resulting resolution and overlap differ with different heights but it is also a crucial factor for flying in high relief areas. The resolution differs enormously from lower parts of the quarry to the higher ones. At the same time the operator has to have an eye for the safety of the UAV while increasing the ‘resolution’. As a fixed-wing UAV needs speed and time to climb, an adaptive flight mission is not always possible. The use of a multirotor type UAV would provide advantages in this regard. In this project the evaluation of the use of a fixed-wing type UAV for a quarry showed certain negative aspects. The flexibility needed for ultra-high resolution is only found in a multirotor platform. As for normal high-resolution flight a fixed-wing UAV can be employed without hesitation.

7.3 Resolution

The achieved resolution differs from area to area as described above. If the higher processing routines were used the resolution was not too different from the original photo quality. The loss of resolution on the other hand is only minor and is not hindering if the correct settings are used. The same is true for the DSM resolution.

Naturally, as the photos were taken facing more or less vertically into the nadir, photos sometimes lack information on the benches' side walls. This geometry results in problems with overhanging rocks, because during processing they are extrapolated further down. This has only minor influence on the overall cubature as there is only a minor change compared to the overall mass of the area, but it is sometimes hindering the assessment of joints and faults. The horizontal faced tricopters' camera can be, and was, an addition to the nadir-facing pictures taken by the fixed-wing UAV, allowing for an enhancement of the model. No major problems were encountered while mixing two different camera types (S110 and IXUS 75)

7.4 Software and data output

7.4.1 VSfM and CMVS

The VSfM (Visual Structure from Motion) and CMVS (Clustering Views for Multi-view Stereo) approach showed very good results. The data can compete with publicly available aerial data, like those from well-known internet-search-platforms, most of the time even better. This showed that even with minimal investment one can produce aerial data of good quality. Due to the software being freely available, certain allowances have to be made in terms of usability, mainly regarding the placement of the GCPs, which is not as convenient as with commercially available software. Nevertheless, the package gives the user a good start in the UAV topic.

7.4.2 Agisoft Photoscan

The package of Agisoft is one of the key elements in this work. It produced the required data in needed quality. The results and handling pay back the initial investment. While having this in mind, one should not underestimate the calculating power (high end workstation with a multicore CPU, RAM ≥ 128 GB, multiple GPU setup; for suggested setups see Agisoft homepage, Agisoft Photoscan (2013)) required for larger data sets, such as the ones in this project. The quality, not only the resolution, of the end product, is a direct result of the quality and quantity of the input and processing time. With low quality pictures and short time no good results can be achieved, but with good quality photos, overlap, ground control and an enormous amount of processing power, photorealistic models are possible as proven in this work.

7.4.3 MATLAB

MATLAB uses JAVA to display the results, which unfortunately causes some issues with turning and tilting the model. The execution of commands issued by the user is often delayed, resulting in overshooting commands, leading to unnecessary protraction of the workflow. Thus this particular approach is not recommended by this study, despite the fact that the MATLAB approach has the convenience of having direct access to a plotting function for the structural data.

7.4.4 Meshlab

Although the loaded *.ply is not geo-referenced, the data in the Photoscan project is. The relative orientation remains the same; thus it is possible to calculate the dip/dip-direction without the hassle of converting degrees to UTM to a relative hundred meter scale for better handling of the data.

As several different softwares are used to handle the data and different import and export steps are necessary (see workflow diagram, Figure 33), the presented approach is not very user-friendly and prone to errors. The data is produced by selection of the individual 3-point-sets by the user and thus heavily biased. At least two sources of error are based in this part of the approach, the user may ‘select’ the face, and the respective extension of it, which may not be accurate and/or the user may accidentally place points while navigating. As this approach is rather time consuming, the resulting dataset is relatively small, rendering the statistical value almost nonexistent and giving unproportional significance to outliers and random error.

However, this approach still leads to a 3D view, allowing the user a first estimation of the orientation of remotely sensed data. This reduces the danger of fatal rock fall to the geologist. Inaccessible areas or areas only reachable with high effort become easily available for measurements.

7.4.5 ArcGIS

As this technique is a 2.5-dimensional approach, it needs data on an exposed slope. Data could be gained but the effort and time needed to get reliable output are very high with this setting. This is not a problem of the approach itself but of the setting. The approach was already proven to work perfectly (Asmar et al., 2014). The quarry has steep benches, only few shallow slopes, and well exposed shoulders. This results in low visibility of joints and cracks. ArcGIS supports only nadir facing evaluation, in contrast to the other approaches described in this work. So this approach was put aside for another future dataset. Tests on artificial structure models were promising.

7.4.6 Coltop3D

As the version used is only a demo version, some features were reduced which precluded the full use and thus evaluation of the software capabilities. Nevertheless, it allowed a very efficient look at large datasets. Even the bigger datasets could be processed in a fairly short time e.g. 16 million points in 40 minutes on a single 2.5 GHz mobile i5 processor core. Note, the software seems to use only one core and therefore the maximal processing speed is only gained by high clock rates. The data mined out of the indexed point cloud is very well established in means of statistic repetitions. The vertices´ orientation is calculated automatically and thus unbiased compared to the Meshlab approach were the human input is quite high. On the accuracy side, the contour plots showed good results, matching the manual measurements within error. This is understandable as most of the well-established faces are in the middle of the quarry faces and so most of them are not directly accessible. So there will always be a gap (in data and in reach) between the sets. The outcrop on the other hand shows quite large change on the joints in short distances. Having this in mind having a larger data set and thus better statistics becomes more important than the established, well-reputed manual measurements.

The visible differences in the features of the division surfaces cannot be evaluated with Coltp3D. The software is not capable of this as the information is not in the dataset. This procedure, the identification of the division surfaces' features, is a field-based detection.

The only encountered problem are the small overhanging parts, as they seemed to lead to misinterpretations in the model (see Figure 58 and Figure 60). As the outcrop is fairly well 'cleaned' by the operating company, the number of overhanging parts suitable for testing this in detail is small. A bigger tolerance in the tool ('Direction and dip with tolerance') helps to find the correct mean orientation of the joints' set. The obtained orientation then fits the measured values quite well.

As this approach seems the most promising, it can be considered a good addition to the workflow, producing fast, reliable results. However, some drawbacks are present in the form of randomly occurring bugs, e.g. the random crashes.

8 Conclusions and outlook

Overall, the project was a success; data was collected in the needed degree of detail using low-cost equipment. It was possible to evaluate the data as planned. However, it proved inevitable to use commercial software for serious data processing. All in all, with some (suggested) enhancements, this workflow can definitely enhance the geological field work. Especially if up-to-date aerial coverage is called for, which can be made readily available with the help of the techniques described in this work, the presented workflow can make a difference. The evaluation of the structural data is not available at moment's notice. Handheld supported documentation (with Rocklogger) in the field is showing faster results. This is, however, only true if the outcrop is easily accessible and small. If not, the described workflow is definitively easier, considerably faster and much safer for the geologist. As the outcrop size increases, the return on invest with the described technique grows exponentially for the structural information.

Further testing of other software and their integration into the workflow is necessary, for example JMX analyst from 3C, Graz or SplitFX from split engineering LCC.

Smaller tasks like measuring volumina and cubatures can easily be done with Photoscan.

8.1 Outlook – technical issues

The applied techniques showed great capabilities. Enhancements can be made at several points, e.g. the airframe choice. Upgrading to a flying-wing with a more effective impellent would be a great step forward. Here a 4-cell setup and a large wingspan appear promising (cf. Rankin, 2013). The FC can be upgraded to an up-to-date 32bit processor as shown by the pixhawk project (Meier et al., 2012). On the camera-sensor side enhancements are always possible. With every generation of new CCD or CMOS chips on the marked the achievable resolution changes. However, it has to be taken into account that the quality does not only increase with better sensors. Also the build quality and the rugged design of the lens and the casing play a major role in achieving better results. Here, careful evaluation and experimentation is needed before decisions are made. The Ricoh GXR line for example was suggested by Ch. Briese, TU Vienna (personal communication) not for its high-end behavior, but for its excellent stability during flight and change. The camera seems closest to a measure camera in its compact class. With gained room and payload capabilities a step up to mirror-less cameras as the Sony NEX series can be considered. One of the main problems remains that even the best equipment still needs to be handled.

8.2 Outlook concerning used software

As doing measurements by hand within the software is very time-consuming and the advances in computer vision are steadily progressing, the user may as well use machine vision to evaluate large datasets. Some groups showed promising results: A workflow for a semiautomatic detection of joints has been proposed by Vasuki et al. (2014). Slob (2008) showed an approach for laser scanning and subsequent data evaluation. Other workflows, like the one presented in this work, are described for division surface evaluation of terrestrial laser scanning data or software. Here commercially available software can be used, e.g.Coltop3D or SPLIT FX. As these are not freely available software packages, their use does not comply with the low-cash-flow approach. On the other hand, the workflow described here shows how dramatically the work speed and data output are increased by use of these software packages. Here the same principle as with Photoscan applies. It is possible to stay on the lower end of the cost spectrum, however, the cost-value ratio of a manageable investment leading to a greatly enhanced output has to be considered.

Problems were encountered at the distinction between the division surfaces' properties, as the software does not provide a feasible way to distinguish for example a fresh slickenside from a rough brittle movement. But as the aim of this work is to highlight the possible uses of the evaluation of photogrammetric data produced by an UAV, this still can be seen as a success. If the distinction is necessary, a random examination of the separated sets is important; the collection of the division surfaces' properties can be accomplished in a streamlined, concurrent process.

This opens a door for further work to develop a way to evaluate a textured model by human perception. This proposition, a clean workflow on a workstation would be a safe, nonthreatening approach for a potential hazardous environment.

8.2.1 Possible enhancements

For the low-cost approach an approach similar to the one suggested by Slob (2008) can be employed, as no considerable difference exists between a pointcloud from photogrammetry and a pointcloud from a terrestrial laser scanner. The higher-cost approach would be acquiring the license for one of the laser scanning softwares described above. As these approaches can handle large datasets, they seem to be the right tool for an overview-assessment for large outcrops, and locating areas for further in-depth investigation in critical environments. The lost 'control' of the hand measurement can be seen as a loss of quality. But measurements by hand also have a big flaw, as they are time and energy consuming and only easily done from ground level to about 2 m height (e.g. maximal arm length of the geologist). So, even if they are done with a smartphone with Rocklogger, they lack the statistical reliability because of their comparably low number of repetitions. Clearly, this is mitigated to a certain degree with the use of digital devices, as their measurements are taken within considerably shorter time than with a compass, resulting in higher repetitions compared to a fully manual measurement. But still these devices are used by a human and this inevitably results in a 'comfort zone measurement' in a height of 1 m – 1.8 m often neglecting other values at different heights for speed, comfort or security reasons. The bottom line is, that every human-base measurement is heavily biased (see Chapter Software and data output).

The security aspect is never to be underestimated. If it is necessary to employ a two or a three man group just to let one geologist down a rope for assessment of a wall, the costs of the operation increase quickly. Even if the imminent danger of falling is dealt with, the danger of rock fall still remains. Here the potential loss of life puts a permanent danger to the existence of the operation or company like the hanging sword of Damocles threatening to fall in the form of a fatal accident leading to an official shutdown.

8.3 Outlook - financial

Most of the software used in this work is expensive, although it was planned to keep investment to a minimum. The package by Agisoft can be considered to be worth the money, despite or even because of its black box behavior. It does not overwhelm the user in the beginning; however, an advanced user might find the options a bit too rough. Nevertheless, it seems to be the industry-leading package, producing state of the art results. The competitor Pix4D was not available for testing due to lack of an evaluation license. For the automatic assessment of the structural data, further work will show the necessity of commercial software like Coltop3D or SplitFX. The MATLAB approach can be converted to another scripting language as shown by Asmar et al. (2014).

Overall, the investment for a workgroup in need of such product, like DSMs and/or orthophotos can easily produce these products themselves. Having a person responsible for the deployment, a lot of money can be saved with the additional benefits discussed in the introduction, like having safer working conditions in hazardous environments for the surveying geologist or not handing out data to subcontractors. The initial investment may be big and should never be considered on a too-tight budget, but the investment shows relatively fast. If the budget is too small, compromises have to be accepted and can cause failure, total loss of machinery and potential damage being inflicted to anything or anyone in the vicinity. Also the ready to run (RTR) offered packages should be judged carefully as they bear the usual danger in the form of lack of understanding of the underlying processes. While they offer fast results, a deeper understanding of the related aeronautical problems can, most of the time, only be mitigated by experience and better consolidated knowledge of the problems which can arise. This is a crucial point both for safety of the machinery used, and the operators´ and by-standers´ safety.

8.4 Outlook - scientific

The approach used in this study showed that it was never easier to produce scientifically assessable, high quality 3D-data. Further it was shown that UAV-supported structural mapping is possible and, with some experience, a huge enhancement.

As the method was mainly tested in a relatively easily manageable, controlled environment so far, the next step would be to evaluate an area with more difficult aeronautical demands. An interesting challenge for such a follow-up study would be evaluating the risk of rock-fall in a region with retreating permafrost or mapping a recent landslide. These fields, as already suggested above, would likely profit hugely from the opportunities provided by the availability of low-cost aerial 3D monitoring.

Possible geological applications have been discussed already in the Introduction (Chapter 1)

The application could be used in dangerous cases of a fresh rock fall or landslide like in Lenzer (2013). The amount of rock remaining in the freshly exposed unstable area and the potential of another failure can be evaluated. In this example the geologist was roped down form a helicopter trying to avoid the hazardous area. A UAV could easily document the situation, not only in a safer but in a much more economical way.

Further possible applications for this proposed workflow are documentation of roadcuts, new railroads and other fresh blasted areas. Assessment of the division surfaces can help for the estimation of required bolting and cubature of reinforced concrete to ensure a safe way. The extracted data can be directly included into the calculation of failing slide-wedges. It not only produces the structural data but also provides a high resolution 3D model; which serves as a convenient base for a construction drawing of the protective constructions.

With this approach the 3D modelling for research of hydrocarbons, which has already been mentioned in the introduction (CIPR Virtual Outcrop Geology Group, 2014a), can be achieved as well. A fixed wing UAV could provide the necessary large-scale model for cubature estimation. A smaller multi-rotor could supply the details, necessary to estimate the influence of smaller structures which serve as the main migration pathways of the hydrocarbons as well as the determination of possible seals and traps. This approach would be very similar to S. J. Buckley et al. (2008). This approach can be upgraded with a possible hyperspectral scanner like proposed in (CIPR Virtual Outcrop Geology Group, 2014c)

Finally it just remains to be concluded that the idea of using self-produced orthophotos for convenient mapping in the field, which originally lead to the conduction of this project, could be proven to work remarkably well.

8.5 Final thoughts

Small scale UAVs can produce good and usable data for geological applications. It enables scientists, engineers, and authorities to base their decisions on up to date remote sensing data and plan accordingly. The time required to learn the basics of the technique is rather short due to the enormous technological advances in the last five to ten years.

The geological uses are definitively given, although as a niche they need some adjustments in the post-processing to reach their full potential. At this time, the used approach already helps the user to be one step ahead and create great results.

9 Acknowledgements

First of all I would like to thank Erich Draganits and Bernhard Grasemann for the possibility to make this project happen as well as for the support and help.

A distinguished help with this project were Niki for all detailed support within the quarry, Florian and his family for the possibility to access the quarry and the massive help during the rescue mission and the workshop crew for carrying out the rescue mission.

I’d like to thank Geert for all the technical insights, administrative help, processing-time at his workstation and so much more.

For reviewing the manuscript, Anne and Matthias took considerably part, thus enhancing it by magnitudes.

The following persons helped a lot with this project:

- Andrea, Anne, Christian, Dominic, Mathias, Matthias for all the critical input
- Chloe for supplying the great ArcGIS script, and for the additional personal training
- Ben for his help with the MATLAB approach, it was enormous
- Friedhelm for fast 24/7 technical support
- The DIY Drones community for providing such great products

I’d like to express my gratitude for all the help and support from my friends and family.

Finally I’d like to thank Kathi for all the encouragement, motivation and the priceless help with launching the UAV. The next tree will always be there for you.

10 Table of figures

11 Table of tables

12 Abbreviations

ACC	accelerometer, measures acceleration in XYZ direction
A	ampere
AGL	above ground level
ALThold	altitude hold, holding the altitude of the copter by managing the throttle automatically
APM	flight control, based on Atmel microprocessor; ArduPilotMega
BARO	barometer, measures pressure of air
CHDK	canon hack development kit (custom firmware)
CMOS	complementary metal-oxide-semiconductor
CMVS	Clustering Views for Multi-view Stereo
CUDA	Compute Unified Device Architecture, a GPU framework from NVIDIA
DoF	degrees of freedom
DSM	digital surface model
ESC	electronic speed controller
EXIF	Exchangeable Image File Format, metadata in picture files
FC	flight control
FPV	First person view
FW	firmware
GCP	ground control point
GNSS	global navigation satellite system
GYRO	gyroscope, measures the orientation of the sensors XYZ coordinates
DOP	dilution of precision
HF	high frequency
IS	image stabilizer
kv	revolutions per applied volts
LiPo	lithium polymer battery
MAG	magnetometer, measures the magnetic field in XYZ directions
MG	metal gear
NDVI	normalized differenced vegetation index
OpenCL	Open Computing Language, an open processing framework from Khronos Group
OSD	on screen display (video overlay)

PCB	printedcircuit board, microchips are placed on it
ply	file type, consisting of point clouds or TINs
PP	point picking
propwash	also propeller wash-down, rapid airflow below a spinning propeller
RC	remote controlled
RTR	ready to run
Rx	receiver
SIFT	scale-invariant feature transform
SMD	surface mount device, usually very small
TIN	triangulated network, a surface based on a pointcloud consisting out of triangles
TVL	TV -lines (resolution)
Tx	transmitter
UAV	unmanned aerial vehicle
UBEC	voltage regulator (battery eliminator circuit)
UHF	ultra high frequency , spectrum between 300 MHz and 3 GHz but mainly used up to 1GHz
UTM	Universal Transverse Mercator
V	volt
VSFM	visual structure from motion
VTOL	vertical take-off and landing
VTx	video transmitter
W	watt
WP	waypoints

13 Appendix

13.1 Tables

Table 1: Accuracy statements from Trimble Pathfinder Office

	measurements	corrected	ACC	0-15cm	15-30cm	30-50cm	0.5-1m	1-2m	2-5m	>5m
Batch 1	5449	5162		67.70%	8.40%	11.50%	11.20%	1.20%	0.00%	0.00%
Batch 2	7536	7270		48.50%	12.50%	17.90%	15.90%	1.30%	0.20%	3.70%

Table 2: manual measurements with Rocklogger

orange		**purple**		**yellow**		**green**		**cyan**	
DIP direction	DIP	DIP direction	DIP	DIP direction	DIP	DIP direction	DIP	DIP direction	DIP
84	54	50	15	300	25	236	41	181	45
84	58	50	26	304	12	240	35	186	33
62	60	50	22	304	6	236	40	194	33
84	60	50	15	305	25	234	37	195	32
85	54	51	29	307	11	242	35	191	33
72	61	51	36	308	25	230	36	192	32
80	58	51	20	309	25	234	38	192	44
67	57	52	33	310	10	226	42	196	46
59	56	52	14	312	12	236	38	189	33
63	56	52	17	312	5	225	37	194	33
75	68	52	20	314	5	239	29	191	34
40	54	53	19	316	21	243	30	193	31
44	56	53	28	316	11	241	29	201	46
56	48	53	21	317	11	247	30	196	48
70	40	54	22	320	22	229	30	195	47
47	45	54	28	323	11	231	32	193	48
40	48	54	29	325	16	233	31	199	47
73	44	54	18	325	13	233	29	206	52
59	47	54	18	326	16	226	30	200	53
78	56	55	25	326	10	231	28	189	42
67	55	55	12	331	7	229	28	196	50
67	44	56	26			228	30	197	49
87	60	57	35			230	29	195	48
99	55	58	14			232	30	202	57
92	60	58	37			229	30	196	57
89	66	59	29			227	27	191	54

orange		purple		yellow		green		cyan	
DIP direction	DIP	DIP direction	DIP	DIP direction	DIP	DIP direction	DIP	DIP direction	DIP
97	63	59	29			242	35	192	57
83	63	59	11			240	37	194	56
87	58	60	30					203	52
47	62	60	15					203	52
55	53	60	16					189	54
70	52	61	32					189	37
85	70	61	14					185	34
49	44	61	29					190	37
46	42	61	14					191	44
41	43	62	16						
46	46	62	18						
47	48	63	36						
62	40	63	29						
69	44	63	29						
		65	29						
		65	28						
		65	33						
		66	32						
		67	29						
		67	29						
		67	18						
		68	21						
		68	17						
		69	31						
		69	32						
		69	24						
		70	35						
		70	40						
		70	32						
		71	24						
		71	35						
		71	30						
		71	35						
		71	28						
		71	23						
		71	31						
		73	13						
		73	17						
		73	15						

orange		purple		yellow		green		cyan	
DIP direction	DIP	DIP direction	DIP	DIP direction	DIP	DIP direction	DIP	DIP direction	DIP
		74	31						
		74	36						
		74	22						
		74	28						
		75	32						
		75	33						
		75	19						
		75	28						
		76	22						
		76	21						
		76	25						
		78	33						
		78	17						
		79	17						
		79	31						
		79	34						
		81	31						
		81	31						
		82	39						
		82	33						
		83	33						
		83	27						
		84	31						
		85	29						
		85	17						
		87	17						
		87	17						
		88	32						
		89	32						
		90	11						
		90	39						

Table 3: Measurements of DIP direction and DIP extracted with Meshlab

orange		purple		yellow		green		cyan	
DIP direction	DIP	DIP direction	DIP	DIP direction	DIP	DIP direction	DIP	DIP direction	DIP
166	64	249	55	142	76	18	60	7	58
199	71	248	56	141	76	29	70	332	51
177	55	250	55	138	72	32	78	329	50
192	50	260	65	162	75	21	71	346	57
197	63	258	70	165	54	20	77	336	62
219	55	241	62	125	82	199	89	346	73
196	77	244	54	149	67	198	84	19	66
221	86	236	65	143	66	197	87	159	88
196	57			148	77	22	71		
				126	75				
				151	72				
				137	67				
				305	83				
				143	56				
				137	69				

Table 4: Statistical statements from Photoscan processing

General statistics	
Number of images:	2080
Flying altitude:	95.3408 m
Ground resolution:	0.021604 m/pix
Coverage area:	1.14809 km²
Camera stations:	1955
Tie-points:	2104541
Projections:	4743817
Error:	0.520798 pix
DSM	
Resolution:	0.172832 m/pix
Point density:	33.4775 points per m²

Table 5: GCP's accuracy out of Trimble Pathfinder Office [m]

ID	STD. DEV	Verti	Horiz	Type of Correction	ID	STD. DEV	Verti	Horiz	Type of Correction
1	0.02287	0.02	0.01	CTFix	130	0.101647	1.15	1.06	CTFloat
2	0.024889	0.02	0.01	CTFix	131	0.083034	0.55	0.41	CTFloat
3	0.042643	0.02	0.02	CTFix	132	0.064233	0.53	0.43	CTFloat
4	0.054391	0.02	0.02	CTFix	133	0.053197	0.01	0.01	CTFix
5	0.074693	0.03	0.02	CTFix	134	0.060339	0.01	0.01	CTFix
6	0.040686	0.04	0.03	CTFix	135	0.056112	0.02	0.02	CTFix
7	0.053119	0.03	0.03	CTFix	136	0.040742	0.01	0.02	CTFix
8	0.056135	0.02	0.02	CTFix	137	0.04608	0.01	0.02	CTFix
9	0.046011	0.02	0.01	CTFix	138	0.044106	0.01	0.02	CTFix
10	0.044	0.02	0.01	CTFix	139	0.187808	0.02	0.02	CTFix
11	0.042402	0.01	0.01	CTFix	140	0.049802	0.03	0.03	CTFix
12	0.045319	0.01	0.01	CTFix	141	0.049067	0.02	0.02	CTFix
13	0.043075	0.01	0.01	CTFix	142	0.075824	0.02	0.02	CTFix
14	0.034047	0.02	0.01	CTFix	143	0.055025	0.02	0.02	CTFix
15	0.056561	0.01	0.01	CTFix	144	0.034459	0.02	0.02	CTFix
16	0.025732	0.14	0.06	CTFloat	145	0.049102	0.02	0.02	CTFix
17	0.050961	0.07	0.03	CTFix	146	0.045251	0.02	0.02	CTFix
18	0.043874	0.04	0.02	CTFix	147	0.047063	0.02	0.01	CTFix
19	0.032305	0.06	0.08	CTFix	148	0.037084	0.01	0.01	CTFix
20	0.070738	0.01	0.01	CTFix	149	0.059714	0.01	0.01	CTFix
21	0.089478	0.01	0.01	CTFix	150	0.150105	0.01	0.01	CTFix
22	0.035265	0.01	0.01	CTFix	151	0.084914	0.01	0.02	CTFix
23	0.043625	0.07	0.03	CTFix	152	0.07859	0.01	0.02	CTFix
24	0.051275	0.24	0.15	CTFloat	153	0.061477	0.02	0.02	CTFix
25	0.059507	0.46	0.38	CTFloat	154	0.060073	0.01	0.01	CTFix
26	0.059479	0.33	0.27	CTFloat	155	0.042502	0.04	0.03	CTFix
27	0.089559	0.4	0.32	CTFloat	156	0.053265	0.02	0.02	CTFix
28	0.059838	0.39	0.32	CTFloat	157	0.05951	0.12	0.12	CTFix
29	0.054502	0.57	0.5	CTFloat	158	0.056736	0.1	0.1	CTFloat
30	0.072684	0.53	0.34	CTFloat	159	0.036038	0.1	0.1	CTFloat
31	0.065596	0.64	0.44	CTFloat	160	0.004767	0.1	0.1	CTFloat
32	0.493299	3.16	1.46	CTFloat	161	0.064031	0.1	0.1	CTFloat
33	0.575298	1.51	0.79	RT-SBAS	162	0.066936	0.1	0.1	CTFloat
34	0.136554	1.63	0.82	CTFloat	163	0.050774	0.1	0.1	CTFloat
35	0.116411	1.31	0.71	RT-SBAS	164	0.041671	0.1	0.1	CTFloat
36	0.09023	6.75	2.41	RT-SBAS	165	0.060965	0.1	0.1	CTFloat
37	0.149551	6.4	2.28	RT-SBAS	166	0.058391	0.1	0.1	CTFloat
38	0.160837	2.45	1.63	RT-SBAS	167	0.062857	0.1	0.1	CTFloat
39	0.098215	0.88	0.56	CTFloat	168	0.030347	0.1	0.1	CTFloat

ID	STD. DEV	Verti	Horiz	Type of Correction	ID	STD. DEV	Verti	Horiz	Type of Correction
40	0.068424	0.86	0.55	CTFloat	169	0.053379	0.1	0.1	CTFloat
41	0.049652	0.51	0.38	CTFloat	170	0.079638	0.1	0.1	CTFloat
42	0.054466	0.47	0.36	CTFloat	171	0.056341	0.1	0.1	CTFloat
43	0.070538	0.48	0.36	CTFloat	172	0.078243	0.1	0.1	CTFloat
44	0.071409	0.53	0.53	CTFloat	173	0.063072	0.1	0.1	CTFloat
45	0.318603	0.38	0.44	CC	174	0.050968	0.1	0.1	CTFloat
46	0.095361	0.31	0.29	CTFloat	175	0.030994	0.1	0.1	CTFloat
47	0.07624	0.25	0.28	CTFloat	176	0.066416	0.1	0.1	CTFloat
48	0.091174	0.41	0.42	CTFloat	177	0.043844	0.1	0.1	CTFloat
49	0.061543	0.29	0.31	CTFloat	178	0.069493	0.1	0.1	CTFloat
50	0.102118	0.37	0.4	CTFloat	179	0.081737	0.1	0.1	CTFloat
51	0.2146	0.99	0.78	CTFloat	180	0.056523	0.1	0.1	CTFloat
52	0.145873	1.28	0.94	CTFloat	181	0.057249	0.1	0.1	CTFloat
53	0.059064	0.87	0.5	CTFloat	182	0.302529	5.58	3.27	RT-SBAS
54	0.075631	0.83	0.46	CTFloat	183	0.164298	5.59	3.2	RT-SBAS
55	0.089925	1.72	0.78	CTFloat	184	0.303911	5.57	3.14	RT-SBAS
56	0.12315	0.61	0.4	CTFloat	185	0.155109	0.89	0.68	CTFloat
57	0.109123	0.89	0.51	CTFloat	186	0.091289	0.61	0.52	CTFloat
58	0.083933	0.85	0.49	CTFloat	187	0.079297	0.31	0.33	CTFloat
59	0.07538	1.02	0.58	CTFloat	188	0.07252	0.32	0.32	CTFloat
60	0.071342	0.96	0.53	CTFloat	189	0.091912	0.1	0.1	CTFloat
61	0.329252	1.89	0.87	CTFloat	190	0.109744	0.1	0.1	CTFloat
62	0.14517	2.13	0.93	CTFloat	191	0.094989	0.1	0.1	CTFloat
63	0.120142	1.36	0.74	CTFloat	192	0.069168	0.1	0.1	CTFloat
64	0.415132	1.34	1.01	RT-SBAS	193	0.108135	0.11	0.11	CTFloat
65	0.112546	0.72	0.72	CTFloat	194	0.049576	0.12	0.13	CTFloat
66	0.138731	0.52	0.42	CTFloat	195	0.048973	0.1	0.1	CTFloat
67	0.100508	0.16	0.2	CTFloat	196	0.083087	0.1	0.1	CTFloat
68	0.048361	0.16	0.21	CTFloat	197	0.078786	0.1	0.1	CTFloat
69	0.069957	0.23	0.26	CTFloat	198	0.05863	0.1	0.1	CTFloat
70	0.080778	0.26	0.27	CTFloat	199	0.031546	0.26	0.19	CTFloat
71	0.160316	0.1	0.1	CTFloat	200	0.057979	0.1	0.1	CTFloat
72	0.04755	0.13	0.13	CTFloat	201	0.069779	0.12	0.11	CTFloat
73	0.675212	32.42	21.89	CC	202	0.08619	0.35	0.4	CTFloat
74	0.378636	30.2	20.28	CC	203	0.122921	0.78	0.57	CTFloat
75	0.09357	0.1	0.1	CTFloat	204	0.057235	0.23	0.14	CTFloat
76	1.250392	30.97	25.24	CC	205	0.051059	0.1	0.1	CTFloat
77	2.223112	36.45	29.81	CC	206	0.049601	0.25	0.13	CTFloat
78	1.860989	36.63	29.7	CC	207	0.186458	0.52	0.45	CTFloat
79	0.056225	0.1	0.1	RT-SBAS	208	0.101572	0.15	0.23	CTFloat

ID	STD. DEV	Verti	Horiz	Type of Correction	ID	STD. DEV	Verti	Horiz	Type of Correction
80	0.056123	0.37	0.51	RT-SBAS	209	0.051522	0.12	0.13	CTFloat
81	0.124056	0.35	0.5	CTFloat	210	0.106201	0.18	0.18	CTFloat
82	0.120627	0.26	0.39	CTFloat	211	0.059381	0.1	0.1	CTFloat
83	0.141559	0.23	0.73	CTFloat	212	0.050021	0.1	0.1	CTFloat
84	0.081962	0.1	0.1	CTFloat	213	0.068345	0.1	0.1	CTFloat
85	0.052852	0.1	0.1	CTFloat	214	0.090617	0.1	0.1	CTFloat
86	0.101221	0.1	0.11	CTFloat	215	0.092396	0.1	0.1	CTFloat
87	0.051185	0.1	0.1	CTFloat	216	0.122939	0.49	0.36	CTFloat
88	0.07334	0.1	0.1	CTFloat	217	0.067332	0.16	0.12	CTFloat
89	0.054559	0.1	0.1	CTFloat	218	0.095129	0.46	0.3	CTFloat
90	0.06415	0.1	0.1	CTFloat	219	0.065933	0.17	0.13	CTFloat
91	0.065422	0.1	0.1	CTFloat	220	0.249883	1.48	1	CTFloat
92	0.029166	0.1	0.1	CTFloat	221	0.07659	0.32	0.24	CTFloat
93	0.032657	0.1	0.1	CTFloat	222	0.064483	0.54	0.41	CTFloat
94	0.059128	0.15	0.12	CTFloat	223	0.117647	0.78	0.51	CTFloat
95	0.26847	0.13	0.11	CTFloat	224	0.136535	0.86	0.53	CTFloat
96	0.122325	0.12	0.1	CTFloat	225	0.169364	0.92	0.63	CTFloat
97	0.078628	0.16	0.16	CTFloat	226	0.124073	0.74	0.38	CTFloat
98	0.12672	0.19	0.18	CTFloat	227	0.076019	0.52	0.29	CTFloat
99	0.100822	0.23	0.24	CTFloat	228	0.067072	0.45	0.27	CTFloat
100	0.184617	0.3	0.27	CTFloat	229	0.081159	0.81	0.41	CTFloat
101	0.136846	0.42	0.26	CTFloat	230	0.102289	0.49	0.33	CTFloat
102	0.093126	0.49	0.34	CTFloat	231	0.144233	0.48	0.23	CTFloat
103	0.128124	0.51	0.42	CTFloat	232	0.102765	0.11	0.11	CTFloat
104	0.144915	0.34	0.33	CTFloat	233	0.044928	0.12	0.1	CTFloat
105	0.094356	0.32	0.27	CTFloat	234	0.070767	0.25	0.13	CTFloat
106	0.181602	0.28	0.24	CTFloat	235	0.048682	0.26	0.14	CTFloat
107	0.056773	0.26	0.2	CTFloat	236	0.046878	0.18	0.14	CTFloat
108	0.067386	0.24	0.22	CTFloat	237	0.080021	0.39	0.34	CTFloat
109	0.054101	0.21	0.28	CTFloat	238	0.076287	0.52	0.3	RT-SBAS
110	0.101687	0.14	0.14	CTFloat	239	0.049531	0.15	0.12	CTFloat
111	0.052135	0.1	0.1	CTFloat	240	0.052487	0.24	0.17	CTFloat
112	0.10454	0.1	0.1	CTFloat	241	0.046152	0.1	0.12	CTFloat
113	0.055176	0.1	0.1	CTFloat	242	0.044983	0.1	0.1	CTFloat
114	0.19357	0.1	0.1	CTFloat	243	0.057688	0.1	0.1	CTFloat
115	0.042947	0.1	0.1	CTFloat	244	0.050936	0.1	0.1	CTFloat
116	0.067178	0.1	0.1	CTFloat	245	0.046661	0.1	0.1	CTFloat
117	0.035805	0.1	0.1	CTFloat	246	0.103602	0.1	0.1	CTFloat
118	0.066404	0.1	0.1	CTFloat	247	0.04544	0.1	0.1	CTFloat
119	0.12922	0.1	0.1	CTFloat	248	0.058794	0.2	0.17	CTFloat

ID	STD. DEV	Verti	Horiz	Type of Correction	ID	STD. DEV	Verti	Horiz	Type of Correction
120	0.209666	0.1	0.1	CTFloat	249	0.093622	0.71	0.54	CTFloat
121	0.060264	0.1	0.1	CTFloat	250	0.105654	1.33	0.8	RT-SBAS
122	0.029592	0.1	0.1	CTFloat	251	0.127964	0.86	0.77	CTFloat
123	0.036091	0.1	0.1	CTFloat	252	0.092358	0.88	0.61	CTFloat
124	0.057105	0.12	0.1	CTFloat	253	0.105609	0.81	0.59	CTFloat
125	0.062166	0.1	0.1	CTFloat	254	0.389274	1.53	0.71	RT-SBAS
126	0.090626	1.18	0.74	CC	255	0.130114	1.1	0.75	CTFloat
					256	0.145409	1.36	0.92	CTFloat
					257	0.092498	1.06	0.75	CTFloat
					258	0.099587	0.86	0.68	RT-SBAS

Table 6: GCPs errors and projection statements out of Photoscan

GCP Number	Error (X)	Error(Y)	Error(Z)	Error (m)	Projections	Error(pixel)
1	-0.260407	0.078065	0.045023	0.27556	7	47.328562
2	-0.344171	-0.054802	0.0216	0.349175	11	38.001037
3	-0.503218	-0.34874	-0.186077	0.639901	13	22.183277
4	-0.514505	-0.158622	-0.006822	0.538444	13	7.850509
5	-0.356889	0.156908	0.229435	0.452361	12	24.178813
6	-0.183334	0.381421	0.645368	0.771747	9	39.605714
7	-0.079512	0.520804	1.089875	1.210531	8	3.308145
8	0.023396	0.764708	1.2677	1.480672	9	31.74803
9	0.067509	0.770629	1.554564	1.736403	9	7.532612
10	0.253104	0.792364	1.685108	1.879226	10	39.527744
11	0.202757	0.78616	1.972976	2.133493	7	1.538545
14	0.370693	0.179488	2.164975	2.203802	4	2.238788
15	0.300798	0.516577	2.382658	2.456499	2	0.054432
16	-1.283542	0.10415	1.381171	1.888375	1	0
17	0.417307	0.56752	2.448683	2.547994	2	0.95244
18	0.312154	0.617497	1.976227	2.093852	5	3.836313
19	0.49657	0.653861	1.936766	2.103611	11	3.649423
20	0.663548	0.775415	1.737354	2.014935	15	3.577886
21	0.620137	0.66825	1.609101	1.849414	15	5.185223
22	0.765861	0.508384	1.397156	1.672436	10	0.880452
23	0.761054	0.436596	1.216577	1.499959	14	0.994057
24	0.656964	0.177515	0.542582	0.87035	18	1.912394
25	0.974339	0.533722	0.241444	1.136878	15	1.315887
26	0.58997	0.662803	0.494607	1.015878	11	1.809342
27	0.772334	0.769452	1.042388	1.508353	5	1.83246
28	0.824788	0.740143	1.560016	1.913566	4	7.105061
29	0.499164	0.680582	1.601081	1.809922	2	0.07154
31	1.056114	0.707125	0.464469	1.353194	14	1.233219
32	0.604627	-0.425606	1.004736	1.247481	13	3.720926
33	0.468791	0.051628	0.369069	0.598868	8	2.051041
34	0.361375	-0.161329	-0.158867	0.426447	7	1.18116
35	0.983831	0.481011	-2.749465	2.959535	4	1.864648
36	-0.021079	-0.106709	-1.613013	1.616677	3	0.621993
37	0.172805	-0.243008	-1.478524	1.508293	5	1.263697
38	0.141109	-0.212813	-1.080357	1.110122	3	0.946592
39	0.499519	-0.283895	-1.989783	2.071075	11	1.119869
40	0.379067	-0.426088	-1.79256	1.881094	7	0.802902
41	0.44255	-0.531608	-1.727076	1.860444	6	0.70558
42	0.335436	-0.705422	-1.73061	1.898723	6	1.155981

GCP Number	Error (X)	Error(Y)	Error(Z)	Error (m)	Projections	Error(pixel)
43	0.226701	-0.744633	-1.474945	1.667734	11	1.023986
44	0.288289	-0.624324	-1.994733	2.109941	7	1.039716
45	-0.029365	-0.810134	-1.190587	1.440374	9	18.873178
46	0.043689	-0.788765	-1.416992	1.622321	6	4.530905
47	0.043071	-0.919006	-0.72724	1.172734	11	0.833213
48	0.109318	-0.925427	-0.573031	1.093951	18	3.469038
49	-0.051966	-0.636917	-0.938072	1.135052	12	3.325706
50	-0.099783	-0.541916	-0.856148	1.018145	12	4.559204
51	-0.070017	-0.622978	-0.225919	0.666366	12	3.569241
52	0.141292	-0.297493	-1.284085	1.325647	10	1.732403
53	0.130515	-0.29874	-1.599956	1.632832	16	2.854108
54	0.118379	-0.453343	-1.912382	1.968943	10	2.448498
55	0.183604	-0.865038	-1.018713	1.348991	11	0.920921
56	0.168642	-1.03352	-1.844093	2.12068	9	3.817422
57	-0.224321	-1.092757	-1.83668	2.148914	15	3.237537
58	0.026952	-0.777626	-2.689514	2.799806	15	4.134454
60	-0.327492	-0.704687	-1.890117	2.043619	19	16.623264
61	-0.337327	-0.734547	-1.826107	1.997001	17	19.280957
62	-0.322584	-0.500795	-1.612627	1.719134	15	1.948431
63	-0.397611	0.085024	-0.799155	0.896645	4	1.559335
64	-0.212136	-0.389364	-1.523942	1.587137	8	1.911838
65	-0.523883	-0.097248	-0.875293	1.024719	12	1.363425
66	-0.589686	0.214563	-0.397717	0.742931	12	1.381702
67	-0.802903	-0.146503	-0.412654	0.914549	13	19.381183
68	-0.848935	-0.343421	-0.462414	1.025892	10	1.459102
69	-0.725839	-0.577173	-0.746663	1.190578	10	1.233274
70	-0.779942	-0.359151	-0.516849	1.002213	8	1.337344
71	-0.689675	-0.410434	-0.242834	0.838496	13	0.927931
72	-0.616566	-0.542019	-0.332142	0.885583	14	1.25103
75	-0.133891	-0.009202	-0.107718	0.172089	8	39.290533
79	0.444365	0.768369	0.785425	1.185219	12	1.240428
80	0.328935	0.90689	1.904059	2.134499	6	1.95243
81	0.564377	0.802726	1.810661	2.059462	19	6.694863
82	0.271698	0.858203	1.388684	1.654925	23	4.916877
83	0.743054	1.040664	1.35879	1.865857	21	4.402344
84	0.683082	0.268257	1.056994	1.286779	21	2.435789
85	0.517201	0.150762	0.727341	0.905125	24	3.09808
86	0.387515	0.036299	0.339119	0.516224	18	1.031071
87	0.373157	-0.141017	-0.044975	0.40144	16	1.67111
88	0.327681	-0.11824	-0.355165	0.497492	18	1.153047
89	0.267616	-0.107149	-0.735177	0.789673	15	1.103989

GCP Number	Error (X)	Error(Y)	Error(Z)	Error (m)	Projections	Error(pixel)
90	0.3202	-0.308659	-0.768912	0.88827	19	1.085829
91	0.149163	-0.365511	-0.892856	0.976238	21	1.178121
92	0.124758	-0.457856	-1.10992	1.207112	18	1.238057
93	0.238711	-0.363562	-1.138455	1.218704	9	0.969409
95	0.387135	-0.565218	-1.531809	1.678029	11	2.978417
96	-0.138211	-0.332052	-1.101544	1.158775	16	1.684426
97	0.278906	-0.24686	-0.827132	0.907124	22	1.026434
98	0.036073	-0.341082	-0.808971	0.878677	14	0.764139
99	-0.052026	-0.367954	-1.05231	1.115998	22	1.426976
100	0.327231	-0.426791	-1.175399	1.292592	16	0.93557
101	-0.092213	-0.589689	-0.620519	0.860977	16	1.295696
102	-0.150149	-0.353295	-0.862266	0.943856	9	1.626771
103	-0.049194	-0.240833	-0.763173	0.801782	11	1.137655
104	0.157952	0.305033	0.266408	0.434704	22	1.830631
105	0.296935	0.000871	0.319142	0.435916	26	1.323922
106	0.243802	0.003286	0.131378	0.276966	32	1.938758
107	0.224808	0.051527	0.416596	0.476178	25	0.734513
108	0.347343	0.229462	0.726648	0.837446	37	2.096005
109	0.41211	0.383953	0.954527	1.108322	24	0.989099
110	0.313606	0.43961	1.16684	1.285738	29	1.500751
111	0.136278	0.559828	1.247851	1.37445	20	1.551787
112	-0.05114	0.561925	1.492425	1.595527	20	2.358855
114	-0.094539	0.891592	1.33991	1.612213	13	2.710916
115	-0.085802	0.646863	1.078264	1.260336	10	0.922778
116	0.070779	0.51756	1.01144	1.138371	13	2.493244
117	0.105912	0.482797	0.818592	0.956244	18	1.448775
118	0.124286	0.360098	0.465281	0.601336	17	1.639346
119	0.279492	0.383699	0.117822	0.489104	18	2.755812
120	0.178586	0.251806	-0.008229	0.308815	14	1.668753
121	0.115572	0.170204	-0.227865	0.307	13	1.051051
122	-0.030164	0.100598	-0.250867	0.271964	11	3.63683
123	-0.228851	0.154467	-0.125962	0.303479	9	2.222809
124	-0.182478	-0.032483	-0.183289	0.260669	14	29.89518
125	-0.197734	-0.144785	-0.408276	0.476183	12	30.389727
130	0.779476	-0.647352	1.332553	1.674021	27	7.916218
131	0.516574	-0.042935	-0.538832	0.747684	23	5.543341
132	0.511535	-0.058313	-0.740599	0.901973	24	4.488247
133	0.339592	0.089829	-0.621553	0.713947	38	4.433366
134	0.269579	0.146455	-0.61101	0.683707	40	4.547067
135	0.181093	0.212033	-0.626253	0.685526	38	7.274856
136	0.23974	0.390581	-0.537875	0.706639	39	7.550772

GCP Number	Error (X)	Error(Y)	Error(Z)	Error (m)	Projections	Error(pixel)
137	0.353777	0.233772	-0.54608	0.691383	43	8.385916
138	0.250239	0.316528	-0.561135	0.691145	45	6.900641
139	0.022475	0.543297	-0.173712	0.570835	55	3.977513
140	-0.06799	0.400844	-0.566605	0.697381	56	2.739004
141	-0.072794	0.429688	0.220618	0.48847	62	2.730076
142	-0.239377	0.55626	1.062861	1.223274	49	7.792926
144	0.166006	0.478031	0.143857	0.526086	55	4.503787
145	0.334484	0.595819	1.606037	1.745346	57	9.72778
146	0.403133	0.78266	1.952416	2.141729	36	12.468502
147	0.293108	0.412083	0.723566	0.882764	43	5.477493
148	0.459745	0.223657	0.013372	0.511436	32	6.508425
149	0.264403	0.422386	0.700717	0.859839	29	6.239789
150	0.035556	0.533435	1.495732	1.588405	13	7.334352
151	0.532429	0.490882	2.319449	2.429875	31	12.928237
152	0.262689	0.41276	1.122419	1.224419	8	13.725165
153	0.443812	0.538018	1.823312	1.952152	10	10.962288
154	0.46111	0.28598	0.981051	1.121101	11	13.407851
155	0.72116	0.428817	1.791477	1.978218	34	5.559889
156	0.723115	0.100718	0.981554	1.22331	30	5.441588
157	0.895255	0.195195	2.184141	2.368556	37	4.285677
160	0.936534	0.144966	2.841629	2.995491	39	5.556915
161	0.93485	0.047188	2.193996	2.385328	16	1.2811
162	0.669553	-0.012798	1.055805	1.250276	30	5.130669
164	1.092008	-0.10943	2.416933	2.654434	31	11.112868
165	1.325902	-0.235439	3.058024	3.341401	29	9.666489
166	1.328075	-0.423955	4.028823	4.263207	27	16.893352
167	1.219151	-0.33301	2.288116	2.613943	27	5.060517
168	1.385236	-0.457895	2.9732	3.311868	24	14.247924
169	1.135824	-0.772497	2.216002	2.607204	19	12.66349
170	0.55347	-1.072306	1.026944	1.584545	14	14.593633
171	0.739277	-0.86305	0.577344	1.274642	20	9.493459
172	0.825987	-0.269858	0.58731	1.048814	21	6.472721
175	0.687778	-0.002498	0.710836	0.989107	30	4.845369
176	0.44987	0.066398	-0.058234	0.458457	33	2.897592
177	0.313382	0.161034	-0.086982	0.362914	33	5.508322
178	0.420811	-0.025429	-1.211088	1.282366	56	5.667136
179	0.255068	-0.187711	-2.050898	2.075206	45	4.050532
180	0.25767	-0.021707	-2.098445	2.114317	47	5.53869
181	0.279691	0.187642	-1.746854	1.779026	49	3.141755
182	0.10512	0.223238	-2.046803	2.061623	54	2.435703
183	0.161774	0.368979	-1.017345	1.094216	50	6.418409

GCP Number	Error (X)	Error(Y)	Error(Z)	Error (m)	Projections	Error(pixel)
184	-0.012944	0.35429	-1.223472	1.273802	45	3.965456
185	-0.284561	0.423003	-0.959435	1.086472	49	2.351181
186	-0.133878	0.362353	0.648083	0.754476	24	2.287911
187	-0.493748	0.24085	0.793428	0.965051	56	6.439795
188	-0.431097	0.56102	0.922112	1.162273	47	10.210696
189	-0.345446	0.656536	0.340007	0.816074	48	9.362638
190	-0.482221	0.909215	0.921152	1.381206	45	14.87307
191	-4.728988	0.088122	0.723286	4.784793	18	10.421302
192	-1.048641	-0.437503	0.175054	1.149652	23	15.250796
193	-0.869776	-0.423243	-1.646629	1.90972	22	15.601707
194	-0.718085	-0.061958	-2.232596	2.346054	25	9.283737
195	-0.607231	0.091503	-2.404814	2.481982	27	8.401133
196	-0.623226	0.0257	-2.026735	2.120548	35	6.501363
197	-0.672407	0.312629	-0.513122	0.901755	32	8.461258
198	-0.578255	0.345349	-1.659221	1.790715	49	3.402266
199	-0.505628	0.14667	-2.310185	2.369415	35	2.18605
200	-0.438365	0.339432	-1.912861	1.991586	53	3.073787
201	-0.421886	0.296562	-1.561532	1.644482	56	3.192447
202	-0.31192	0.484383	-1.039701	1.188655	47	4.520933
204	-0.334006	0.423012	-0.959602	1.100606	60	3.478857
205	-0.132225	0.365807	-1.320783	1.376869	54	3.071727
206	-0.27125	0.057235	-2.459305	2.47488	53	3.179994
207	-0.489103	-0.052182	-2.460655	2.509336	43	6.345883
208	-0.362982	0.137113	-3.139721	3.163606	27	4.766153
209	-6.052455	-6.058158	-3.104137	9.108741	30	5.478534
210	0.006931	-0.058083	-2.885994	2.886587	44	7.301531
211	1.08038	-1.10799	0.309159	1.578113	23	7.641546
212	0.806702	-0.657383	-0.246295	1.069384	14	5.985405
213	0.561541	-0.724469	-0.853751	1.252627	31	2.78114
214	0.412702	-0.72003	-1.092621	1.372074	30	3.863881
216	0.068216	-0.525437	-2.217957	2.280366	28	3.095704
217	0.284981	-0.483219	-1.543411	1.642203	36	7.313902
218	0.443087	-0.256048	-1.404932	1.495233	42	9.581029
219	0.54715	-0.324461	-0.849977	1.061654	33	7.292644
220	0.437754	-0.468234	-1.275013	1.42707	58	8.390847
221	-1.235366	-3.62376	-2.097705	4.365562	31	1.801879
222	0.420311	-0.09652	-0.997165	1.086423	48	7.390654
223	-0.001886	0.05587	-2.563805	2.564415	40	5.976809
224	0.062725	-0.973168	-3.314618	3.455095	18	8.269948
225	-0.011199	-0.379058	-3.042156	3.065701	36	6.552551
226	0.288161	-0.260851	-2.47446	2.504802	37	9.556081

GCP Number	Error (X)	Error(Y)	Error(Z)	Error (m)	Projections	Error(pixel)
227	-0.144041	-0.277531	-2.814407	2.831724	31	6.442985
228	-0.045421	-0.427602	-1.63833	1.693822	26	7.821651
229	0.70941	-0.724641	-0.022555	1.014335	25	4.598269
230	0.200419	-0.532166	-1.335173	1.451226	21	4.572854
231	-0.022551	-0.103705	-1.790842	1.793984	18	7.025002
232	-0.131062	-0.108247	-2.783247	2.788433	17	5.604958
233	0.034628	0.144978	-2.623847	2.628077	24	8.923278
234	-0.658954	-0.334771	-2.808121	2.903762	12	19.081512
235	-0.548573	0.019639	-1.765155	1.848537	9	42.945489
236	-1.427157	-0.195872	-0.078675	1.442683	15	8.460419
237	-1.64233	-0.266748	0.745392	1.823187	16	5.587954
238	-1.786358	-0.103011	2.748796	3.279873	28	1.555714
239	-1.567713	0.073304	2.268415	2.758406	14	1.61848
240	-1.512359	0.11028	1.278722	1.983563	16	3.013692
241	-1.463121	-0.059373	1.058337	1.806744	18	2.091115
242	-1.643345	-0.111946	1.996166	2.58801	9	2.703101
243	-1.118684	0.224087	2.116091	2.404061	15	15.224432
244	-1.369142	-0.155046	1.00937	1.708044	20	18.660338
245	-1.461183	-0.127019	1.717993	2.258913	19	20.160072
246	-1.359844	0.269205	1.366169	1.946295	25	15.901892
247	-1.213031	0.402923	1.485034	1.959367	27	9.076869
248	-1.114857	0.485545	1.646497	2.046854	31	2.878605
249	-0.895598	0.670453	2.336476	2.590506	19	3.380872
250	-0.739674	0.993037	2.822274	3.081959	14	1.676357
251	-0.673038	0.928369	2.514933	2.764008	16	7.921609
252	-0.360303	0.805387	2.439116	2.593791	12	7.275266
253	-0.231179	0.91375	1.372953	1.665348	15	17.157974
254	-0.416859	0.922308	2.455402	2.655828	10	22.198303
255	0.159259	0.701169	1.920681	2.050857	21	8.67056
256	0.129462	0.849159	2.038637	2.21221	22	4.484767
257	0.261994	0.844777	2.336204	2.498027	26	3.802366
258	0.530207	0.848112	2.504942	2.697248	17	4.602013
259	0.297479	0.245514	3.528723	3.549741	23	12.486302
260	0.754603	0.03635	4.667045	4.727796	27	11.632249
261	0.908722	0.259487	2.708854	2.868971	23	12.177466
262	-0.785303	0.245904	0.602242	1.019738	47	4.676629
Total	0.775007	0.668709	1.580153	1.882735	5409	8.554603

14 Abstract

Good and reliable 3D models and orthophotos are employed for various applications. The UAV-approach to produce very detailed data with the use of photogrammetric software is a recent development. In this work micro UAVs, a combination of fixed-wing and multicopter, were used to develop a dataset of a quarry while keeping the costs to a minimum. The data had to be better than commercially available remote sensing data and compete with terrestrial laser scanning. Aerial photos taken by UAVs were processed and evaluated, with emphasis on structural assessment. For that purpose several software packages were used. For photogrammetric purposes Agisoft Photoscan and VisualSFM were applied. Further processing of the data was done with MATLAB, Meshlab, ArcGIS, and Coltop3D. It was proven that, with proper tools and software, 3D datasets could be developed and evaluated for use in structural geology.

On the hardware side a fixed-wing UAV (Finwing Penguin and Bixler 2) and small multirotors (RCexplorer Tricopter 2.5 and a heavily modified Gaui 540H frame type Hexacopter) were employed. For mission planning and as flight control the APM 2.5 with MissionPlanner was used.

The achieved ground resolution was below 5 cm, the resolution for the calculated DSMs was well below 15 cm.

15 Zusammenfassung

Gute und zuverlässige 3D-Modelle und Orthophotos werden in den verschiedensten Anwendungen eingesetzt. Der Ansatz zur Erstellung detaillierter Daten mit dem Einsatz von UAV-gestützter photogrammetrischer Software wird erst seit kurzer Zeit genutzt. In dieser Arbeit wurde mithilfe von mehreren microUAVs, genauer einer Kombination aus sowohl klassischen Modellflugzeugen als auch Multicoptern, ein 3D-Datensatz von einem Steinbruch erzeugt. Dabei wurde versucht, die Kosten möglichst gering zu halten. Die gewonnenen Daten sollten besser sein als handelsübliche Fernerkundungsdaten und vergleichbar mit terrestrischem Laserscanning. Die Luftbilder der UAVs wurden verarbeitet und auf ihren strukturgeologischen Inhalt hin ausgewertet. Zu diesem Zwecke wurden mehrere Softwarepakete verwendet. Für die Photogrammmetrie wurden die Pakete von Agisoft Photoscan und VisualSFM verwendet. Die Weiterverarbeitung der Daten erfolgte mit MATLAB, Meshlab, ArcGIS und Coltop3D. Es wurde nachgewiesen, dass mit den richtigen Tools und geeigneter Software ein 3D-Datensatz entwickelt und dieser für strukturgeologische Interpretationen ausgewertet werden kann. Auf der Hardwareseite wurden zwei fixed-wing UAVs (Finwing Penguin und Bixler 2) und kleinere Multikopter (RCexplorer Tricopter 2.5 und ein stark modifizierter Gaui 540H Hexacopter) eingesetzt. Für die Flugplanung und als Flugsteuerung wurde ein APM 2.5 in Kombination mit MissionPlanner verwendet. Die erreichten Bodenauflösungen waren kleiner als 5 cm, die Auflösung für die berechneten DHMs lag unter 15 cm.

16 References

16.1 Internet resources

Canon Inc. (2014). S110 Datasheet. http://www.canon.at/For_Home/Product_Finder/Cameras/Digital_Camera/PowerShot/PowerShot_S110/.

CIPR Virtual Outcrop Geology Group (2014a). Background. http://org.uib.no/cipr/Project/VOG/background.htm.

CIPR Virtual Outcrop Geology Group (2014b). Modern systems. http://org.uib.no/cipr/Project/VOG/modern.htm.

CIPR Virtual Outcrop Geology Group (2014c). research hompage. http://org.uib.no/cipr/Project/VOG/research.htm.

DIY drones (2014). DIY Drones Forum. http://diydrones.com/forum.

DIY Drones community (2007). APM. http://ardupilot.com/.

DIY Drones community (2014a). EAGLE schematics of APM 2.5. http://stuff.storediydrones.com/APM_v252_RELEASE.zip.

DIY Drones community (2014b). Vibration Damping and Isolation of the Flight Control Boards. http://copter.ardupilot.com/wiki/vibration-damping/.

Duffy, B. (2014). Flightriot Hompage. flightriot.com.

Fabian Briese (2013). APM Tutorial 02 - Spannungsregler Fix. http://youtu.be/5Ur_s2inGHY?list=UUlCZWv9dKygCflwty9_s8Sw.

Heinrich, G. (2014). Gerys Lipo Fibel. http://rc-modellbau-blog.com/2012/12/das-kleine-lipo-akku-1x1-gerys-lipo-fibel/.

in-Terra (2011). Close range photogrammetry based on UAV imaging after the debris flow and flood disaster in Lötschental (Switzerland) from October 10, 2011. http://pix4d.com/in-terra-ltd/.

Lenzer, B. (2013). Felssturz Felbertauern: Ein Bild der Verwüstung. http://www.dolomitenstadt.at/2013/05/14/felssturz-in-matrei-wurde-durch-wasser-ausgelost/.

O'Callaghan, S. (2014). Dji Phantom flies into Volcano. https://www.youtube.com/watch?v=0-shWVW1UBc.

Pachmann, I. (2012). Kreidefelsen-Unfall: Rügen. http://www.fr-online.de/panorama/kreidefelsen-unfall-ruegen--die-suche-hat-ein-ende,1472782,11545176.html.

Plischka, P. (2014). Kurzschluss im 3,3V Spannungsregler. http://fpv-community.de/showthread.php?37502-APM-2-52-eine-tickende-Zeitbombe-fliegt-%FCber-uns-Kurzschluss-im-3-3V-Spannungsreg.

Public Lab (2013). NDVI with Infrablue. http://publiclab.org/notes/cfastie/04-21-2013/rosco.

Rankin, J. (2013). X8 UAV. https://plus.google.com/113008153233723627606/posts/bBk9HsLKdLu.

rcgroups.com (2014). rcgroups.com Forum. http://www.rcgroups.com/forums/index.php.

Riekkola-Vanhanen, M. (2010). Production Technologies. Talvivaara Mining Company Plc. http://www.talvivaara.com/files/talvivaara/Presentations/Talvivaara_Technical_Seminar_London_May_Presentation.pdf.

Robert (2011). MOBAC - Where are all the map sources gone?

Robertson, J., & Orndorff, R. (2013). The Science of Sinkholes. USGS. http://www.usgs.gov/blogs/features/usgs_top_story/the-science-of-sinkholes/.

Snow, T. (2014). ESC specs for Simonk / BLHeli Firmware. https://docs.google.com/spreadsheet/ccc?key=0AhR02IDNb7_MdEhfVjk3MkRHVzhKdjU1YzdBQkZZRlE#gid=0.

SpiegelOnline (2009). Katastrophe von Nachtersted. http://www.spiegel.de/panorama/katastrophe-von-nachterstedt-behoerde-warnt-vor-weiteren-erdrutschen-a-637062.html.

theguardian (2013). Sinkholes around the world - in pictures. http://www.theguardian.com/world/gallery/2010/jun/03/natural-disasters-guatemala.

Vieira, G. (2014). 3D | antartida - monitoring of antarctic permafrost environments. http://ppl.com.pt/en/prj/3dantartida.

Vorkoetter, S. (2014). How Electric Motors Work. http://www.stefanv.com/rcstuff/qf200212.html.

Wich, S., Koh, L.P., Wunderlin, S., & Pang, K. (2014). conservationdrones.org. http://conservationdrones.org/.

Windestål, D. (2011). Tricopter V2.5. http://rcexplorer.se/projects/2011/09/the-tricopter-v2-5/.

Wu, C. (2007). SiftGPU: A GPU implementation of Scale Invaraint Feature Transform (SIFT). http://cs.unc.edu/~ccwu/siftgpu.

16.2 Software

Agisoft Lens (2011). *Lens*. http://www.agisoft.ru/products/lens.

Agisoft Photoscan (2013). *Photoscan*. www.agisoft.ru/products/photoscan.

CHDK (2006). *Canon Hacker Development Kit*. http://chdk.wikia.com/wiki/CHDK.

ESRI Inc. (1999). *ArcGIS*.

FGT, University of Pisa (2005). *Meshlab*. http://meshlab.sourceforge.net/.

Grasemann, B. (2011). *Solution of the Three-Point-Problem using Cramer's Rule -MATLAB script*.

MathWorks (1984). *MATLAB*.

Michael Oborne (2014). *MissionPlanner:* 3D Robotics.

Microsoft Corporation (2011). *Image Composite Editor*. http://research.microsoft.com/en-us/um/redmond/groups/ivm/ice/.

skiljan, i. (2014). *Irfan View*. http://irfanview.tuwien.ac.at/.

terranum (2011). *Coltop3D.* Lausanne: terranum. http://www.terranum.ch/coltop3d-features.

Trimble Navigation Ltd. (2009). *GPS Pathfinder Office*.

Turner-Jones, B. (2011). *Rocklogger*. http://rockgecko.wordpress.com/.

Zoltán, G. (2014). *minimosd-extra*. https://code.google.com/p/minimosd-extra/.

16.3 Bibliography

Abel, J., Wegner, K., Haas, F., Heckmann, T., & Becht, M. (2014). Comparing data of terrestrial LiDAR and UAV (photogrammetric) in Comparing data of terrestrial LiDAR and UAV (photogrammetric) in the context of the project “SedAlp”. *EGU 2014 Abstracts*. http://meetingorganizer.copernicus.org/EGU2014/EGU2014-6866.pdf.

Allmendinger, R.W., Cardozo, N., & Fisher, D.M. (2011). *Structural Geology Algorithms: Vectors and Tensors:* Cambridge University Press.

Arenson, L.U. (2002). *Unstable alpine permafrost. A potentially important natural hazard - variations of geotechnical behaviour with time and temperature.* Zürich: Vdf Hochschulverlag AG an der ETH Zürich.

Asmar, C., Grasemann, B., & Tari, G. (2014). The Qartaba Structure (Mount Lebanon): structural study and modeling, *16*. http://adsabs.harvard.edu/abs/2014EGUGA.16.6434A.

Barazzetti, L., Remondino, F., Scaioni, M., & Brumana, R. (2010). Fully automatic UAV image-based sensor orientation. *Proceedings of the 2010 Canadian Geomatics Conference and Symposium of Commission I*.

Brown, D.C. (1966). Decentering Distortion of Lenses.

Christian, P. (2014). Using a Low-Cost Unmanned Aircraft System and Structure-From-Motion for Hillslope Gully Modeling. *CSU Geospatial Review*, *12*. http://csugis.sfsu.edu/CSU_Geospatial_Review/2014.pdf.

Drury, S.A. (1998). *Images of the earth. A guide to remote sensing*. (2nd ed.). Oxford [England], New York: Oxford University Press.

Eisenbeiß, H. (2009). UAV photogrammetry. Dissertation. Zürich

Eisenbeiss, H., & Zhang, L. (2006). Comparison of DSMs generated from mini UAV imagery and terrestrial laser scanner in a cultural heritage application. *International Archives of Photogrammetry, Remote Sensing and Spatial Information Sciences XXXVI-5, 90e96*.

Furukawa, Y., Curless, B., Seitz, S.M., Szeliski, R., & Google Inc (2010). R.: Towards internet-scale multiview stereo. *Proceedings of IEEE CVPR*.

Furukawa, Y., & Ponce, J. (2010). Accurate, dense, and robust multiview stereopsis. *IEEE transactions on pattern analysis and machine intelligence*, *32*, 1362–1376.

Gruen, A., Eisenbeiss, H., Blaha, M., Sauerbier, M., & Fux, P. (2009). UAV Photogrammetry Project Drapham Dzong, Bhutan.

Jaboyedoff, M., Metzger, R., Oppikofer, T., Couture, R., Derron, M., Locat, J., & Turmel, D. (2007). New insight techniques to analyze rock-slope relief using DEM and 3D-imaging cloud points. *Rock Mechanics: Meeting Society's Challenges and Demands*, 61–68.

Jancosek, M., & Pajdla, T. (2011). Multi-View Reconstruction Preserving Weakly-Supported Surfaces. *IEEE Conference on Computer Vision and Pattern Recognition 2011*.

Kasser, M., & Egels, Y. (2002). *Digital photogrammetry.* London, New York: Taylor & Francis.

Kääb, A., Haeberli, W., & Gudmundsson, G.H. (1997). Analysing the creep of mountain permafrost using high precision aerial photogrammetry: 25 years of monitoring Gruben rock glacier, Swiss Alps. *Permafrost and Periglacial Processes*, *8*, 409–426.

Kikinis, R., Shenton, M.E., Iosifescu, D.V., McCarley, R.W., Saiviroonporn, P., Hokama, H.H., Robatino, A., Metcalf, D., Wible, C.G., Portas, C.M., Donnino, R.M., & Jolesz, F.A. (1996). A digital brain atlas for surgical planning, model-driven segmentation, and teaching. *IEEE Transactions on Visualization and Computer Graphics*, *2*, 232–241.

Kraus, K. (2004). *Photogrammetrie 1. Geometrische Informationen aus Photographien und Laserscanneraufnahmen.* Berlin: Walter de Gruyter.

Kraus, K. (2007). *Photogrammetry. Geometry from images and laser scans*. (2nd ed.). Berlin, New York: Walter de Gruyter.

Linder, W. (2009). *Digital photogrammetry. A practical course*. (3rd ed.). Berlin, London: Springer.

McGonigle, A. J. S., Aiuppa, A., Giudice, G., Tamburello, G., Hodson, A.J., & Gurrieri, S. (2008). Unmanned aerial vehicle measurements of volcanic carbon dioxide fluxes. *Geophysical Research Letters*, *35*.

Meier, L., Tanskanen, P., Heng, L., Lee, G.H., Fraundorfer, F., & Pollefeys, M. (2012). PIXHAWK: A micro aerial vehicle design for autonomous flight using onboard computer vision. *Autonomous Robots*, *33*, 21–39.

Mikoś, M., & Hübel, J. (2008). *11th Congress INTERPRAEVENT ; 26 - 30 May 2008, Dornbirn, Vorarlberg, Austria ; conference proceedings ; extended abstracts.* Klagenfurt: Villach.

Nex, F., & Remondino, F. (2014). UAV for 3D mapping applications: a review. *Applied Geomatics*, *6*, 1–15.

Paul, F., Kääb, A., & Haeberli, W. (2007). Recent glacier changes in the Alps observed by satellite: Consequences for future monitoring strategies. *Global and Planetary Change*, *56*, 111–122.

Phillips, M., Springman, S., & Arenson, L.U. (2003-2004). *Permafrost. Proceedings of the Eighth International Conference on Permafrost, 21-25 July 2003, Zurich, Switzerland.* Lisse: Balkema.

Prokop, A. (2008). Assessing the applicability of terrestrial laser scanning for spatial snow depth measurements. *Cold Regions Science and Technology*, *54*, 155–163.

Pyle, D.M., Mather, T.A., & Biggs, J. (2013). *Remote sensing of volcanoes and volcanic processes. Integrating observation and modelling*.

Remondino, F., Barazzetti, L., Nex, F., Scaioni, M., & Sarazzi, D. (2011). UAV photogrammetry for mapping and 3d modeling-current status and future perspectives. *International Archives of the Photogrammetry, Remote Sensing and Spatial Information Sciences*, *38*, C22.

Rzybilla, H.-J., & Wester-Ebbinghaus, W. (1979). Bildflug mit ferngelenktem Kleinflugzeug. *Bildmessung und Luftbildwesen, Zeitschrift für Photogrammetrie und Fernerkundung*, *Vol. XLVII*, 137–142.

S. J. Buckley, J. Vallet, A. Braathen, & W. Wheeler (2008). OBLIQUE HELICOPTER-BASED LASER SCANNING FOR DIGITAL TERRAIN MODELLING AND VISUALISATION OF GEOLOGICAL OUTCROPS.

Sauerbier, M., & Eisenbeiß, H. (2010). UAVs for the documentation of archaeological excavations. *International Archives of Photogrammetry, Remote Sensing and Spatial Information Sciences*, *38*.

Slob, S. (2008). Automated rock mass characterisation using 3-D terrestrial laser scanning. PhD. Delft.

Vasuki, Y., Holden, E.-J., Kovesi, P., & Micklethwaite, S. (2014). Semi-automatic mapping of geological Structures using UAV-based photogrammetric data: An image analysis approach. *Computers & Geosciences*, *69*, 22–32.

Verhoeven, G.J., Smet, P.F., Poelman, D., & Vermeulen, F. (2009). Spectral Characterization of a Digital Still Camera's NIR Modification to Enhance Archaeological Observation. *IEEE Transactions on Geoscience and Remote Sensing*, *47*, 3456–3468.

Wester-Ebbinghaus, W. (1980). Aerial Photography by radio controlled model helicopter. *The Photogrammetric Record*, *X*, 85–92.

Wu, C. (2013). Towards Linear-Time Incremental Structure from Motion. *2013 International Conference on 3D Vision (3DV)*, 127–134.

Wu, C., Agarwal, S., Curless, B., & Seitz, S.M. (2011). Multicore bundle adjustment. *2011 IEEE Conference on Computer Vision and Pattern Recognition (CVPR)*, 3057–3064.

Zhou, G. (2009). Near real-time orthorectification and mosaic of small UAV video flow for time-critical event response. *Geoscience and Remote Sensing, IEEE Transactions on*, *47*, 739–747.

17 Curriculum vitae

Personal data

Name	David Grebenstein

Education

Gymnasium	Abitur 2006

Academic studies

Oct. 2007 – Aug. 2010	B.Sc. Geowissenschaften, TU / LMU München
Since Oct. 2010	M.Sc. Erdwissenschaften, University of Vienna